A MEASUREMENT OF THE BRANCHING RATIO

$$\frac{K_L \to \pi^+\pi^-}{K_L \to \pi^\pm e^\mp \overset{(-)}{\nu}}$$

Laura M. Bertolotto

Submitted for the degree of Doctor of Philosophy
The University of Edinburgh
1997

Abstract

The branching ratio of $K_L \to \pi^+\pi^-$ relative to $K_L \to \pi^\pm e^\mp \overset{(-)}{\nu}$ has been measured using preliminary data from the experiment NA48 at the CERN-SPS, whose aim is to determine the CP violation parameter $\mathrm{Re}(\varepsilon'/\varepsilon)$ with an accuracy of 2×10^{-4}.
The performed measurement gave the value

$$\frac{K_L \to \pi^+\pi^-}{K_L \to \pi^\pm e^\mp \overset{(-)}{\nu}} = (0.53 \pm 0.02 \pm 0.02) \times 10^{-2}$$

where the quoted errors are statistical and systematic respectively.

Contents

List of Figures

List of Tables

Introduction

The main aim of particle physics in the last twenty years has been to establish and test the so-called *Standard Model.* Such a theory is very successful in describing all the particle physics phenomena; however, there are still unexplained features, as well as the dependency of this model on experimental measurements of its parameters.

Measurements at the Large Electron Positron Collider at CERN have established that there are only three kinds of light neutrinos, and therefore only three generations of fundamental fermions. For each of these particles there is an antiparticle, but the theory is not invariant under the simple exchange of a particle with its antiparticle: it is necessary to apply three transformations - charge conjugation C, parity P and time reversal T. All this is contained within the Standard Model, which describes strong, weak and electromagnetic interactions (the fourth fundamental force, gravity, is not yet incorporated into the theory). However, there is a clear asymmetry between matter and antimatter in the universe; and in principle there is no reason why what is called "matter" should be favoured with respect to "antimatter".

Unlike strong and electromagnetic forces, the weak interaction is not symmetric under interchange of particle and antiparticle. For example, it is not sufficient to replace a neutrino, which is left-handed, with an antineutrino by applying a charge conjugation transformation. This operation in fact would produce a left-handed antineutrino, which does not exist in nature. It is necessary to apply also the parity transformation; the combined CP operation gives a physical right-handed antineutrino.

A phenomenon in which CP symmetry were violated could produce a substantial difference between matter and antimatter. Only one situation in nature has been observed in which CP symmetry is broken: the neutral kaon

system, with the decay of a long-lived neutral kaon into two either charged or neutral pions, with a branching ratio of about 10^{-3}, and a charge asymmetry in semi-leptonic decays.

The cause of violation of CP symmetry is still an open issue in physics. Most CP violation is due to the mixing of the two CP eigenstates K_1 (CP = +1) and K_2 (CP = -1) into the physical eigenstates K_L and K_S. The complex parameter ε describes this mixing. In addition, according to the Kobayashi-Maskawa model, CP violating decays may be induced through virtual transitions involving heavy quarks ("direct" CP violation). The relative magnitude of such transitions involving CP violation in $K^0 \to 2\pi$ decays is given by the complex parameter ε'.
The determination of ε'/ε should thus allow to discriminate between different theoretical hypotheses. In the figure below the existing measurements of $\mathrm{Re}(\varepsilon'/\varepsilon)$ are shown. While one of the most recent measurements is compatible with zero, the other indicates the presence of direct CP violation.

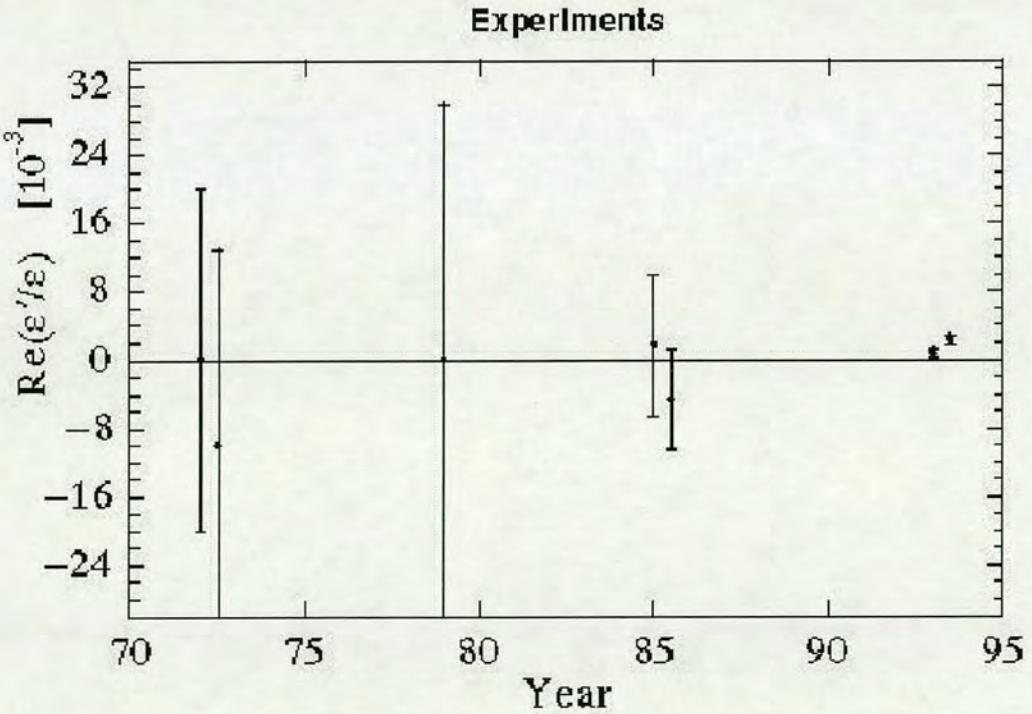

Figure 0.1: Measured values of $\mathrm{Re}(\varepsilon'/\varepsilon)$ as a function of time.

The aim of the NA48 experiment at CERN-SPS is to determine such a parameter with an accuracy of 2×10^{-4}, with one order of magnitude more statistics than any other previous measurement. The advantages of NA48 with respect previous experiments are high statistics and reduced systematic effects. The former aim is achieved by a high intensity primary beam and a pipelined data acquisition, with little or no dead time. The latter feature is given by the simultaneous detection of the four different decays of interest. In this way, differences and variations in detection efficiencies for K_L and K_S decays become unimportant, as do rate dependent effects introduced by accidental activity in the detector elements.

In 1995 the first data-taking period of the experiment took place, without electromagnetic calorimeter. Its purpose was to verify the performance of the magnetic spectrometer and other sub-detectors, of the trigger system and data acquisition. Besides, physics data were collected and allowed the measurement of some parameters of kaon decay. The obtained results are not competitive due to the lack of statistics and to the incompleteness of the experimental apparatus. They are nevertheless useful in understanding the functioning of the setup.

The subject of this thesis is the measurement of the branching ratio of $K_L \to \pi^+\pi^-$. The channel chosen as a normalisation is $K_L \to \pi^\pm e^\mp \overset{(-)}{\nu}$. In the first chapter an overview of the neutral kaon system phenomenology and of CP violation is given. The NA48 experimental technique and the apparatus are described in the second chapter. The data-taking period which took place in 1995 and the off-line algorithms used to reconstruct the collected data are described in chapter three. The fourth chapter illustrates the NA48 Monte Carlo simulation programs and presents the parallelisation of one of them. The event selection procedure is given in the fifth chapter, and the necessary corrections are described in the sixth. The seventh chapter reports the final value of the measurement and a discussion of the systematic error.

Chapter 1

The neutral Kaon system and CP violation

1.1 Discrete Symmetries

Conservation laws in nature are closely connected with invariance under an operation. Such transformations can be *continuous* (such as translations) or *discrete*. For our purposes, three discrete transformations are of interest: parity, P, which is the operation of spatial inversion of coordinates $(x, y, z \rightarrow -x, -y, -z)$; charge conjugation, C, reverses the sign of charge and magnetic moment of a particle; and time reversal T, the antiunitary transformation $t \rightarrow -t$.

The 'CPT theorem' [2, 3] connects these three symmetries, stating that all interactions are invariant under any combination of the transformations C, P, and T. However, physical processes are not necessarily invariant under C, P, T separately, as Lee and Yang suggested in 1956 [4] to explain the "$\tau - \theta$ *puzzle*". During the following year their theory was confirmed by the experimental observations on the angular distribution of the electrons emitted in β-decay of polarised nuclei.

It was assumed that CP was a 'good symmetry' until 1964, when Christenson, Cronin, Fitch and Turlay [5] observed the decay of the K_L meson into a final state of opposite parity ($\pi^+\pi^-$). Such violation is quite small and its only evidence so far comes from the K^0 meson decay.

1.2 The neutral Kaon system

The K^0 mesons are produced by strong interaction processes (such as $\pi^- + p \rightarrow K^0 + \Lambda$), therefore the value of their strangeness quantum number S is defined. According to the quark model, $K^0 \equiv \bar{s}\, d$; the K^0 meson does not coincide with its antiparticle, since its strangeness quantum number is $+1$: $\overline{K^0} \equiv s\, \bar{d}$, with strangeness -1. The K^0 mesons are stable with respect to strong interactions, which conserve strangeness. However, weak interactions give rise to decays of K^0 mesons; furthermore, the transition $K^0 \rightarrow \overline{K^0}$ is *a priori* allowed, since strangeness is not conserved by the weak hamiltonian. Therefore, a two-dimensional space spanned by the two states $|K^0>$ and $|\overline{K^0}>$ can be introduced:

$$|K^0> \equiv \begin{bmatrix} 1 \\ 0 \end{bmatrix}, \quad |\overline{K^0}> \equiv \begin{bmatrix} 0 \\ 1 \end{bmatrix} \tag{1.1}$$

and the Schrödinger equation can be written for a generic state

$$|\Psi(t)> = \Psi_1(t)|K^0> + \Psi_2(t)|\overline{K^0}> = \begin{pmatrix} \Psi_1(t) \\ \Psi_2(t) \end{pmatrix}. \tag{1.2}$$

The Schrödinger equation itself has the form

$$i\frac{\partial}{\partial t}|\Psi(t)> = H|\Psi(t)> \tag{1.3}$$

where the hamiltonian H is a generic 2×2 matrix, in general non-hermitian in order to account for decays. The two linear combinations of $|K^0>$ and $|\overline{K^0}>$ which diagonalize H are the stationary states, i.e. the states with definite mass and lifetime.

It is always possible to decompose the hamiltonian as

$$H = M - \frac{i}{2}\Gamma, \tag{1.4}$$

where M and Γ are both hermitian matrices:

$$M = \begin{pmatrix} M_{11} & M_{12} \\ M_{12}^* & M_{22} \end{pmatrix}; \quad \Gamma = \begin{pmatrix} \Gamma_{11} & \Gamma_{12} \\ \Gamma_{12}^* & \Gamma_{22} \end{pmatrix}. \tag{1.5}$$

If the weak interactions were set to zero, then $|K^0>$ and $|\overline{K^0}>$ would be mass degenerate states, and it would be

$$M_{11} = M_{22}; \quad M_{12} = 0; \quad \Gamma = 0. \tag{1.6}$$

Due to CPT invariance, which is always assumed, the following relations hold in general:

$$M_{11} = M_{22} = m; \quad \Gamma_{11} = \Gamma_{22} = \gamma. \tag{1.7}$$

Before proceeding to diagonalize H in its general form, let us consider the particular case

$$M_{12} = M_{12}^*; \quad \Gamma_{12} = \Gamma_{12}^*. \tag{1.8}$$

In this case H is symmetric, with eigenvectors

$$|K_1> = \frac{1}{\sqrt{2}}\left(|K^0> + |\overline{K^0}>\right) \tag{1.9}$$

$$|K_2> = \frac{1}{\sqrt{2}}\left(|K^0> - |\overline{K^0}>\right). \tag{1.10}$$

These are CP eigenstates, with eigenvalues $+1$ and -1 respectively. It can be concluded that, when M_{12} and Γ_{12} are real, CP commutes with the hamiltonian, and therefore $K^0 \leftrightarrow \overline{K^0}$ is a CP-conserving process.

Let us now examine the general case. The eigenvalues of the matrix H are

$$\begin{aligned} M_S - \frac{i}{2}\Gamma_S &= m - \frac{i}{2}\gamma + R \\ M_L - \frac{i}{2}\Gamma_L &= m - \frac{i}{2}\gamma - R \end{aligned} \tag{1.11}$$

where

$$R = \sqrt{\left(M_{12} - \frac{i}{2}\Gamma_{12}\right)\left(M_{12}^* - \frac{i}{2}\Gamma_{12}^*\right)}. \tag{1.12}$$

The measured values for masses and lifetimes are [6]:

$$\begin{aligned} m_K &= \frac{M_S + M_L}{2} = 0.497672 \pm 0.000031 \ \text{GeV/c}^2 \\ \Delta M &= (3.491 \pm 0.009) \times 10^{-15} \ \text{GeV/c}^2 \\ \tau_L &= 1/\Gamma_L = (5.17 \pm 0.04) \times 10^{-8} \ \text{s} \\ \tau_S &= 1/\Gamma_S = (0.8927 \pm 0.0009) \times 10^{-10} \ \text{s} \end{aligned}$$

The two eigenvectors are

$$\begin{aligned} |K_S> &= p|K^0> + q|\overline{K^0}> \\ |K_L> &= p|K^0> - q|\overline{K^0}> \end{aligned} \tag{1.13}$$

where

$$\frac{p}{q} = \sqrt{\frac{M_{12}^* - \frac{i}{2}\Gamma_{12}^*}{M_{12} - \frac{i}{2}\Gamma_{12}}}; \quad |p|^2 + |q|^2 = 1. \tag{1.14}$$

The indices L (long) and S (short) reflect the difference in lifetimes of the two eigenstates. The quantities q and p are not physical. In fact, if a strangeness rotation (of a quantity φ) on $|K^0>$ and $|\overline{K^0}>$ is performed :

$$|K^0> \to |K^0>' = e^{i\varphi}|K^0>; \quad |\overline{K^0}> \to |\overline{K^0}>' = e^{-i\varphi}|\overline{K^0}> \tag{1.15}$$

the form of the CP operator is modified, from the original definition

$$CP|K^0> = e^{i\alpha}|\overline{K^0}>; \quad CP|\overline{K^0}> = e^{-i\alpha}|K^0> \tag{1.16}$$

to

$$CP|K^0>' = e^{i(\alpha+2\varphi)}|\overline{K^0}>'; \quad CP|\overline{K^0}>' = e^{-i(\alpha+2\varphi)}|K^0>' . \tag{1.17}$$

Because of the relations (1.15), the off-diagonal terms of M and Γ transform:

$$\begin{aligned} M_{12} &= <|K^0|M|\overline{K^0}> \to e^{-2i\varphi} M_{12} \\ \Gamma_{12} &= <|K^0|\Gamma|\overline{K^0}> \to e^{-2i\varphi} \Gamma_{12} \end{aligned} \tag{1.18}$$

This implies

$$\frac{q}{p} \to e^{2i\varphi}\frac{q}{p} \tag{1.19}$$

Measurable quantities, such as the eigenvalues defined in eq. (1.11), are not affected by this transformation.

The integration of the Schrödinger equation (1.3) gives

$$|K_S(t)> = e^{-i\left(M_S - \frac{i}{2}\Gamma_S\right)t}|K_S(0)> \tag{1.20}$$

$$|K_L(t)> = e^{-i\left(M_L - \frac{i}{2}\Gamma_L\right)t}|K_L(0)> . \tag{1.21}$$

Let us consider a beam composed of K^0 mesons only, produced at the time $t = 0$. From the equations (1.13),

$$|\Psi(0)> = |K^0> = \frac{1}{2p}\left(|K_S(0)> + |K_L(0)>\right), \tag{1.22}$$

which implies

$$\begin{aligned} |\Psi(t)> &= \frac{1}{2p}\left(|K_S(t)> + |K_L(t)>\right) \\ &= f_+(t)|K^0> + \frac{q}{p} f_-(t)|\overline{K^0}> \end{aligned} \tag{1.23}$$

where

$$f_{\pm}(t) = \frac{1}{2}\left[e^{-i\left(M_S - \frac{i}{2}\Gamma_S\right)t} \pm e^{-i\left(M_L - \frac{i}{2}\Gamma_L\right)t}\right]. \quad (1.24)$$

The probability of finding a K^0 meson in the beam after a time t is proportional to

$$\begin{aligned} |< K^0|\Psi(t) >|^2 &= |f_+(t)|^2 \\ &= \frac{1}{4}\left[e^{-\Gamma_S t} + e^{-\Gamma_L t} + 2e^{-\frac{\Gamma_S+\Gamma_L}{2}t}\cos(\Delta M t)\right] \end{aligned} \quad (1.25)$$

while that of finding a $\overline{K^0}$ is given by

$$\begin{aligned} |< \overline{K^0}|\Psi(t) >|^2 &= \left|\frac{q}{p}\right|^2 |f_-(t)|^2 \\ &= \left|\frac{q}{p}\right|^2 \frac{1}{4}\left[e^{-\Gamma_S t} + e^{-\Gamma_L t} - 2e^{-\frac{\Gamma_S+\Gamma_L}{2}t}\cos(\Delta M t)\right] \end{aligned} \quad (1.26)$$

1.3 Decays of K meson

In table 1.1 the branching ratios of the dominant decay modes of K_L meson are given.

Decay mode	Branching Ratio
$K_L \to \pi^{\pm} e^{\mp} \overset{(-)}{\nu}$	$(38.78 \pm 0.27)\%$
$K_L \to \pi^{\pm} \mu^{\mp} \overset{(-)}{\nu}$	$(27.17 \pm 0.25)\%$
$K_L \to \pi^0\pi^0\pi^0$	$(21.12 \pm 0.27)\%$
$K_L \to \pi^+\pi^-\pi^0$	(12.56 ± 0.20)
$K_L \to \pi^+\pi^-$	$(2.067 \pm 0.035) \cdot 10^{-3}$
$K_L \to \pi^0\pi^0$	$(9.36 \pm 0.20) \cdot 10^{-4}$

Table 1.1: The main decay modes of K_L meson.

1.3.1 Semi-Leptonic decays

The semi-leptonic decays (K_{l3}) account for $\sim 66\%$ of all K_L decays. In the process

$$K \to \pi \nu l \quad (1.27)$$

where l is a charged lepton, either μ or e, the lepton wave functions enter the decay amplitude in the standard form

$$J_l^\lambda = \bar{\nu}\, i\gamma_\lambda(1+\gamma_5)l. \tag{1.28}$$

In order to obtain a Lorentz invariant amplitude, this must be contracted with a hadronic vector current made from the momenta of the kaon (p_K) and the pion (p_π), the most general form being

$$f_+(p_K+p_\pi)_\lambda + f_-(p_K-p_\pi)_\lambda. \tag{1.29}$$

The functions f_+, f_- are dimensionless form factors which can depend on

$$q^2 = (p_K - p_\pi)^2, \tag{1.30}$$

the square of the four-momentum transferred to the leptons.
The covariant amplitude is then [7]

$$M = \frac{G}{\sqrt{(2)}}\left[f_+(p_K-p_\pi)^\lambda + f_-(p_K-p_\pi)^\lambda\right]\bar{\nu}\, i\gamma_\lambda(1+\gamma_5)l \tag{1.31}$$

where G is the universal weak coupling constant. Time reversal would require f_+ and f_- to be relatively real. The form factor f_- does not contribute appreciably in case of electrons; for by momentum conservation:

$$p_K - p_\pi = p_l + p_\nu \tag{1.32}$$

and

$$\bar{\nu}\,(i\gamma p_l + i\gamma p_\nu)(1+\gamma_5)l \simeq -m_l\,\bar{\nu}\,(1-\gamma_5)l \tag{1.33}$$

for the Dirac equation of the leptons. The electron mass is negligible compared to other energies and masses involved.
According to this parametrisation, the Dalitz plot density can be written as

$$\rho \propto Af_+^2 + Bf_+f_- + Cf_-^2 \tag{1.34}$$

where the quantities A, B and C are

$$\begin{aligned} A &= m_K(2E_\pi E_\nu - m_K E'_\pi) + m_l^2(\frac{1}{4}E'_\pi - E_\nu) \\ B &= m_l^2(E_\nu - \frac{1}{2}E'_\pi) \\ C &= m_l^2 E'_\pi/4 \end{aligned} \tag{1.35}$$

with

$$E'_\pi = E_\pi^{max} - E_\pi = \frac{m_K^2 + m_\pi^2 - m_l^2}{2m_K} - E_\pi \tag{1.36}$$

For K_{e3}, only the form factor f_+ is involved, since the quantities B and C vanish. For the $K_{\mu 3}$ decays, a parameter ξ is usually introduced as

$$\xi(q^2) = f_-(q^2)/f_+(q^2) \tag{1.37}$$

Since the K_{e3} rate depends only on $f_+(q^2)$, the ratio $\Gamma(K \to \pi\mu\nu)/\Gamma(K \to \pi e\nu)$ provides a quadratic relationship for ξ. Analyses of semi-leptonic decays frequently assume a linear dependence

$$f_\pm(q^2) = f_\pm(0)\left[1 + \lambda_\pm \frac{q^2}{m_\pi^2}\right] \tag{1.38}$$

The experimental results are [6]:

$$\begin{aligned} \lambda_+ &= 0.0286 \pm 0.0022 \\ \xi &= -0.35 \pm 0.15 \end{aligned} \tag{1.39}$$

It has been shown in the previous section that a beam initially containing only K^0 mesons, after a time t will contain both K^0 and $\overline{K^0}$ with probabilities given by eqs. (1.25-1.26). Neglecting CP violation effects, i.e. $q/p = 1$, one finds:

$$\frac{N(K^0) - N(\overline{K^0})}{N(K^0) + N(\overline{K^0})} = \frac{2\cos(\Delta M t)}{e^{-\frac{\Delta\Gamma t}{2}} + e^{\frac{\Delta\Gamma t}{2}}}, \tag{1.40}$$

where $N(K^0)$ $(N(\overline{K^0}))$ denotes the number of K^0 $(\overline{K^0})$ mesons in the beam at the time t. These quantities can be determined experimentally by studying the semi-leptonic decays of K mesons. In fact, such decays obey the $\Delta S = \Delta Q$ rule, which states that the variation of strangeness in the process equals the charge difference between hadrons in the initial and final states. Because of this selection rule, the decay modes

$$\begin{aligned} K^0 &\to \pi^- e^+ \nu_e \\ \overline{K^0} &\to \pi^+ e^- \overline{\nu}_e \end{aligned}$$

are allowed, while the same processes with opposite sign of the lepton charges are forbidden. As a consequence, $N(K^0)$ is proportional to the number of observed *positrons*, and $N(\overline{K^0})$ to the number of observed *electrons*, and the quantity in eq. (1.40) can be experimentally measured as a function of time.

1.3.2 Decays into three pions

It will be discussed in the next section (1.3.3) that the $K_L \to 2\pi$ decays would not occur if CP were an exact symmetry, since in such a case the K_L meson would be a CP eigenstate with eigenvalue -1, and could not decay into two pions. The same argument does not hold for the quantity

$$\eta_{\pm 0} = \frac{< \pi^+\pi^-\pi^0|T_W|K_S >}{< \pi^+\pi^-\pi^0|T_W|K_L >} \tag{1.41}$$

since the three-pion states contain a component with CP= $+1$ (when the isospin I is 0, 2), although strongly suppressed by centrifugal barrier effects. This allows K_S mesons to decay in three pions even if CP is conserved.
Only $I = 1$ and $I = 3$ states, which are characterised by CP eigenvalue $+1$, are allowed for the decay of K^0 mesons into three neutral pions; so, the process $K_S \to \pi^0\pi^0\pi^0$ violates CP symmetry, and the quantity

$$\eta_{000} = \frac{< \pi^0\pi^0\pi^0|T_W|K_S >}{< \pi^0\pi^0\pi^0|T_W|K_L >} \tag{1.42}$$

would be different from zero only in presence of CP violation.
The violation of CP symmetry in the long-lived three-pion decay would appear as interference in the final state between the dominant CP negative state and a state of opposite CP.

The decay amplitude at the centre of the kinematically allowed region (the Dalitz plot) is conventionally expanded as [8, 9]:

$$A(K^0 \to \pi^+\pi^-\pi^0) \propto 1 + g\frac{s_3 - s_0}{m^2_{\pi+}} + h\left[\frac{s_3 - s_0}{m^2_{\pi+}}\right]^2 + j\frac{s_2 - s_1}{m^2_{\pi+}} + k\left[\frac{s_2 - s_1}{m^2_{\pi+}}\right]^2 + \cdots \tag{1.43}$$

where the kinematics is given by

$$K(k) \to \pi^+(p_1)\pi^-(p_2)\pi^0(p_3), \tag{1.44}$$

and the Lorentz-invariant energy variables are defined as:

$$s_i = (k - p_i)^2; \quad s_0 \equiv \frac{1}{3}(s_+ + s_- + s_3) = m^2_\pi + \frac{1}{3}m^2_K. \tag{1.45}$$

The parameter g measures the (CP non-violating) asymmetry along the π^0 energy axis. The parameter j arises from the interference between the CP-even and CP-odd amplitude in the $K_L \to \pi^+\pi^-\pi^0$ decay [10]. It hence

describes a charge asymmetry which signals the occurrence of a CP violating process. A similar charge asymmetry is found also in the $K_S \to \pi^+\pi^-\pi^0$ decays, but it is not a manifestation of CP violation.
Two different experiments [11, 12] give the present limits on the value of the parameter j:

$$\begin{aligned} j &= -0.001 \pm 0.003 \\ j &= \quad 0.001 \pm 0.011 \end{aligned}$$

respectively. No new measurement has been reported since 1977.

1.3.3 Decays into two pions

In order to determine whether the eigenstates of the hamiltonian H are also CP eigenstates, the decays of K mesons into two-pion states ($|\pi^0\pi^0>$ or $|\pi^+\pi^->$) and three-pion states ($|\pi^0\pi^0\pi^0>$ or $|\pi^+\pi^-\pi^0>$) have to be considered. The reason is that two-pion states are CP eigenstates with eigenvalue $+1$, while three-pion states are predominantly in a CP eigenstate with eigenvalue -1. As a consequence, if K_L and K_S are also CP eigenstates, K_S can decay only into two pions, and K_L only into three pions.
Two-pion states are usually classified according to their isotopic spin I. Since $I = 1$ is forbidden by Bose statistic, the two final pions can have either $I = 0$ or $I = 2$ [13]. The Clebsch-Gordon decomposition gives

$$\begin{aligned} |\pi^+\pi^-> &= \sqrt{\frac{2}{3}}\,|\pi\pi, I=0> \;+\; \sqrt{\frac{1}{3}}\,|\pi\pi, I=2> \\ |\pi^0\pi^0> &= -\sqrt{\frac{1}{3}}\,|\pi\pi, I=0> \;+\; \sqrt{\frac{2}{3}}\,|\pi\pi, I=2> \end{aligned} \qquad (1.46)$$

In the following, the simplified notation

$$|0> \;\equiv\; |\pi\pi, I=0>; \quad |2> \;\equiv\; |\pi\pi, I=2>\,. \qquad (1.47)$$

will be used.
Since K mesons belong to $I = 1/2$ multiplets, the transition can be characterised by $\Delta I = 1/2$ or $\Delta I = 3/2$. A well-established experimental fact of hadron physics is that weak amplitudes corresponding to processes with isospin variation $\Delta I = 1/2$ are strongly enhanced with respect to those with

higher ΔI (the so-called non-leptonic $\Delta I = 1/2$ selection rule). If this rule were exact, one would have

$$\frac{\Gamma(K_S \to \pi^+\pi^-)}{\Gamma(K_S \to \pi^0\pi^0)} = 2. \tag{1.48}$$

Indeed, the observed value is 2.186 [6], thus in accordance with the validity of the $\Delta I = 1/2$ rule.

It is customary to introduce the quantities

$$\eta_{\pm} = \frac{<\pi^+\pi^-|T_W|K_L>}{<\pi^+\pi^-|T_W|K_S>} \tag{1.49}$$

$$\eta_{00} = \frac{<\pi^0\pi^0|T_W|K_L>}{<\pi^0\pi^0|T_W|K_S>} \tag{1.50}$$

where T_W is the weak transition matrix. Both $\eta_{\pm}$ and η_{00} vanish if CP is conserved; so they are the appropriate quantities to investigate CP violation. Decomposing the two-pion states as in eqs. (1.46), one finds

$$\eta_{\pm} = \frac{\varepsilon_0 + \frac{\omega}{\sqrt{2}}\varepsilon_2}{1 + \frac{\omega}{\sqrt{2}}} \tag{1.51}$$

$$\eta_{00} = \frac{\varepsilon_0 - \sqrt{2}\omega\varepsilon_2}{1 - \sqrt{2}\omega}, \tag{1.52}$$

where

$$\varepsilon_I = \frac{<I|T_W|K_L>}{<I|T_W|K_S>} \cdot \frac{1 - \frac{q}{p}\frac{<I|T|\overline{K}^0>}{<I|T|K^0>}}{1 + \frac{q}{p}\frac{<I|T|\overline{K}^0>}{<I|T|K^0>}}, \quad I = 0, 2 \tag{1.53}$$

$$\omega = \frac{<2|T_W|K_S>}{<0|T_W|K_S>} \cdot \frac{1 + \frac{q}{p}\frac{<2|T|\overline{K}^0>}{<2|T|K^0>}}{1 + \frac{q}{p}\frac{<0|T|\overline{K}^0>}{<0|T|K^0>}} \cdot \frac{<2|T_W|K^0>}{<0|T_W|K^0>}. \tag{1.54}$$

It is worth noticing that ε_I and ω are invariant under the phase redefinition of eq. (1.15).

The weak hamiltonian H_W can be decomposed as a sum of two terms:

$$H_W = H_W^{\Delta S=2} + H_W^{\Delta S=1} \tag{1.55}$$

where the first term gives rise to $K^0 - \overline{K^0}$ mixing, a process where strangeness changes by two units, and the second one is responsible for K meson decays. In the same way, at first order in weak interactions, the transition matrix T_W can be decomposed as:

$$T_W = T_W^{\Delta S=2} + T_W^{\Delta S=1}. \tag{1.56}$$

The amplitudes $< I|T_W|K^0 >$ and $< I|T_W|\overline{K^0} >$ receive contributions only from $T_W^{\Delta S=1}$ $(I = 0, 2)$, while $T_W^{\Delta S=2}$ affects ε_I and ω indirectly through q/p.

DIRECT CP VIOLATION

In the most general case, when CP symmetry is violated in K decays, the following relation holds:

$$\frac{< 2|T_W|\overline{K^0} >}{< 2|T_W|K^0 >} \neq \frac{< 0|T_W|\overline{K^0} >}{< 0|T_W|K^0 >}, \tag{1.57}$$

and one obtains

$$\eta_{\pm} = \varepsilon_0 + \frac{\omega}{\sqrt{2}\left(1 + \omega/\sqrt{2}\right)}(\varepsilon_2 - \varepsilon_0) \tag{1.58}$$

$$\eta_{00} = \varepsilon_0 - \frac{2\omega}{\sqrt{2}\left(1 - \omega\sqrt{2}\right)}(\varepsilon_2 - \varepsilon_0). \tag{1.59}$$

The following notation will be adopted:

$$\varepsilon \equiv \varepsilon_0; \quad \varepsilon' \equiv \frac{\omega}{\sqrt{2}}(\varepsilon_2 - \varepsilon_0). \tag{1.60}$$

If terms of order ω^2 are neglected (because of the $\Delta I = 1/2$ rule), eqs. (1.58-1.59) become

$$\eta_{\pm} \simeq \varepsilon + \varepsilon' \tag{1.61}$$

$$\eta_{00} \simeq \varepsilon - 2\varepsilon'. \tag{1.62}$$

The quantity ε' gives a new kind of CP violation, independent of $K^0 - \overline{K^0}$ mixing, known as *direct* CP violation. The parameter ε represents the contribution to CP violation given by mixing (*indirect* CP violation).
It is possible to determine experimentally the branching ratios of the different K decay modes, and measure the quantity

$$R = \frac{\Gamma(K_L \to \pi^+\pi^-)/\Gamma(K_S \to \pi^+\pi^-)}{\Gamma(K_L \to \pi^0\pi^0)/\Gamma(K_S \to \pi^0\pi^0)} = \left|\frac{\eta_{\pm}}{\eta_{00}}\right|^2 \simeq 1 + 6\mathrm{Re}\left(\frac{\varepsilon'}{\varepsilon}\right) \tag{1.63}$$

1.4 THEORETICAL MODELS FOR CP VIOLATION

1.4.1 SUPERWEAK MODEL

If all CP violating effects are due to $H_W^{\Delta S=2}$ (that is, to the mixing process), one has

$$(CP)T_W^{\Delta S=1}(CP)^{-1} = T_W^{\Delta S=1} \tag{1.64}$$

and taking into account the fact that $\pi\pi$ states are CP eigenstates with eigenvalue $+1$, one finds

$$\begin{aligned} < I|T_W|K^0 > &= < I|T_W^{\Delta S=1}|K^0 > \\ &= < I|(CP)^{-1}T_W^{\Delta S=1}(CP)|K^0 > \\ &= < I|T_W|\overline{K^0} > e^{i\alpha} \end{aligned} \tag{1.65}$$

for both $I = 0$ and $I = 2$. The phase factor $e^{2i\alpha}$ has been introduced to account for the arbitrariness in the definition of CP. From eqs. (1.53–1.54) one obtains

$$\varepsilon_2 = \varepsilon_0 \tag{1.66}$$

$$\eta_{\pm} = \eta_{00} = \varepsilon_0. \tag{1.67}$$

This situation, in which CP-violating effects are confined in $K^0 - \overline{K^0}$ mixing while K decays are CP-conserving, is usually called *superweak CP violation* [14].

1.4.2 CP VIOLATION IN THE STANDARD MODEL

In the gauge sector of the Standard Model, which describes the interactions of fermions with gauge fields and of gauge vectors among themselves, CP is conserved, since no complex phase is present. Only in the interaction of fermions with the scalar Higgs doublet (introduced to generate fermion masses) a complex phase is found, which can give rise to a violation of CP symmetry:

$$\mathcal{L}_{YUKAWA} = \left(h_{ij}^u \overline{\psi}_{Li}^u \psi_{Rj}^u + h_{ij}^d \overline{\psi}_{Li}^d \psi_{Rj}^d\right) v + \text{h.c.} \tag{1.68}$$

where h^u, h^d are the Yukawa couplings, i and j are generation indices and v is the vacuum expectation value of the neutral Higgs field. The fermionic fields ψ are:

$$\psi_{L,R}^u = \begin{pmatrix} u \\ c \\ t \end{pmatrix}_{L,R} \quad ; \quad \psi_{L,R}^d = \begin{pmatrix} d \\ s \\ b \end{pmatrix}_{L,R} \tag{1.69}$$

where the subscripts L, R denote the left and right-handed components, respectively.

In order to find the physical eigenstates ψ^{0u} and ψ^{0d}, the 3×3 matrices

$$M^u = h^u v, \quad M^d = h^d v \tag{1.70}$$

have to be diagonalized. The bi-unitary rotations which realize such a diagonalization can be defined as

$$U_L^\dagger M^u U_R = M^u_{diag}; \quad V_L^\dagger M^d V_R = M^d_{diag}. \tag{1.71}$$

and one finds

$$\psi^u_{L,R} = U_L \psi^{0u}_{L,R}; \quad \psi^d_{L,R} = V_L \psi^{0d}_{L,R}. \tag{1.72}$$

The lagrangian has thus the form

$$\mathcal{L}_{YUKAWA} = \overline{\psi}^{0u}_L diag(m_u, m_c, m_t)\psi^{0u}_R + \overline{\psi}^{0d}_L diag(m_d, m_s, m_b)\psi^{0d}_R \tag{1.73}$$

where $m_u, \ldots, m_b$ are the masses of the corresponding quarks.
The change of basis from the fermionic fields ψ to the physical eigenstates ψ^0 in the charged current sector (i.e. the coupling of physical quarks with the charged vector bosons $W^\pm$) gives

$$\overline{\psi}^u_L \gamma^\mu \psi^d_L W^+_\mu \to \overline{\psi}^{0u}_L U_L^\dagger \gamma^\mu V_L \psi^{0d}_L W^+_\mu \tag{1.74}$$

The matrix $U_L^\dagger V_L$ is the so-called Cabibbo-Kobayashi-Maskawa (CKM) matrix, which generalises the Cabibbo mixing mechanism [15, 16].
Taking into account the fact that spinors are defined up to a phase, the CKM matrix for n fermion generations has $(n-1)^2$ real parameters, out of which $\frac{1}{2}(n-1)(n-2)$ are phases. When $n = 3$, the CKM matrix is described by three angles and one phase, and it can be represented (as Wolfenstein proposed, [17]) as

$$\begin{pmatrix} V_{ud} & V_{us} & V_{ub} \\ V_{cd} & V_{cs} & V_{cb} \\ V_{td} & V_{ts} & V_{tb} \end{pmatrix} = \begin{pmatrix} 1-\lambda^2/2 & \lambda & A\lambda^3(\varrho - i\eta) \\ -\lambda & 1-\lambda^2/2 & A\lambda^2 \\ A\lambda^3(1-\varrho-i\eta) & -A\lambda^2 & 1 \end{pmatrix} + \mathcal{O}(\lambda^4), \tag{1.75}$$

where λ is the sinus of the Cabibbo angle ($\lambda \simeq 0.22$) and the value of A, determined measuring V_{cb}, is at present (0.82 ± 0.10) [6]. The parameter η gives CP violation.

Obviously, the parametrisation of the CKM matrix is not unique; however, a "measure" of CP violation which does not depend on any particular parametrisation can be obtained by writing the unitarity relation:

$$V^\star_{ub} V_{ud} + V^\star_{cb} V_{cd} + V^\star_{tb} V_{td} = 0 \tag{1.76}$$

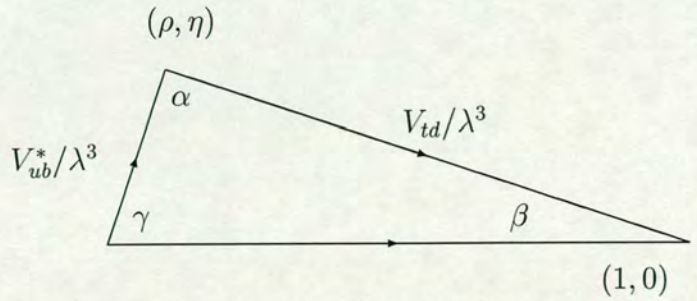

Figure 1.1: The unitarity triangle.

or, according to Wolfenstein's parametrisation,

$$\frac{V_{ub}^\star}{A\lambda^3} + \frac{V_{td}}{A\lambda^3} - 1 = 0. \tag{1.77}$$

This is a triangle in the complex plane (ϱ, η), usually called Jarlskog or Bjorken triangle, whose area is proportional to the amount of CP violation [18]. It is shown in fig. 1.4.2.

Only with more than two fermion generations CP symmetry can be violated in the Standard Model, i.e. a complex phase survives in the CKM matrix. All the elements of such a matrix must be non-vanishing, and the quarks of the same charge must have different masses.

INDIRECT CP VIOLATION IN THE STANDARD MODEL

In the neutral Kaon system, the Standard Model gives CP violation in the $K^0 - \overline{K^0}$ transition ($\Delta S = 2$) as well as in the K decay ($\Delta S = 1$).
Both the short-distance calculation of the box diagram and the long-distance evaluation of the hadronic matrix element have to be taken into account. One obtains [19]

$$M_{12} \simeq \frac{G_F^2}{16\pi^2} m_W^2 (V_{ts} V_{td}^\star)^2 \eta_{tt} \left(\frac{m_t^2}{m_W^2}\right) f\left(\frac{m_t^2}{m_W^2}\right) \frac{1}{2m_K} \alpha_s(\mu^2)^{2/9} \cdot \\ \cdot < \overline{K^0} | (\overline{s}\gamma^\mu(1-\gamma_5)d)(\overline{s}\gamma_\mu(1-\gamma_5)d) | K^0 >, \tag{1.78}$$

where

$$f(x) = \frac{1}{4} + \frac{9}{4} \cdot \frac{1}{1-x} - \frac{3}{2} \cdot \left(\frac{x^2 \ln x}{(1-x)^3}\right) \tag{1.79}$$

and $\eta_{tt} \simeq 0.6$ gives the short-distance QCD corrections.
Concerning the hadronic matrix element, from the completeness relation it

can be written:

$$< \overline{K^0}|(\overline{s}\gamma^\mu\gamma_5 d)(\overline{s}\gamma_\mu\gamma_5 d)|K^0 >= \sum_\lambda < \overline{K^0}|(\overline{s}\gamma^\mu\gamma_5 d)|\lambda >< \lambda|(\overline{s}\gamma_\mu\gamma_5 d)|K^0 > \tag{1.80}$$

and the vacuum insertion gives:

$$< \overline{K^0}|(\overline{s}\gamma^\mu\gamma_5 d)|0 >< 0|(\overline{s}\gamma_\mu\gamma_5 d)|K^0 >= \frac{8}{3} f_K^2 m_K^2. \tag{1.81}$$

The importance of such a contribution in eq. (1.80) is parametrised by a factor B_K which, according to different non-perturbative techniques, ranges from 0.3 to 1. The factor f_K can be measured studying purely leptonic decay, and its present value is $f_K \simeq 114$ MeV.

The heaviness of the top quark makes the contribution due to the (t,t) exchange the dominant one. In conclusion,

$$|\varepsilon| = \frac{G_F^2}{6\sqrt{2}\pi^2} \frac{f_K^2 m_K}{\Delta M} B_K \eta_{tt} m_t^2 f\left(\frac{m_t^2}{m_W^2}\right) A^4 \lambda^{10} \eta(1-\varrho). \tag{1.82}$$

Direct CP violation in the Standard Model

The condition to have CP violation in the $K \to \pi\pi$ decay is that at least two interfering amplitudes contribute to the transition with two different weak and strong phases. The process $K \to \pi\pi$ can proceed at one loop through the flavour changing neutral current transition $s - d$. A W and an up-quark (u, c, t) run in the loop with a virtual gluon attached to the up-quark line converting into a $q\overline{q}$ pair. This one-loop diagram belongs to the class of the so-called *penguin* diagrams and it is a 'strong' one, since a gluon is exchanged. Alternatively, a virtual photon or a Z can be exchanged, thus obtaining an electroweak penguin diagram (see fig. 1.2).

The calculation of the ratio ε'/ε presents many difficulties, mainly due to the evaluation of the hadronic matrix element in the long-distance part.

For a value of m_t between 120 and 200 GeV, ε'/ε varies between 2×10^{-4} and 2×10^{-3}, with large uncertainties. Notice that for large m_t values, even $\varepsilon'/\varepsilon = 0$ can be obtained. The lastest theoretical predictions for the value of $\mathrm{Re}(\varepsilon'/\varepsilon)$ are given in table 1.2.

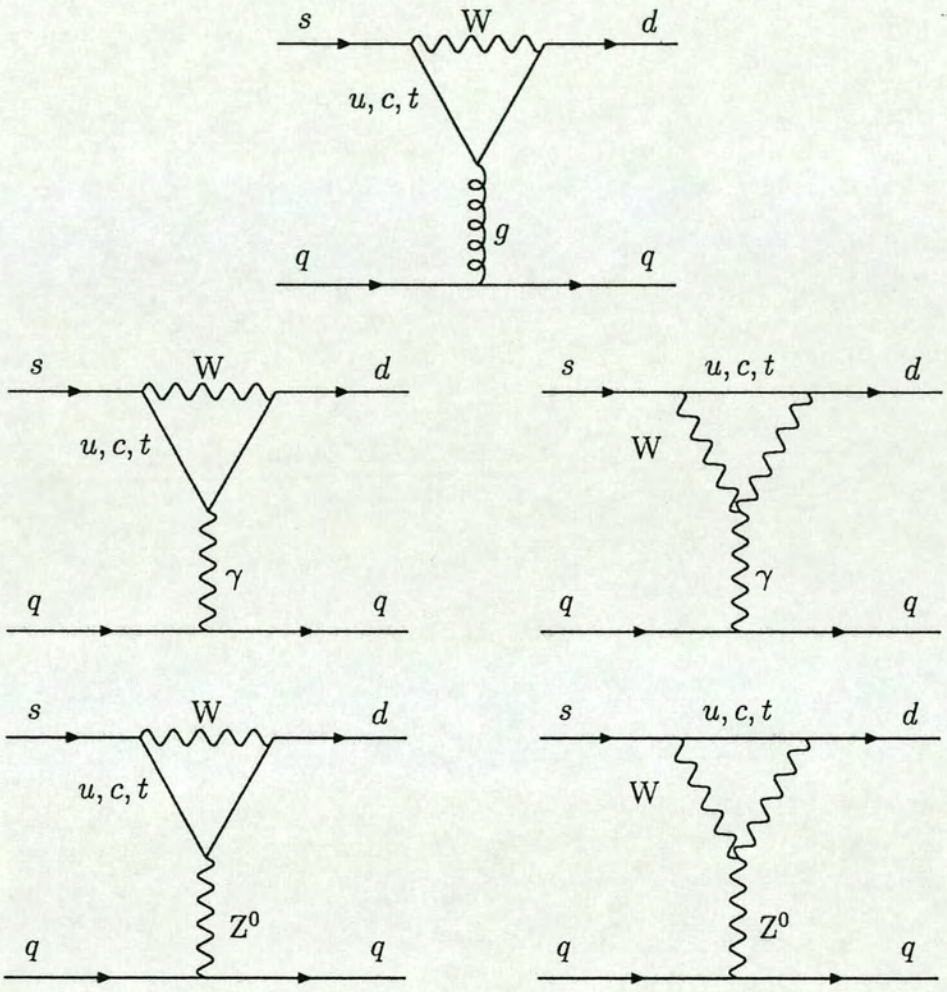

Figure 1.2: The "penguin" diagrams contributing to the two-pion decays. Top, a strong penguin, the other four diagrams are the electroweak penguins.

Predictions of $\mathrm{Re}(\varepsilon'/\varepsilon)$	
Gilman and Wise, Phys. Lett. B83 (1979), 83	1/13 - 1/100
Guberina, Peccei, Nucl. Phys. B163 (1980), 289	$1.5 - 4.4 \cdot 10^{-3}$
Gilman, Phys. Lett. B126 (1983), 111	$> 2.3 \cdot 10^{-3}$
Buras, Phys. Lett. B203 (1988), 272	$\sim 1.6 \cdot 10^{-3}$
Buras, Nucl. Phys. B408 (1993), 209	$6.7 \cdot 10^{-4}$
Ciuchini, Phys. Lett. B301 (1993), 263	$0.5 - 6.8 \cdot 10^{-4}$
Buras, HEP-PH/9609324	$\sim 3.6 \cdot 10^{-4}$

Table 1.2: Predicted values for $\mathrm{Re}(\varepsilon'/\varepsilon)$

1.5 EXPERIMENTAL RESULTS

The quantities connected with CP violation which are experimentally measured are the two complex parameters $\eta_{\pm}$, η_{00}, the charge asymmetry in semi-leptonic decays (here called δ_l)

$$\eta_{\pm} = \frac{A(K_L \to \pi^+\pi^-)}{A(K_S \to \pi^+\pi^-)} = |\eta_{\pm}|\, e^{i\Phi_{\pm}} \tag{1.83}$$

$$\eta_{00} = \frac{A(K_L \to \pi^0\pi^0)}{A(K_S \to \pi^0\pi^0)} = |\eta_{00}|\, e^{i\Phi_{00}} \tag{1.84}$$

$$\tag{1.85}$$

where A is the decay amplitude of the corresponding channel, and

$$\delta_l = \frac{\Gamma(K_L \to l^+\pi^-\nu) - \Gamma(K_L \to l^-\pi^+\overline{\nu})}{\Gamma(K_L \to l^+\pi^-\nu) + \Gamma(K_L \to l^-\pi^+\overline{\nu})} = 2\mathrm{Re}(\varepsilon) \tag{1.86}$$

and the double ratio R:

$$R = \frac{\Gamma(K_L \to \pi^0\pi^0)/\Gamma(K_S \to \pi^0\pi^0)}{\Gamma(K_L \to \pi^+\pi^-)/\Gamma(K_S \to \pi^+\pi^-)} = \left|\frac{\eta_{\pm}}{\eta_{00}}\right|^2 \simeq 1 - 6\mathrm{Re}\left(\frac{\varepsilon'}{\varepsilon}\right) \tag{1.87}$$

In practice, the five measurements which are usually performed are $|\eta_{\pm}|$, the phase $\Phi_{\pm}$, the double ratio R, the difference $\Phi_{00} - \Phi_{\pm}$ and the charge asymmetry δ_l.

The experimental data on ε'/ε are still contradictory. They do not exclude a vanishing value of the ratio, which is a prediction of weak theories of CP violation.

The most recent experimental measurements give [6]:

$$\begin{aligned} |\eta_{\pm}| &= (2.285 \pm 0.019) \times 10^{-3} \\ \Phi_{\pm} &= (43.7 \pm 0.6)^{\circ} \\ \Phi_{00} - \Phi_{\pm} &= (-0.2 \pm 0.8)^{\circ} \\ \delta_l &= (0.327 \pm 0.012)\% \\ \mathrm{Re}(\varepsilon'/\varepsilon) &= (1.5 \pm 0.8) \times 10^{-3} \end{aligned}$$

(where $\Delta m = (0.5304 \pm 0.0014) \times 10^{10}\ \hbar\mathrm{s}^{-1}$ and $\tau_s = (0.8927 \pm 0.0009) \times 10^{-10}$s). The value of $\mathrm{Re}(\varepsilon'/\varepsilon)$ has been derived from the measurements of two different experiments: E731 (Fermilab) and NA31 (CERN). Their final values are [20, 21]:

$$\begin{aligned} &\text{E731}: \quad \mathrm{Re}(\varepsilon'/\varepsilon) = (0.74 \pm 0.52 \pm 0.29) \times 10^{-3} \\ &\text{NA31}: \quad \mathrm{Re}(\varepsilon'/\varepsilon) = (2.3 \pm 0.65) \times 10^{-3} \end{aligned}$$

The value given by NA31 seems to provide evidence for direct CP violation, in agreement with the Standard Model. The E731 measurement, however, is compatible with zero. Other experiments are thus needed in order to obtain more precise results.

1.5.1 Experimental investigation of CP violation in the Kaon system

Two new experiments, at CERN (NA48) and at Fermilab (E832) [25, 22], will provide new data in order to measure ε'/ε with a precision up to 10^{-4}. Both experiments will evaluate the double ratio R (eq. 1.87).
The Φ-factory DAΦNE [23] is in preparation in Frascati. It consists of a high-luminosity e^+e^- collider which will investigate the channel

$$\Phi \to K\overline{K} \to \pi^+\pi^-\pi^0\pi^0 \tag{1.88}$$

in order to measure ε'/ε with a precision of 10^{-4}.

1.5.2 Determination of the CKM Elements

The elements in the first two rows of the CKM matrix can be measured from tree level decays. The present knowledge is summarised below [6]:

- $|V_{ud}|$ - From nuclear β-decay: $|V_{ud}| = 0.9736 \pm 0.0010$.

- $|V_{us}|$ - From kaon decays ($K^+ \to \pi^0 e^+ \nu$, $K_L^0 \to \pi^- e^+ \nu$) and semileptonic hyperon decays ($\Lambda \to p e^- \bar{\nu}$) : $|V_{us}| = 0.2205 \pm 0.0018$.

- $|V_{cd}|$ - From charm production in deep inelastic neutrino (antineutrino) - nucleon scattering ($\nu d \to \mu^- c$): $|V_{cd}| = 0.224 \pm 0.016$.

- $|V_{cs}|$ - From decays of D mesons (e.g. $D^+ \to \overline{K}^0 e^+ \nu$): $|V_{cs}| = 1.01 \pm 0.18$.

- $|V_{cb}|$ - From the exclusive decay $\overline{B}^0 \to D^* l \, \bar{\nu}$ and from the partial width of inclusive semileptonic B decays: $|V_{cb}| = 0.041 \pm 0.003$.

- $|V_{ub}|$ - The ratio $|V_{ub}/V_{cb}|$ is obtained from measurements of the lepton energy spectrum for semileptonic B decays by studying the spectrum beyond the endpoint for the $b \to c$ transition. The result depends strongly on the theoretical model used to generate the lepton spectrum. At present: $|V_{ub}/V_{cb}| = 0.08 \pm 0.02$

Information on the CKM matrix elements involving the top quark can be obtained from favour-changing processes that occur at the one-loop level, for example the particle-antiparticle oscillations of neutral B mesons.
From the measurement of the mass difference ΔM_d from $B_d^0 - \overline{B}_d^0$ mixing and lattice QCD calculations, the quantity $|V_{tb}^* V_{td}|$ can be derived: at present, $|V_{tb}^* V_{td}| = 0.009 \pm 0.003$.
Using results from lattice QCD calculations and the present experimental limit on $\Delta M_{B_s}/\Delta M_{B_d}$, the value $|V_{td}/V_{ts}| < 0.37$ is obtained.

Chapter 2

The NA48 experiment

The NA48 experiment aims for a precision of $2 \cdot 10^{-4}$ on the measurement of $\mathrm{Re}(\varepsilon'/\varepsilon)$. The principles which inspired the design of the experiment are illustrated in this chapter, as well as the main sources of systematic errors. The final set-up of the detector, the kaon beams, the trigger and the data acquisition are described.
The experiment is located in the North Area High Intensity Facility, on the K12 beam line (see fig.2.1), and makes use of a primary proton beam from the Super Proton Synchrotron (SPS) [24], showed in fig.2.2.

2.1 Principle of the experiment

2.1.1 The experimental technique

The measurement of ε'/ε is obtained by evaluating the double ratio of the decay rates of K_L and K_S into two neutral and two charged pions [25]:

$$\mathrm{Re}\left(\frac{\varepsilon'}{\varepsilon}\right) = \frac{1}{6}\left(1 - \frac{\Gamma(\mathrm{K_L} \to \pi^0\pi^0)}{\Gamma(\mathrm{K_S} \to \pi^0\pi^0)} \cdot \frac{\Gamma(\mathrm{K_S} \to \pi^+\pi^-)}{\Gamma(\mathrm{K_L} \to \pi^+\pi^-)}\right) \qquad (2.1)$$

with simultaneous observation of all the four decay modes in the same experimental setup.
The basic NA48 scheme features two nearly collinear beams of K_L and K_S, produced by protons hitting two different targets, and distinguished by tagging of the protons producing the K_S component. A magnetic spectrometer with four drift chambers reduces background in the charged pion mode, and a fast liquid krypton calorimeter will reduce background in the neutral mode. The NA48 detector is illustrated in fig. 2.3.

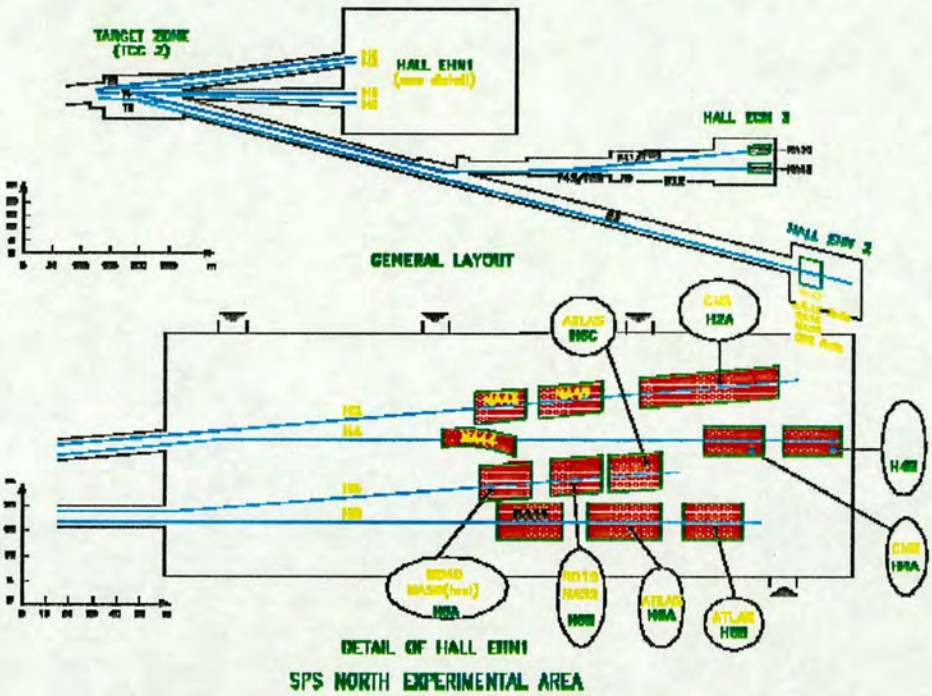

Figure 2.1: The North Area.

The advantage of the method is that, at any given energy and vertex position, the detection efficiencies cancel, provided that the position of the K_L and K_S beams coincide in the detector.

2.1.2 Statistical error

The decay rates $\Gamma(K \to \pi\pi)$ which appear in the expression of the ratio R are evaluated as

$$\Gamma(K \to \pi\pi) = \frac{N_{K\to\pi\pi} - N_{B,K\to\pi\pi}}{\mathcal{N} \cdot \varepsilon}, \tag{2.2}$$

where $N_{K\to\pi\pi}$ is the number of decays of a given type, $N_{B,K\to\pi\pi}$ represents the total number of background events to that type, $\mathcal{N}$ denotes the total number of events, and ε is the detection efficiency (relative to that decay mode). An independent measure of each of the four decay amplitudes which appear in eq. (2.1) is not necessary, since $\mathcal{N}$ cancels in the ratio; it is sufficient to count the events in each decay channel.

The statistical error on the double ratio R is dominated by the statistical precision of CP-violating decays. In order to determine $\mathrm{Re}(\varepsilon'/\varepsilon)$ with a

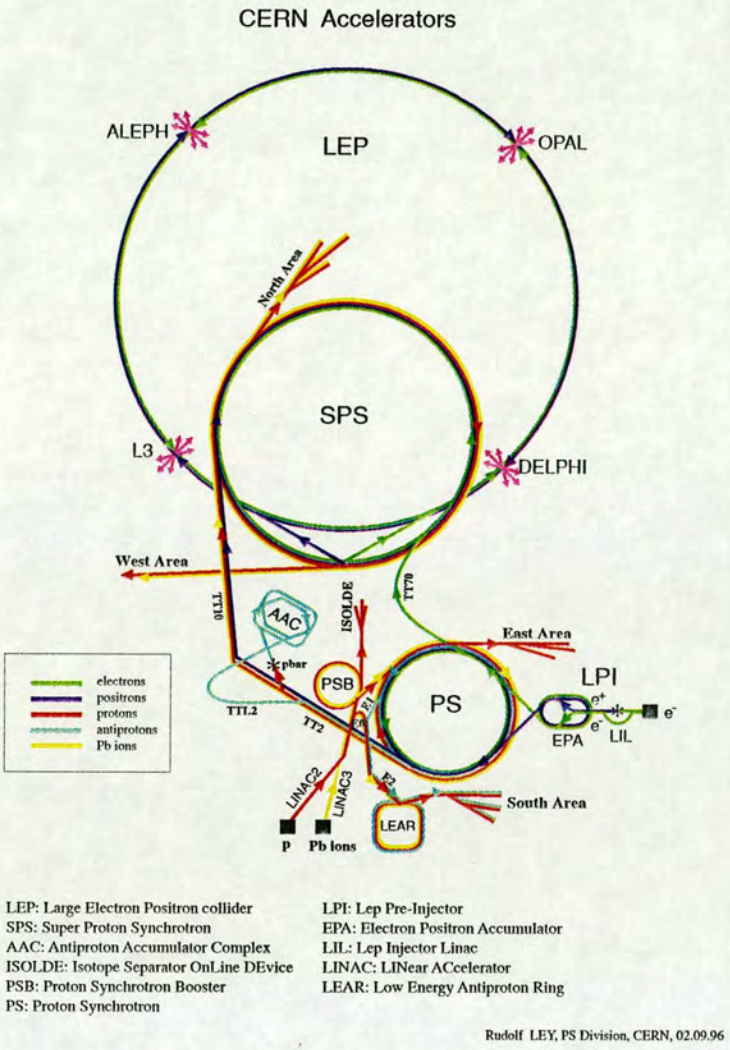

Figure 2.2: CERN accelerators.

precision of 10^{-4}, it is necessary to collect about 5×10^6 $K_L \to \pi^0\pi^0$ decays, i.e. one order of magnitude more than the previous experiments NA31 and E731. In one year, considering 120 effective days and an efficiency of 50%, 1.5×10^6 K_L decays will be collected; in three years, the necessary amount of data will be recorded.

NA48 will be able to operate at a frequency of 1 MHz, obtained with 1.5×10^{12} protons per pulse (ppp) on the K_L target.

2.1.3 Systematic error

It is mostly the systematic error which limits the precision attainable on the measurement of R. In fact, due to different beam divergences, energy spectra

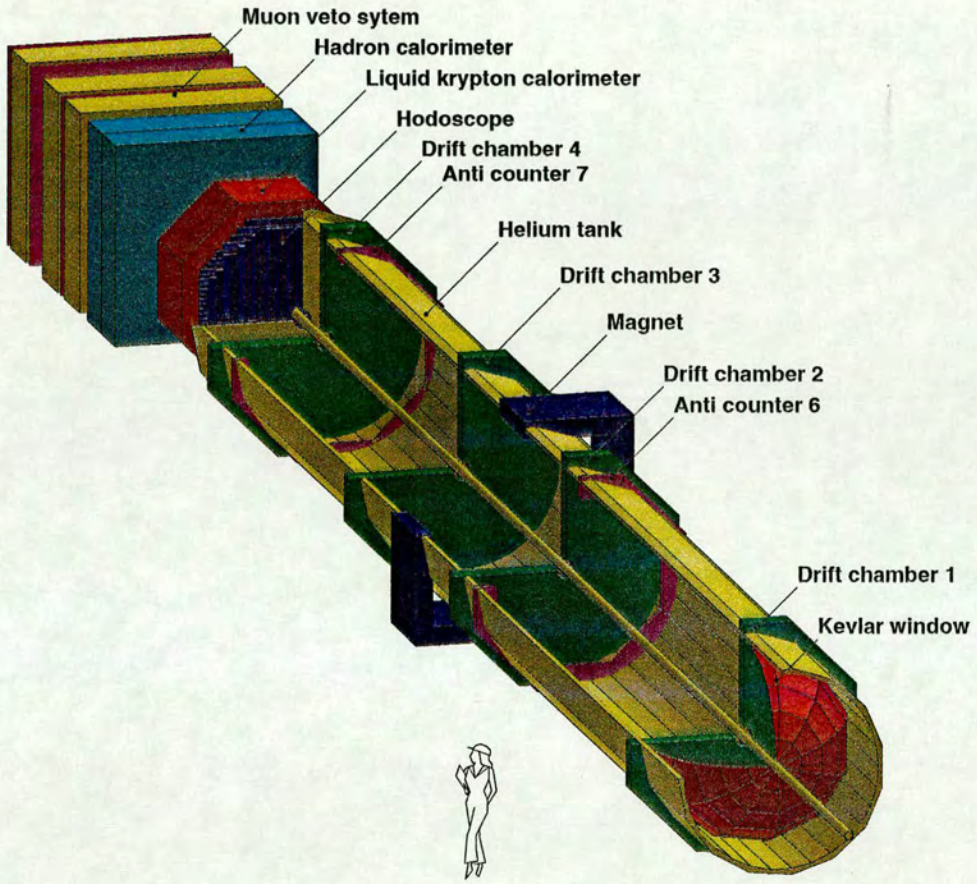

Figure 2.3: The NA48 detector.

and decay vertex positions, the acceptances of K_L and K_S decays are not the same. In order to have a negligible difference in momentum spectra, the production angles of the K_L and K_S beams have been carefully chosen (2.4 and 4.2 mrad respectively). This way, the decay spectra are similar when the kaon momentum is between 70 and 170 GeV/c, as shown in fig. 2.4 and 2.5.

Due to different lifetimes, the distribution of vertex decays is flat for K_L

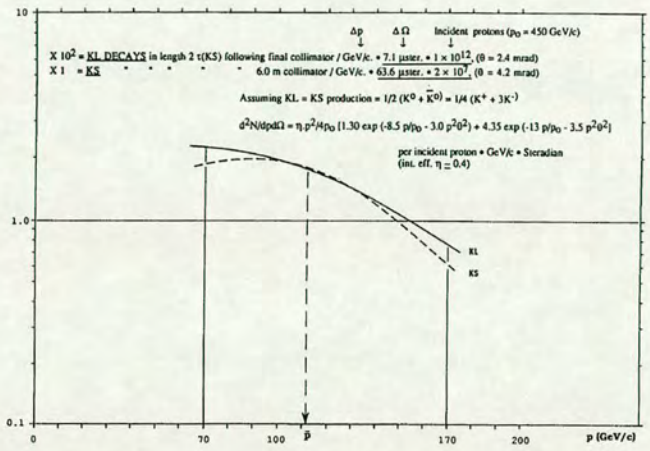

Figure 2.4: Decay spectra for K_L and K_S.

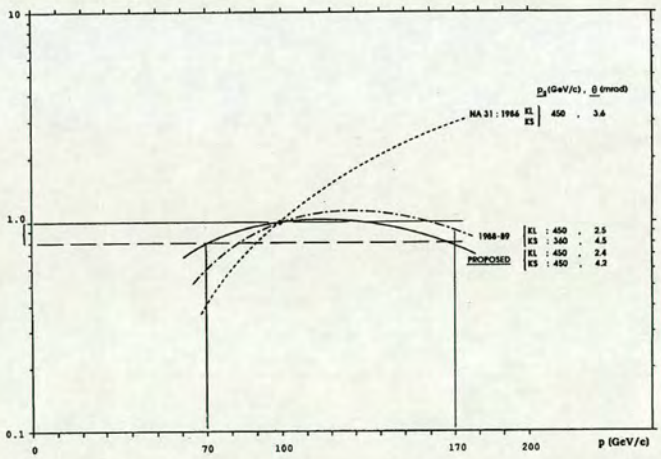

Figure 2.5: The solid line shows the ratio between the K_L and K_S decay spectra. It has the same values at 70 and 170 GeV.

and exponential in the case of the K_S beam, as shown in fig. 2.6. It is for this reason that a weight W, depending on kaon momentum p and on the longitudinal coordinate z of the kaon decay vertex, will be applied to K_L

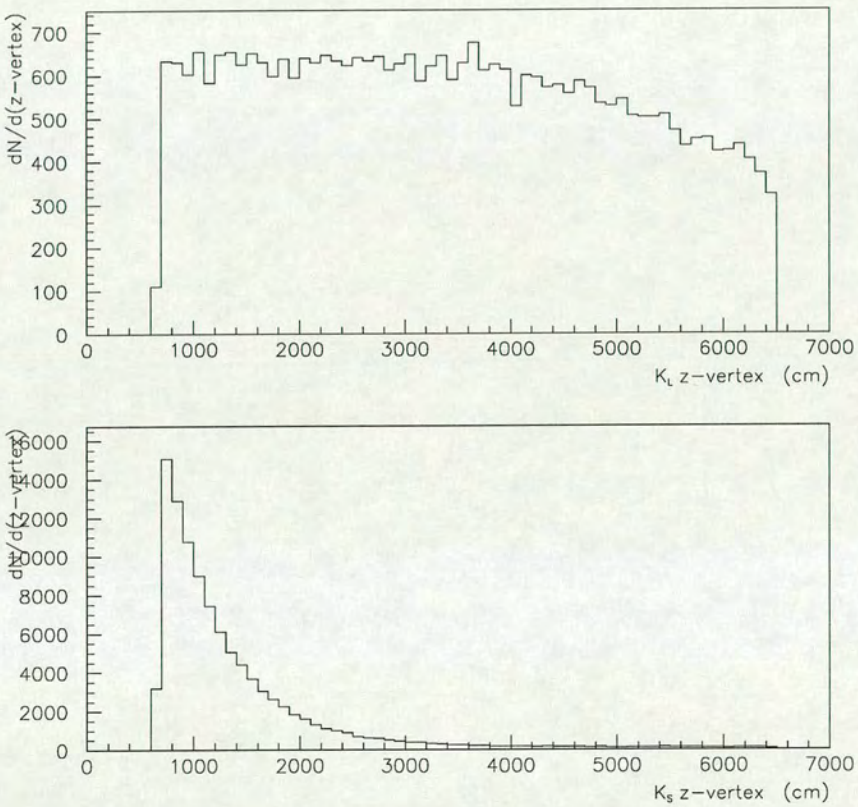

Figure 2.6: Distribution of the longitudinal vertex coordinates for K_L (above) and K_S (below). From 1995 data.

events:

$$W(p,z) = e^{-z \cdot m_K / p \cdot c\tau'}, \tag{2.3}$$

where $\tau' = \tau_S/(1 - \tau_S/\tau_L)$, and $\tau_{S(L)}$ denotes the mean life of the short (long)-lived kaon. Using this technique, the spatial distribution of K_L decay vertices reproduces that of the K_S beam. However, the use of the weight W increases the statistical error by about 15%. Thus, the double ratio R in eq. (1.87) can be written as a function of kaon momentum:

$$\mathrm{R}(p) = \sum_z \frac{N_L^{00}(p,z)a^{00}(p,z)W(p,z)}{N_S^{00}(p,z)a^{00}(p,z)} \cdot \frac{N_S^{+-}(p,z)a^{+-}(p,z)}{N_L^{+-}(p,z)a^{+-}(p,z)W(p,z)} \tag{2.4}$$

where $a^{00}(p,z)$ and $a^{+-}(p,z)$ denote the acceptances of the neutral and charged decay modes respectively, as functions of kaon momentum and longitudinal vertex position.

The longitudinal decay vertex position z of a $K \to \pi^0\pi^0$ can be computed from the energies E of the four photons given by the decay of π^0 and their positions x and y on the surface of the detector:

$$z = \frac{1}{m_K}\left\{\sum_{i,j<i} E_i E_j \left[(x_i - x_j)^2 + (y_i - y_j)^2\right]\right\} \tag{2.5}$$

where the subscripts i and j denote the four photons.
A difference in the reconstructed energy makes the longitudinal vertex position vary. This affects the number of events in each bin of z and p, so affecting the double ratio R as well. The value of energy is given by an electromagnetic calorimeter in case of neutral events, and by a magnetic spectrometer for charged ones. The two detectors must then be very carefully calibrated, in order not to introduce a systematic effect in the computation of R.

Background events, mainly three-body decays, are another important source for systematic errors. In case of neutral events, the decays $K \to \pi^0\pi^0\pi^0$ are rejected by using anticounter rings which veto photons outside the fiducial region, and an electromagnetic calorimeter with excellent resolution in energy and space.
The background of charged events is given by $K_L \to \pi^\pm e^\mp \overset{(-)}{\nu}$, $K_L \to \pi^+\pi^-\pi^0$ (called $K_{3\pi}$), and by $K_L \to \pi^\pm \mu^\mp \overset{(-)}{\nu}$ ($K_{\mu 3}$). The information of the muon-veto counters, located at the rear end of the detector, is used at the trigger

level to reject $K_{\mu 3}$ events. The invariant mass is reconstructed at the trigger level as well, in order to discard $K_{3\pi}$ decays and K_{e3} (at 90% level).

2.2 THE K_L AND K_S BEAMS

The NA48 experiment compares the $\pi^0\pi^0$ and $\pi^+\pi^-$ decays rates from distinct K_L and K_S beams which enter a common decay region along a path entirely contained in vacuum. The two decay modes are thus recorded at the same time and from the same fiducial length. The two beams are nearly collinear, converging at an angle comparable with the beam divergence (see fig. 2.7).

A proton beam (momentum 450 GeV, intensity 10^{12} protons per pulse)

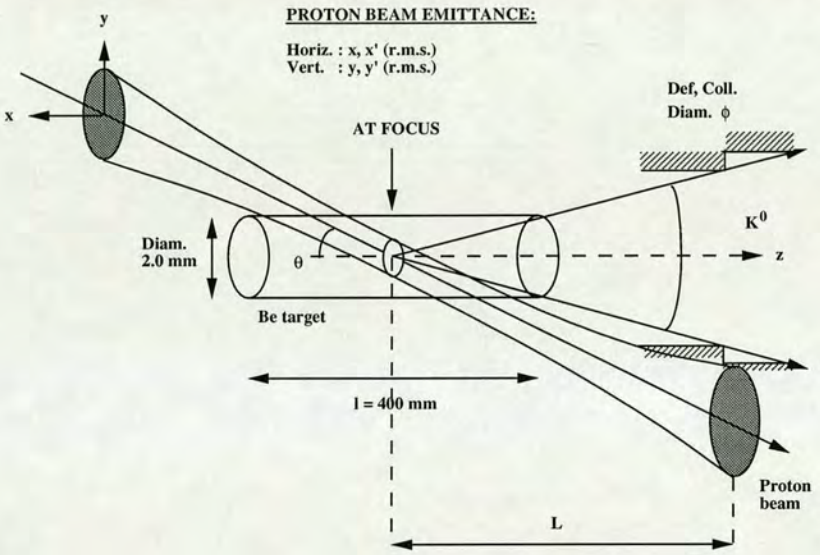

Figure 2.7: K_L and K_S beam definition.

strikes a beryllium target, producing the K_L beam at an angle of 2.4 mrad. After a first collimator which limits acceptance, charged particles (including the remaining primary protons) are deviated from the K_L line by a sweeping magnet. A fraction of the primary protons (about 3×10^7 ppp) is channelled back towards the K_L beam by a bent silicon crystal [26] (see fig. 2.8); passes through a tagging counter, and is eventually deflected and focused on the K_L line. It then hits a second target, placed 72 mm above the first one and at

a distance of 120 m from it, to produce a K_S beam at an angle of 4.2 mrad. This beam is defined by a collimator and converges with the K_L one at an angle of 0.6 mrad. The exit of the K_S collimator coincides with the last of three collimators designed to define the K_L beam, so that background from the collimators themselves cannot reach the detector. After the K_S collimator, a set of a lead converter, three scintillation counters and an anticounter with a central hole (a subdetector called AKS) vetoes K_S decays occurred before the collimator exit, and defines the fiducial region.

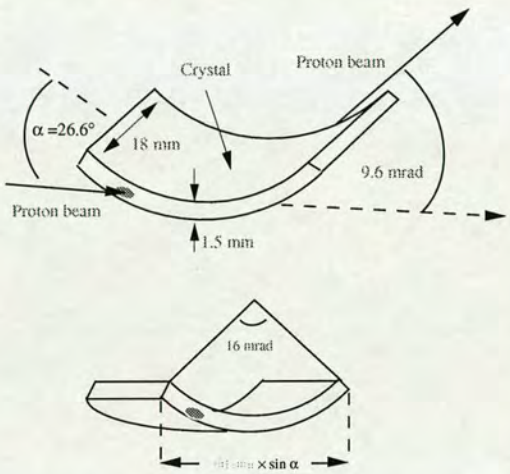

Figure 2.8: The silicon crystal, which channels a fraction of the primary protons onto the K_S target.

After the AKS, the two beams enter a cylindrical container (the *decay region*) 88 m long, where the pressure is kept below 1 μbar in order to minimise interactions. A thin kevlar window then separates the vacuum tank from a region filled with helium at atmospheric pressure. It contains the magnetic spectrometer, and terminates with an aluminium window before the charged hodoscope. The centre of the kevlar window is traversed by a beam pipe, which transports in vacuum the two beams through the various components of the detector until they reach a profile and intensity monitor, and eventually a beam dump, situated at about 250 m from the K_L target. The characteristics of the beams are given in table 2.1.

	Simultaneous, nearly-collinear beams of		
	K_L	+	K_S
Protons per pulse on target:	$1.5 \cdot 10^{12}$		$3 \cdot 10^7$
Spill ~ 2.5s, Cycle time 14.4s.			
Momentum p_0 (GeV/c)	450		450
Production angle (mrad)	2.4		4.2
Length of beam:			
target to last collimator/AKS (m)	126.0		6.07
last coll. to photon calorimeter mid-plane (m)		115.10	
Angle of convergence to K_L beam (mrad)	—		0.6
Angular acceptance of K^0 beam (mrad)	± 0.15		± 0.375
Radius of beam at detector (mm)	36 ± 5		45 ± 25
Radius of beam passage (mm) WC, LKr		76, 80	
K^0 momentum range accepted, p (GeV/c)		$70 < p < 170$	
Fiducial length for decays (m)		$15 < 4\tau_s < 36$	
at mean momentum $\langle p \rangle$ (GeV/c)		~ 110	
Total K^0 per pulse at exit last coll.	$\sim 2 \cdot 10^7$		$\sim 2 \cdot 10^2$
Total K^0 per pulse of accepted p	$6.4 \cdot 10^6$		$\sim 1.5 \cdot 10^2$
and decaying in fiducial length	$4.4 \cdot 10^4$		$1.5 \cdot 10^2$
to $\to \pi^0\pi^0$	40		45
Detector acceptance for decays		~ 0.2	
Useful decays per pulse: $K^0 \to \pi^0\pi^0$	8		9
" " per hour "	$2.0 \cdot 10^3$		$2.3 \cdot 10^3$
" " per year "	$2.9 \cdot 10^6$		$3.3 \cdot 10^6$
(120 days with eff. 0.5)			
Counting rates:			
Incident protons on target (s^{-1})	$1.0 \cdot 10^{12}$		$2 \cdot 10^7$ tagged
K^0 decays into detector (s^{-1})	$\sim 9 \cdot 10^5$	+	$\sim 1.4 \cdot 10^2$
μ's through detector (s^{-1})	$\sim 1.5 \cdot 10^5$	+	$\sim 10^3$
Background from target + dump			
Total rate detector (s^{-1}) Q_{OR}:	$\sim 1.5 \cdot 10^6$	+	$\sim 10^5$
(from 1995 rates)			

Table 2.1: Characteristics of the combined K_L and K_S beams. 1996 values.

2.3 Tagging: Was it a K long or a K short?

In order to decide whether an event originates from the K_L or the K_S beam, the time difference between the passage of the proton in counters upstream of the K_S target (see fig. 2.9) and the event time in the detector is measured. Events having this time difference within a time interval Δt are identified as "K_S", otherwise as "K_L" decays. The event time for charged events is given by a hodoscope placed before the electromagnetic calorimeter; in case of neutral decays, this information is provided by a hodoscope placed inside the calorimeter itself. In the case of $\pi^+\pi^-$ events, the information provided by the spectrometer allow a precise reconstruction of the vertex position, as shown in fig. 2.10, thus enabling the identification of an event as K_L or K_S. This redundancy allows the measurement of the efficiency of the tagging system.

An accidental signal in the tagging counters leads to a misidentification of a K_L event as K_S. The probability of such a $K_L \to K_S$ "transition" is the same for charged and neutral events, and does not depend on time resolution. Its only effect is a dilution of the value of ε'/ε, which can be corrected.

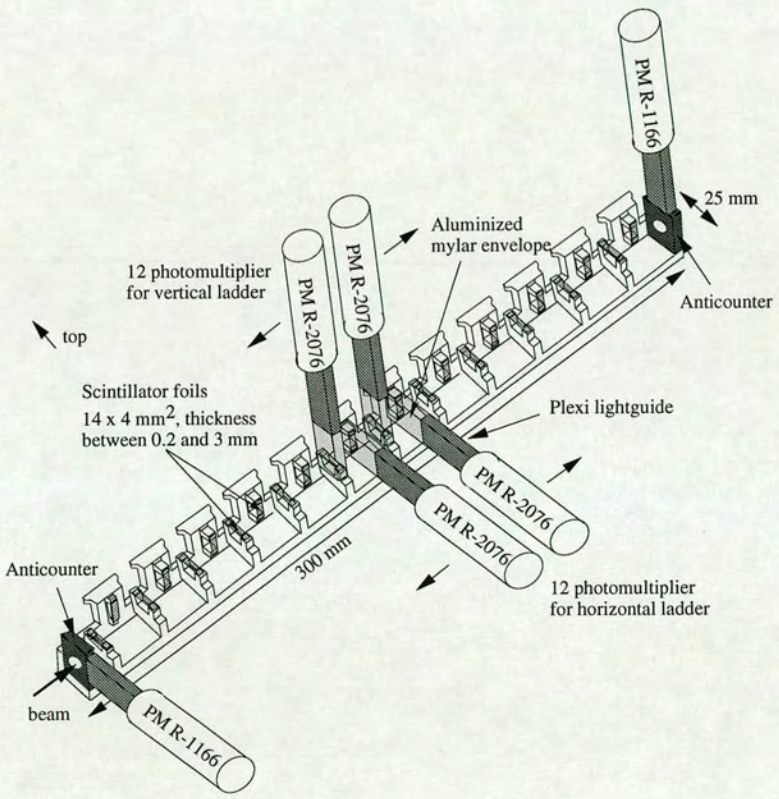

Figure 2.9: The proton tagging counter.

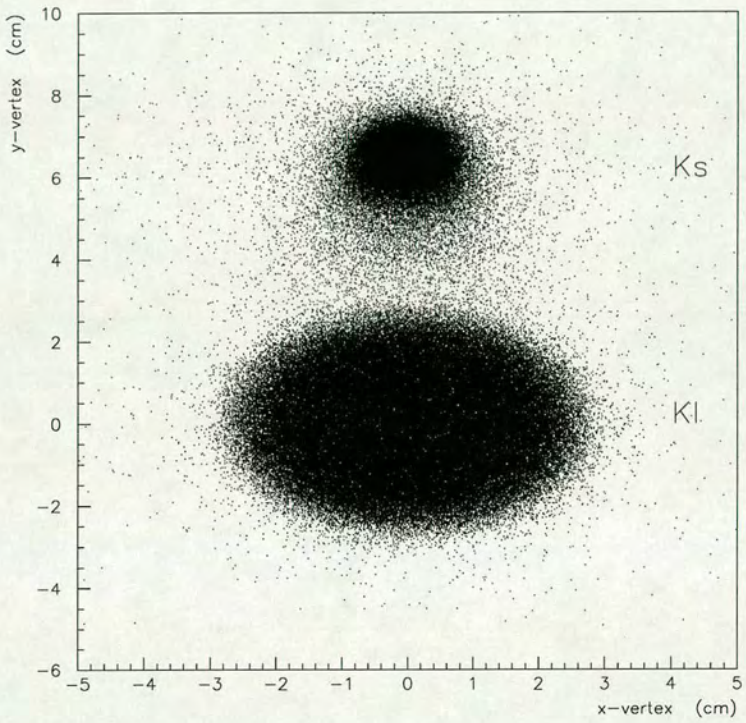

Figure 2.10: Position of the decay vertex of charged events, in the (x, y) plane. The two beams are clearly identifiable (1995 data).

Any tagging inefficiencies or wrong event time measurements give a $K_S \to K_L$ transition. Tagging misidentifications do not depend on the decay mode. Since the event time of neutral and charged events is provided by different detectors, the probabilities of a $K_S \to K_L$ transition in this case are different for $\pi^+\pi^-$ and $\pi^0\pi^0$ decays. This effect can generate a non-zero value of ε'/ε. Thus, the time window has to be wide enough compared to the time resolution of the 'tagger + detector' system, to prevent errors given by small differences in time resolution between charged and neutral events. At the same time, such interval has to be conveniently small in order to minimise the effect given by accidental events. The required resolution is better than 500 ps.

2.4 Background Rejection

2.4.1 Anti-counter Rings

Events with four photons detected in the electromagnetic calorimeter, but with other photons escaping the acceptance of the detector (typically, $K_L \to 3\pi^0$, BR $\simeq$ 22%), are rejected using the information provided by seven anti-counter rings, placed around the vacuum pipe which defines the decay region. Their geometrical acceptance (polar angle $\geq$ 10.35 mrad) is thus complementary to that of the detector itself (see fig. 2.11). Each anti-counter consists of 24 (the first four rings) or 16 (the remaining three) scintillators arranged in two layers, as shown in fig. 2.12, and preceded by 3.5 cm of iron to increase photon conversion probability.

2.4.2 Muon-Veto Counters

A substantial contribution to the background for $K_L \to \pi^+\pi^-$ decays is given by $K_L \to \pi^\pm\mu^\mp \overset{(-)}{\nu}$ events, whose branching ratio is about 27%. These decays are rejected at trigger level using the information provided by the μ-counters, located at the end of the beam line. A total of 28 scintillator strips are arranged in three planes of 2.7×2.7 m^2, preceded by an iron layer 80 cm thick (see fig. 2.13). The strips are alternatively vertical and horizontal, partially overlapping, and equipped with photomultipliers on both sides. A signal in the first two planes gives the 1μ trigger signal, whose efficiency

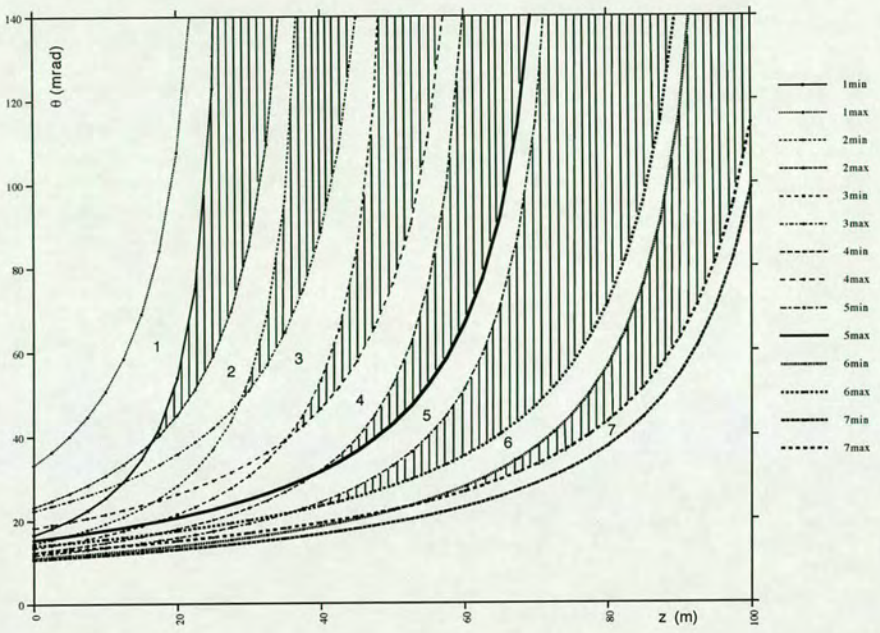

Figure 2.11: Anti-counter rings angular coverage, as a function of the decay vertex longitudinal coordinate. The shaded regions are not covered.

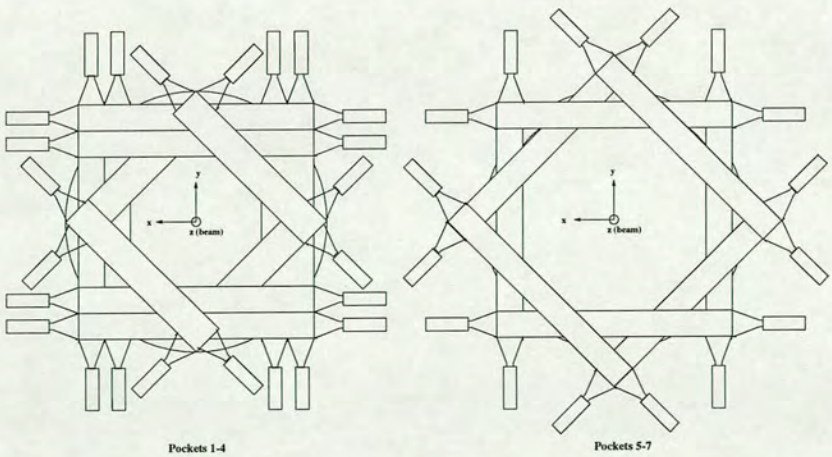

Figure 2.12: The anti-counter rings.

has been measured using the signal provided by the third plane and the information from the hadronic calorimeter. It has been found to be nearly 100% [27].

2.4.3 Hadron Calorimeter

The most important task of this subdetector is to provide an energy threshold signal which is part of the trigger, and is used to reject background coming from $K_{\mu 3}$ and K_{e3} events. The front and back modules of the hadronic calorimeter (fig. 2.14) consist of alternate iron and scintillator planes. Each scintillator plane has 44 strips, arranged vertically and horizontally to form quadrants. Vertical or horizontal strips in each module are connected to the same photomultiplier, giving an overall number of 176 readout channels. The energy resolution of the hadron calorimeter is $65\%/\sqrt{E}$.
During the 1995 data-taking period, the electromagnetic calorimeter was still in preparation. For this reason, the hadron calorimeter provided the only particle identification information.

2.5 The Magnetic Spectrometer

Two sets of drift chambers on each side of a central dipole magnet (see fig. 2.15) provide a measurement of charged particles momenta. Each chamber has four views X, Y, U and V, tilted 45°; each view consists of two planes of 256 wires, at a distance of 1 cm from each other, to avoid ambiguities in the position measurement. The spatial resolution of each view is $\simeq 100$ μm, which corresponds to $\Delta p/p = 0.6\%$ accuracy on momentum measurement. The diameter of the beam pipe central hole is 160 mm.
The field integral of the main field component (B_y) is $\oint B\mathrm{d}l = 0.83$ Tm, and is equivalent to a transverse momentum change of 250 MeV/c. The magnet is shown in fig. 2.16.
The decay vertex longitudinal coordinate and the invariant mass of the event, reconstructed by the magnetic spectrometer, are used at the trigger level to select two-pion events.

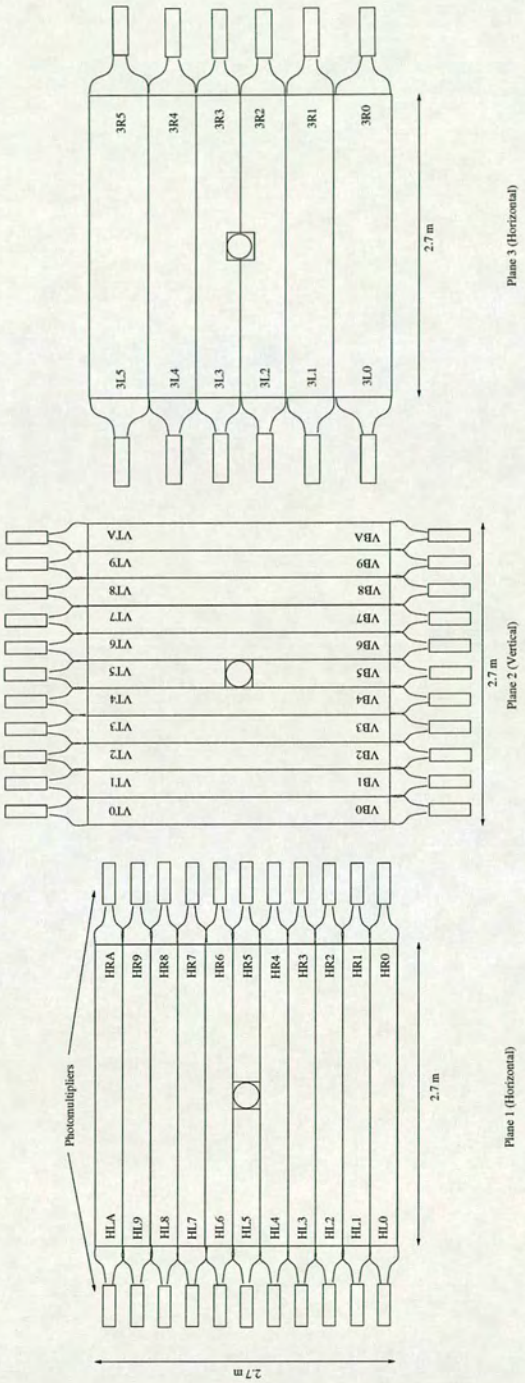

Figure 2.13: The muon veto counters.

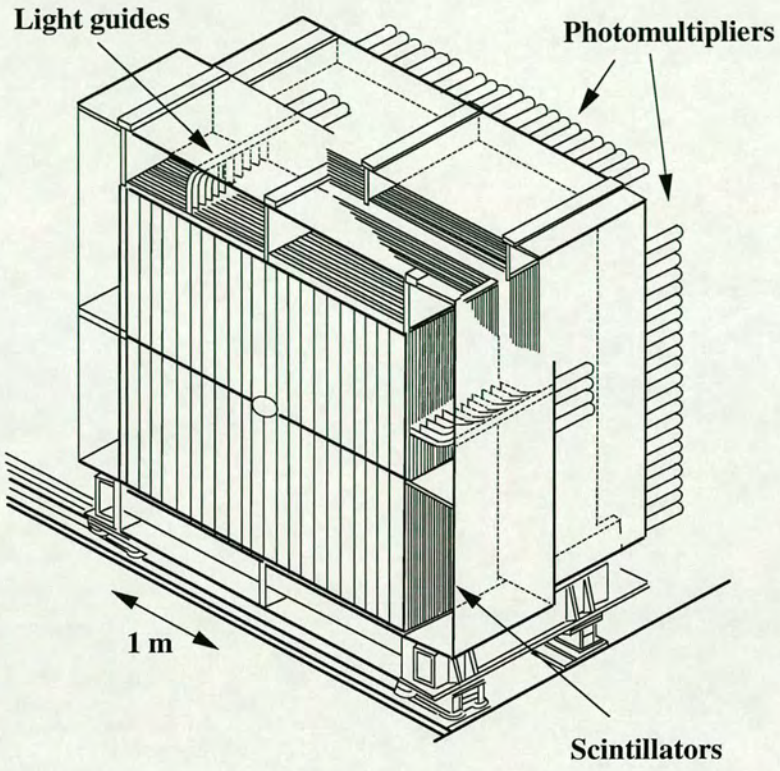

Figure 2.14: The hadronic calorimeter.

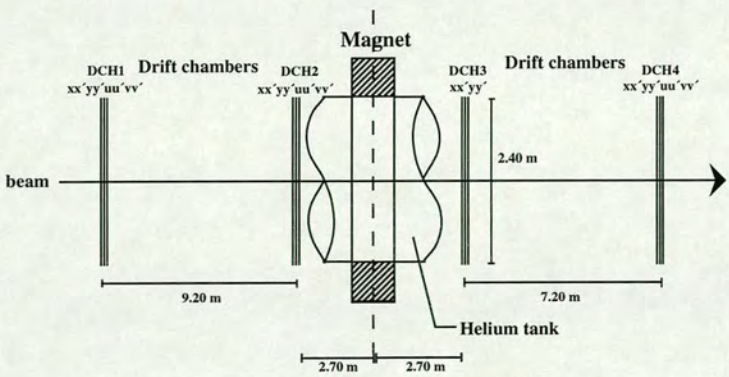

Figure 2.15: The magnetic spectrometer.

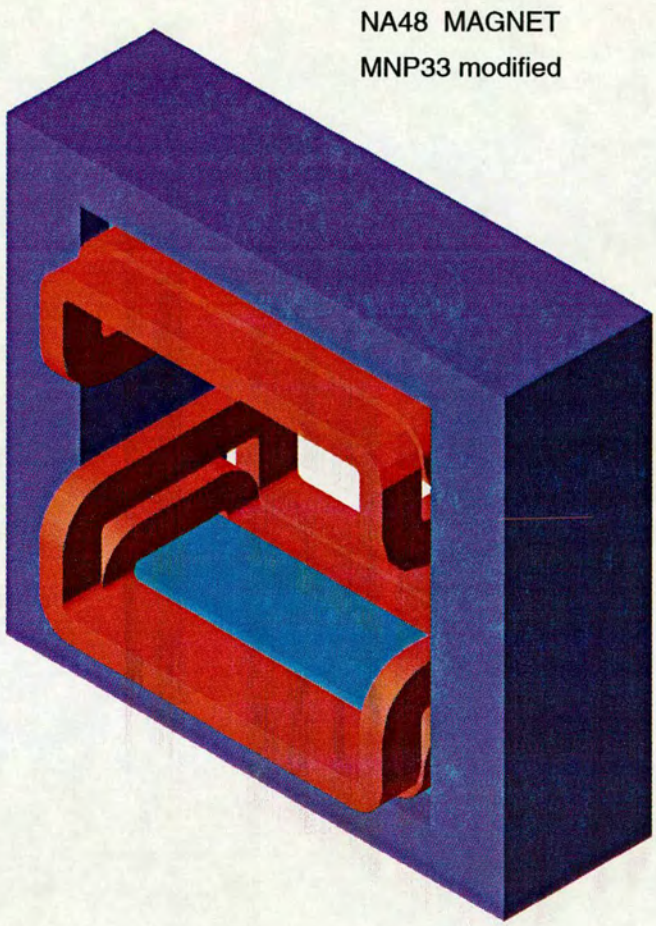

Figure 2.16: The NA48 magnet (MNP33).

2.6 The Event Time Measurement

2.6.1 Charged Hodoscope

The information provided by this detector is used to identify the K_L or K_S origin of charged decays, and in the trigger to select two-body decays (table 2.2).

Two planes of scintillator counters, at a distance of 50 cm, are located

Charged Hodoscope Signals	
ORH	OR of all horizontal counters
ORV	OR of all vertical counters
TOTAL OR	OR of all hodoscope counters
COINCIDENCES	$(QV_1 + QH_1) + (QV_2 + QH_2) + (QV_3 + QH_3) + (QV_4 + QH_4)$
Q_x^{13}	$(QV_1 + QH_1) \cdot (QV_3 + QH_3)$
Q_x^{24}	$(QV_2 + QH_2) \cdot (QV_4 + QH_4)$
Q_x	$Q_x^{13} + Q_x^{24}$

Table 2.2: Charged hodoscope trigger signals. Notation: QV_n (QH_n) means OR of the vertical (horizontal) counters of the n-th quadrant.

after the magnetic spectrometer along the beam line (see fig. 2.17). Each plane consists of 64 scintillators, arranged vertically in the first one and horizontally in the second, and is divided four into quadrants. The width of the scintillator strips ranges from 6.5 cm to 9.9 cm according to their distance from the centre of the plane, and their thickness is 2 cm.

2.6.2 Neutral Hodoscope

Situated at a depth of 9.5 radiation lengths inside the electromagnetic calorimeter, the neutral hodoscope provides a time measurement of neutral events independent of the calorimeter itself, making use of a much smaller number of channels.

This detector consists of 256 sets of 25 scintillating fibres each. In the central part of the detector each photomultiplier reads 10 sets, while the side sets will be read in groups of 22.

The performance of the electromagnetic calorimeter is not affected by the

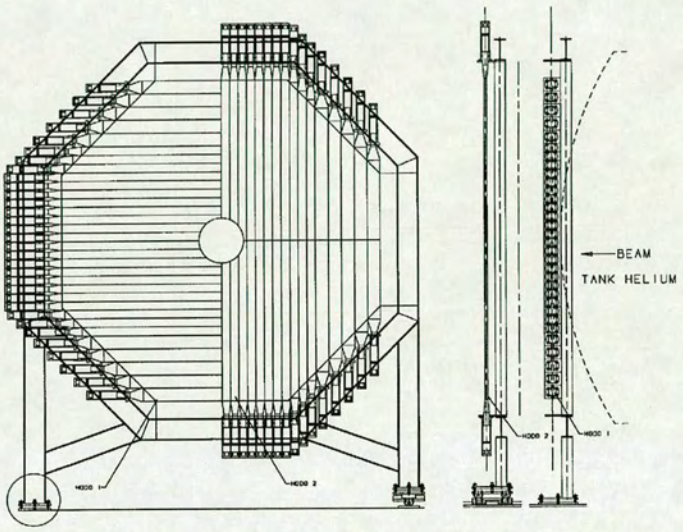

Figure 2.17: The charged hodoscope: front view of two half-planes and side view of both planes.

presence of the neutral hodoscope, whose measured time resolution is below 300 ps (beam energy $\geq$ 15 GeV).

2.7 Electromagnetic Calorimeter

A fast liquid krypton (LKr, radiation length = 4.8 cm, Molière radius = 4.7 cm) calorimeter has been designed for the detection of photons from π^0 decays. Its main requirements are the capability of recording multi-photon events at a rate of $\approx$ 1 MHz with a space resolution of about 1 mm, and an excellent energy resolution ($\sim 3\%/\sqrt{E}$ plus a constant term smaller than 0.5%).

To achieve these goals, a quasi-homogeneous ionization chamber has been developed. Sampling fluctuations are small, due to the use of krypton both as converter and detection medium. Copper-beryllium electrodes are arranged in a 2×2 cm^2 tower read-out structure. The towers are parallel to the beam direction. The active volume is an octagon, whose width and depth are 2.6 m and 1.2 m respectively. It comprises 13500 read-out channels, immersed in 8 m^3 of liquid krypton. High-speed read-out of the detector signal is possible owing to the low cell capacitance (80 pF) and to the use of preamplifiers with short connections. Initial current read-out technique will be used, and all pulses will de digitised with 40 MHz flash ADCs.

A prototype calorimeter of 184 cells has been tested with three different electrode structures [28, 29, 30, 31], to achieve a sufficiently uniform response within a cell. The chosen structure is shown in fig. 2.18. The read-out structure is based on *ribbon* electrodes stretched between two end-plates. Each cell is formed by a central anode and by two cathodes at 10 mm distance on each side of the anode. The cathodes are shared between horizontally adjacent cells. Longitudinally, the correct spacing between the electrodes is enforced by slotted plates. These *spacer-plates* push the ribbons alternatively from the right and the left side, positioning them at angles of about $\pm$50 mrad from the detector axis (see fig. 2.19). This *zig-zag* applied to the geometry gives two advantages. Firstly, it reduces the length over which the electrodes are stretched, allowing to maintain their corrected spacing against electrostatic forces with a small tension. This permits the achievement of a satisfactory

uniformity of the cell geometry. Also, the zig-zag reduces the depth inside the detector along which a shower core may be close to an electrode, thus avoiding the loss of response for ionization deposited in the proximity of the electrodes.

The prototype calorimeter was exposed to an electron beam, whose energy

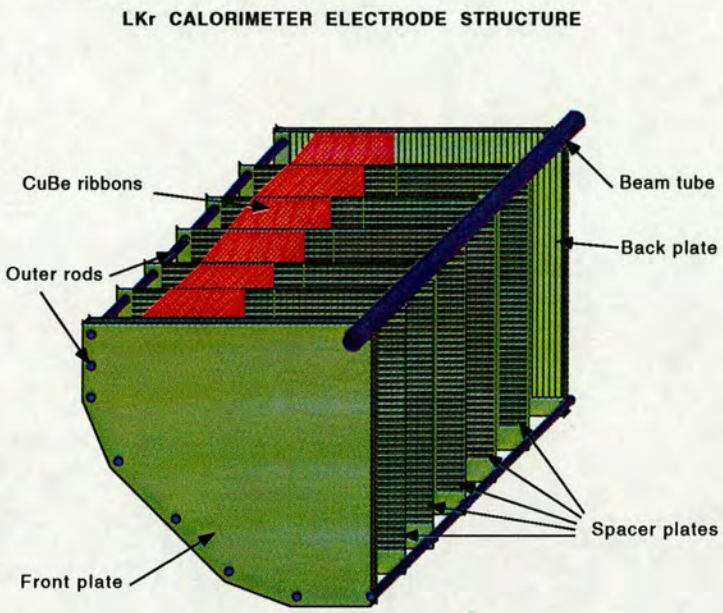

Figure 2.18: The electro-magnetic calorimeter electrode structure.

ranged from 8 to 80 GeV. The results met the expectations. The energy resolution can be parametrised as:

$$\frac{\sigma(E)}{E} = \frac{3.5\%}{\sqrt{E}} \oplus \frac{40\text{MeV}}{E} \oplus 0.42\% \tag{2.6}$$

where energy is measured in GeV and $\oplus$ denotes addition in quadrature.

The space resolution was obtained by comparing the position of the centre of gravity (COG) of the shower in the calorimeter with the electron impact point as reconstructed by the drift chambers. The COG was calculated using a 3×3 shower box and corrected for the non-linear dependence on the impact point within a cell. The space resolution as a function of beam energy is

$$\sigma_x = \left(\frac{4.2}{\sqrt{E[GeV]} \oplus 0.6} \right) \text{mm}; \quad \sigma_y = \left(\frac{4.3}{\sqrt{\text{E[GeV]}} \oplus 0.6} \right) \text{mm}. \tag{2.7}$$

The determination of the shower time was performed applying a digital filtering approach to the data stream [32]. The required coefficients were determined by a data sub-sample, optimising the response of the calorimeter

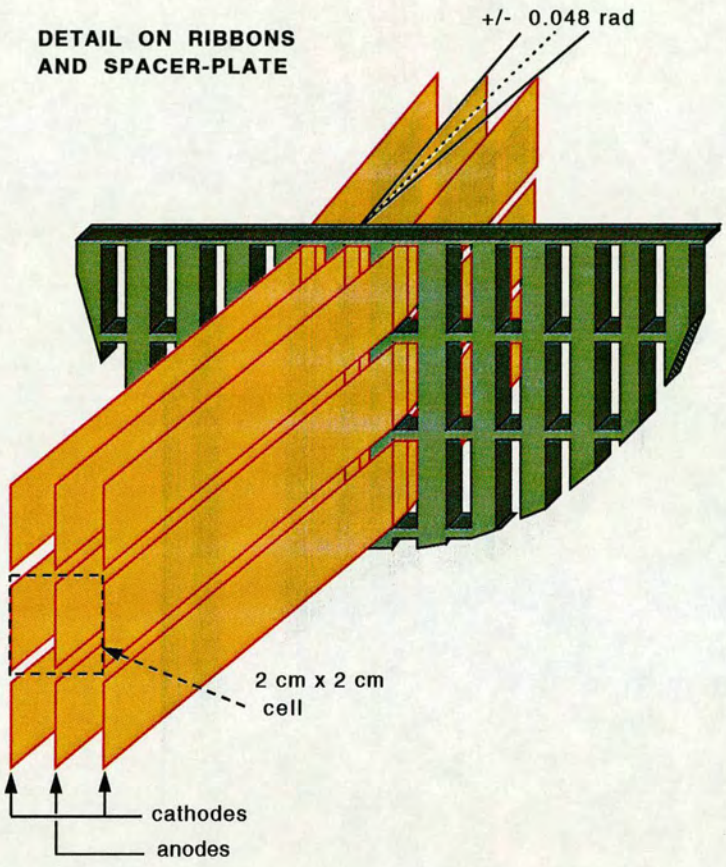

Figure 2.19: The electromagnetic calorimeter ribbons and spacers.

relative to a scintillation counter. The time resolution is better than 275 ps for shower energies above 15 GeV.

2.8 The Trigger

Due to the required high accuracy on the measurement of ε'/ε, a very high statistics data sample and a very good knowledge of the systematics are needed. This fact poses very hard requirements on the trigger and data acquisition systems, which is almost fully pipelined, in order to guarantee a very small dead time fraction at very high rates. In such a way, no biases between the charged and the neutral trigger are introduced.
The NA48 trigger system is subdivided into two hardware levels and in a software one. The information in each subdetector system is continuously digitised at a frequency of 40 MHz, and stored in digital circular memory buffers, where it resides for a maximum of 200 μs. In the meantime, the Local Trigger Systems (LTSs) continuously give partial decisions for each 25 ns *time slice*, based on the information from a given subset of the detector.

The **first level trigger**, a fast pipelined hardware system, uses information provided by the charged hodoscope, the anticounter rings, the muon counters, the first drift chamber and by the calorimeters. A *pre-trigger* signal [33] is given by the coincidence of two opposite quadrants of the charged hodoscope, which provides the event time. The task of the pre-trigger is to start the charged trigger system.
The purpose of the **Level 1 Trigger Supervisor** (L1TS, shown in fig. 2.20) is to identify likely two-body charged decays so as to limit the rate in the second level trigger. The L1TS receives information from the above-mentioned subdetectors and determines whether an invariant mass calculation is required. The output of the L1TS consists of the trigger code which describes the trigger type, and the time of the event relative to the burst (the so-called *time stamp*). For accepted events, a request is inserted into the second level queue, along with the time stamp. It enables the second level trigger to calculate the invariant mass of the charged particles from the drift chambers information.

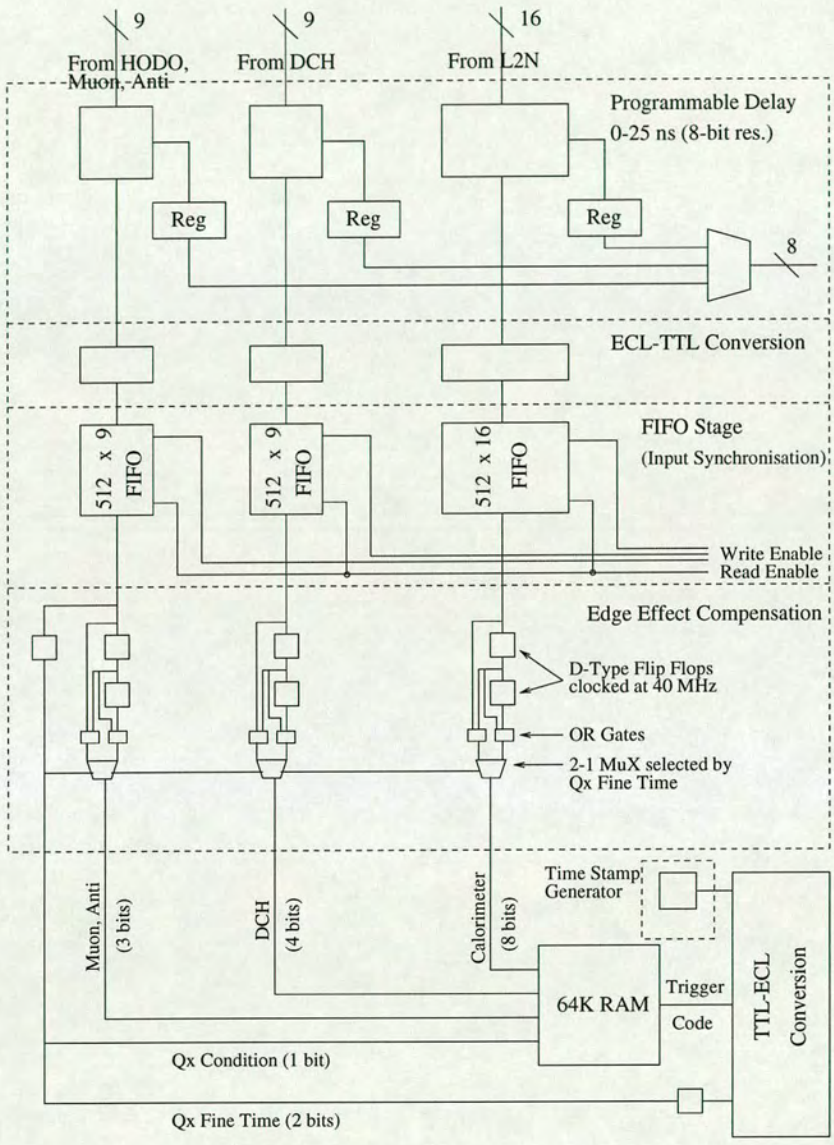

Figure 2.20: The Level 1 Trigger Supervisor.

The **neutral trigger** [34] monitors the information coming from the liquid krypton calorimeter and signals to the read-out electronics whenever a $\pi^0\pi^0$ event has occurred. Its design is fully pipelined: every 25 ns, each step of the trigger processes the data from one time bin and passes it onto the next. The arrival of the result at the output of the pipeline occurs at a fixed time delay after the incoming calorimeter pulses. The time taken to perform the calculation is always the same.
Five main quantities are computed for each time bin and used to make the trigger decision: the number of 1-dimensional peaks in x and y views, the total energy, the centre of gravity, the vertex position of the decay and the proper lifetime of the kaon. Selection conditions are applied to these quantities to reduce background, especially coming from $K_L \to \pi^0\pi^0\pi^0$.
The neutral trigger notifies the trigger supervisor of its decision for any given time bin within a certain delay from the decay itself. The Level 2 Trigger Supervisor will store the results of the calculation until all signals from the other triggers have arrived and then correlate them.

The **second level charged trigger** (L2C, see fig. 2.21) [35] is a partially-pipelined system which computes the invariant mass and the vertex of the event. Following a request from level 1, it collects information from the drift chambers and performs mass and vertex calculation in parallel on several fast processors. Such an approach, while allowing for high power and flexibility, makes the system asynchronous, since the computing time - although guaranteed not to exceed a fixed limit of 100 μs - is not constant but depends on several parameters on an event by event basis. Once a conclusion concerning the processed event is reached, the time stamp and the results of the L2C computations are sent to the Level 2 Trigger Supervisor.

The **Level 2 Trigger Supervisor** (L2TS, see fig. 2.22) [36] is a fully-pipelined hardware system which has to correlate the trigger information coming from local trigger sources (level 1 charged trigger, neutral trigger, level 2 charged trigger), take the trigger decision and dispatch it to the

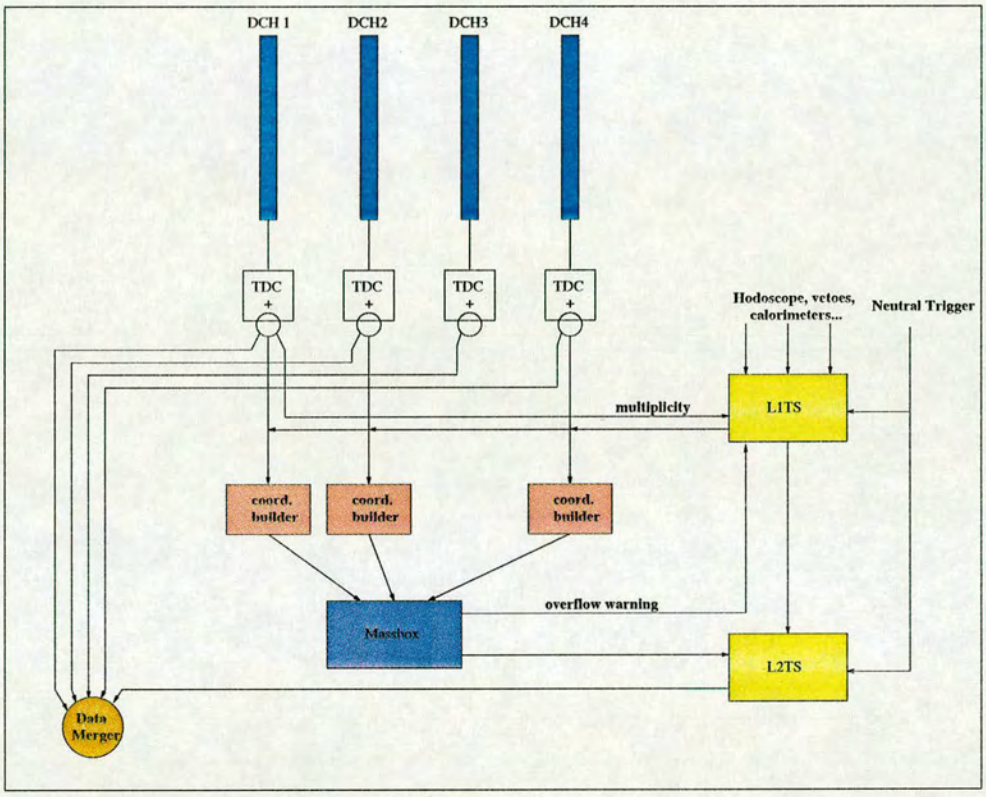

Figure 2.21: The Level 2 Charged Trigger.

Read-Out Controllers (ROCs) to initiate the read-out. In addition, it performs trigger counting and downscaling, dead time control in order to cope with anomalous conditions, random trigger generation and trigger monitoring. The L2TS receives both synchronous (i.e. produced at a fixed time delay with respect to the event time) and asynchronous information. For the synchronous trigger systems the time information is intrinsic and can be reconstructed inside the L2TS itself by dedicated 40 MHz counters. The asynchronous trigger (the L2C) also provides the time stamp, labelling each individual 25 ns time slice within a 2.5 s beam spill. At output stage, a trigger word, an event number and the corresponding time stamp are stored in a *trigger queue buffer* (TQB). The main purpose of the TQB is to derandomise triggers, in order to guarantee a fixed minimum time interval Δt (20 μs) between them. This allows the ROCs downstream (i.e. the read-out in each subdetector) to avoid trigger queues.

In order to avoid bottlenecks in the optical links for the electromagnetic calorimeter, it is desirable to have a strong rejection power in the dataflow scheme before data enter the optical links. The primary goal of the **Level 2B Trigger** (L2B) [38] is to complement the selection power of the main pipelined neutral trigger. It performs a first, rough reconstruction of the photons detected by the calorimeter; the pion masses are reconstructed for each pair of photons (all the possible combinations of photons are checked) and required to be consistent with the known pion mass. The L2B works entirely downstream of the other NA48 trigger systems, and acts only on event triggers which are issued by the Level 2 Trigger Supervisor. It is integrated into the sequence of the liquid krypton calorimeter read-out, and performs processing in parallel with the zero suppression of the calorimeter data.

A **third level trigger** is foreseen to impose additional criteria to select the events of interest. It consists of a software system which filters reconstructed data before recording onto tape.

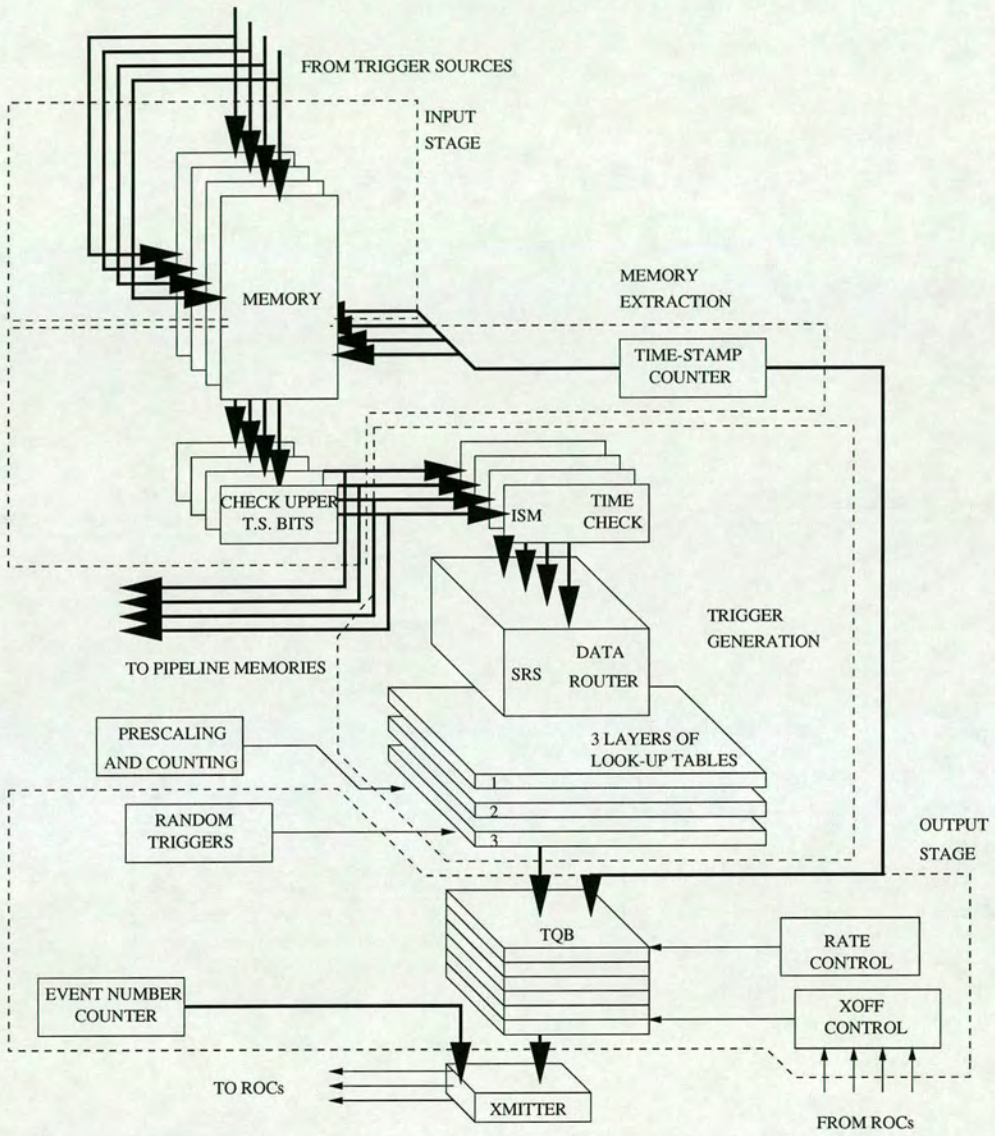

Figure 2.22: The Level 2 Trigger Supervisor.

2.9 Data Acquisition

The event rate following the level 2 trigger is about 5 kHz. The event length is dominated by the data coming from the electromagnetic calorimeter, and depends on zero suppression and data compression algorithms. The other detectors generate modest amounts of data for each trigger. The total typical event length can be estimated to be 10 kbytes. Taking into account the mentioned rate, 30 Mbytes/s have to be processed (equivalent to $\sim$ 75 Mbytes for each SPS burst). However, in order to cope with possible unforeseen inefficiencies (for example, if the trigger is not as good as expected), or to allow future developments (e.g. new trigger categories), the data acquisition system (DAQ) [39] has been designed to cope with 100 MBytes/s and a trigger rate of 10 kHz. These figures correspond to 25000 events per SPS burst.

The long distance (about 100 m) which separates the Read-Out Controllers from the Data Merger, where the event is assembled, forces the use of optical fibre transmission, and an **Optical Link** (OL) transmitter/receiver set [40] is used. The link is designed to transfer information at a rate of at least 10 Mbytes/s with a bit error rate of less than 10^{-14}, and provide electrical insulation. In general, each subdetector has one OL, except the electromagnetic calorimeter which requires 8 of them.
Through the OL, the output from the Read-Out Controllers is delivered to an *Input Buffer* (IB) which is part of the **Data Merger** (DM) [39]. The task of such a device is to collect all the information and concatenate them to form a *global event*, which is then sent to a workstation farm. Events are stored in the DM input buffer until required for read-out. There is one IB for each subdetector (i.e. for each Optical Link). The IBs are read out sequentially by the Output Formatter, which concatenates the sub-events and feeds the complete global event to the Front-End Workstations via a HIPPI (High Performance Parallel Interface) link.
The data to be distributed come in data-blocks, each comprising the data produced during a single SPS burst. The system is designed to handle 250 MBytes of data per SPS burst (assuming the use of the HIPPI links at their

theoretical maximum throughput of 100 MBytes/s over a 2.5 s burst). Each data-block is transferred from the Data Merger to one of the **Front-End Workstations** (FEWs) by a HIPPI switch, while the subsequent data-block will be transferred to another FEW. Each workstation is a DEC Alpha 3000 with 320 Mbytes of memory, and is equipped with a HIPPI/TURBOchannel interface. Fig. 2.23 shows a diagram of the data flow.

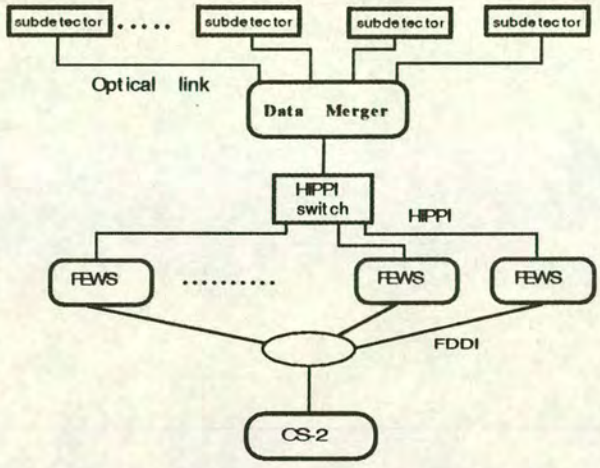

Figure 2.23: The NA48 data flow. The CS-2 system is described below.

2.9.1 The PMB data acquisition system

The read-out of the event time measurement detectors, of the AKS and the anti-counters is based on modules called **Pipeline Memory Boards** (PMBs). The signals from each subdetectors are collected by the PMB system, sampled, digitised and written into memory. Then, according to the L2TS decision, the information is transferred to a buffer and sent to the Data Merger via an optical link.

A particular PMB module, called PMB Pattern Unit, has been developed to process digital signals only. Its main purpose is to record trigger information and to monitor the neutral trigger and the trigger supervisor.

2.10 Central Data Recording

At their arrival on the FEWs, data are written to disk, possibly in a compressed format. In a traditional approach, these disk files would be immedi-

ately copied onto a tape unit attached to the DAQ system. Instead, a new approach to data recording is being pioneered by NA48.

2.10.1 The Meiko CS-2

A optical fibre link 5 km long has been installed to connect the CERN North Area, where NA48 resides, to the CERN computer centre, to transfer the data in real-time to a 64-node Meiko **CS-2** system [37]. Each node of such a distributed-memory architecture consists of a twin-processor board equipped with two 100 MHz Sparc processors, 128 MBytes of memory and 1 GByte of disk. The nodes are interconnected by a high-performance (50 MBytes/s) low-latency ($\leq 10\mu s$) network. The working environment for the end-user is a familiar UNIX (SUN Solaris operating system). The configuration of the machine is shown in fig. 2.24.

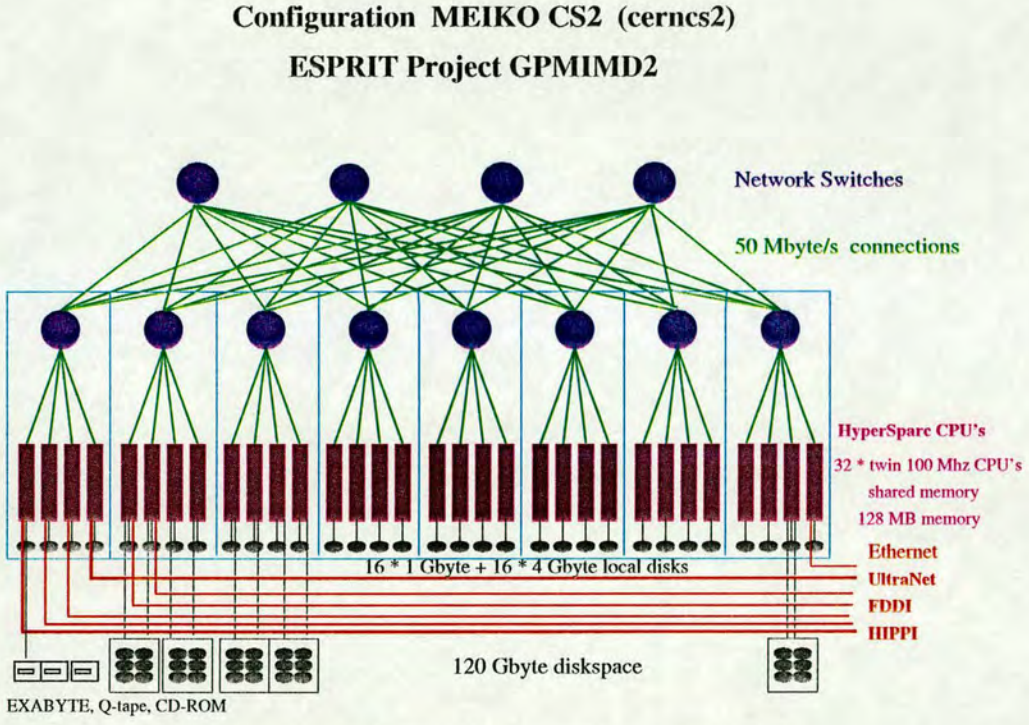

Figure 2.24: The Meiko-CS2 configuration.

2.10.2 Data Archival

Each Front-End Workstation is equipped with its own FDDI (Fibre Distributed Data Interface) interface, connected to a FDDI concentrator. Dur-

ing the data-taking period in 1995, for the first time data were sent to the CS-2 over a FDDI link, with a measured bandwidth of 9 MBytes/s. The average data recording rate was 2.5 MBytes/s (whereas a rate of 19 MBytes/s is foreseen for the final configuration, with the electromagnetic calorimeter). On the CS-2, data were written on 8 Parallel File Systems (PFSs). Each PFS consisted of 4 disks for a total of 10-12 GBytes, with a transfer bandwidth of 8-10 MBytes/s. The 32 disks were attached to 12 CS-2 processors, fully dedicated to data recording and to a first real-time check of the data quality. The subsequent step was to transfer data from disk onto magnetic tapes. Digital DLT 2000 tapes have been used so far. Several PFS have been used in order to spread the load over more nodes and to increase system resilience to disk or tape unit failure. The Central Data Recording (CDR) scheme is shown in fig. 2.25. Most of the rest of the CS-2 disk space was used as circular buffer, allowing to keep data on disk for about 12 hours. This gave the possibility to detect and solve possible problems with the data recording system. A careful *book-keeping* is necessary, to record when each file has been transferred from the experimental site to the Computer Centre, and onto which tape it has been archived, as well as to keep track of possible problems. Such a system also allows the user to stage the desired data when needed.
Although a back-up DLT units system had been installed at the experimental site and connected to the DAQ for 'local' data archival, not a single problem arose with the optical link connection. The local DLT units have never been used. The experience gained in Central Data Recording field will be extremely important for the future LHC experiments.

2.10.3 Evolution towards the Full System

During the data-taking period foreseen in 1997, the Central Data Recording system in its final configuration will be used to store 40 TeraBytes of data flowing at an average rate of about 19 MBytes/s.
The CS-2 fast internal network, its CPU power and its disk I/O capability are already adequate. However both the link throughput and the tape I/O speed need to be increased.
The FDDI link could be replaced by a HIPPI connection that has already been tested at CERN [41] , in order to provide more than 80 MBytes/s

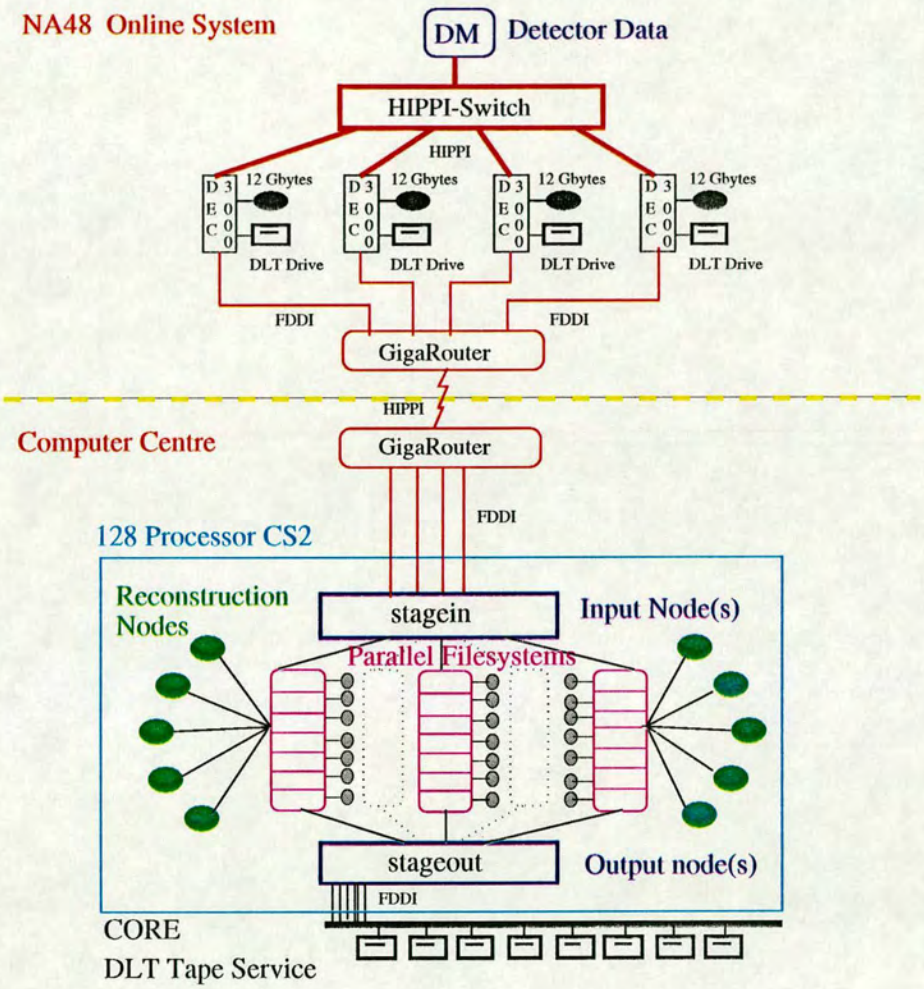

Figure 2.25: The NA48 online processing on the Meiko-CS2.

transfer rate. On the other hand, native HIPPI is a low-level, point-to-point uni-directional link, and currently there is no implementation of a high-level protocol (such as FTP) for Digital Unix. For this reason, the option of installing several FDDI links in favoured.

As far as data storage is concerned, if the 1997 requirements were to be met using DLT 2000 drives as in 1995, about 20 of them in parallel would be needed. Storage performances are expected to increase to provide a transfer rate of about 5-10 MBytes/s by 1997. For this reason, one of the design criteria of our system is the capability to integrate and profit from evolving computer technology. In particular, the software model must maintain transparent, reliable and efficient access to data at different storage levels. An user interface to access the data stored on permanent media and on disk in a reliable and transparent fashion in also essential, especially since the user has to be protected from the risk of misusing the system during data-taking.

Chapter 3

The 1995 data-taking and the Reconstruction Programs

This chapter describes the data-taking period which took place in 1995. The aim of such a period was the commissioning of the various components of the apparatus, the sub-detectors, the trigger system, the data acquisition. Moreover, the first physics data were collected. The algorithms used for event reconstruction are presented. A detailed description of the data analysis will be given in later chapters.

3.1 Experimental Apparatus

The 1995 data-taking was characterised by the absence of the electro-magnetic calorimeter. This allowed the detection of charged particles only.
The magnetic spectrometer consisted of three drift chambers, instead of four. Two chambers (1 and 2) were positioned immediately upstream from the magnet, and one downstream (chamber number 4). The information given by the first two chambers allow the reconstruction of a vertex position, while the momentum corresponding to a track can be determined using the impact point coordinates on the fourth chamber. The third chamber would have provided redundant information, allowing spurious tracks found from a given track section upstream of the magnet and an unassociated hit (for example, from backsplash from the hodoscope) to be rejected.
The mass resolution obtained with three chambers was about 2.5 MeV/c^2.
The K_S decays veto detector (AKS, see section 2.2), the charged hodoscope and the anti-counter rings were all in place as foreseen. The hadronic calorime-

ter and the muon veto detector were readout using a temporary system, based on commercial modules (CAMAC FERA).
Data sets were collected at several beam intensity values and with different beam configurations.

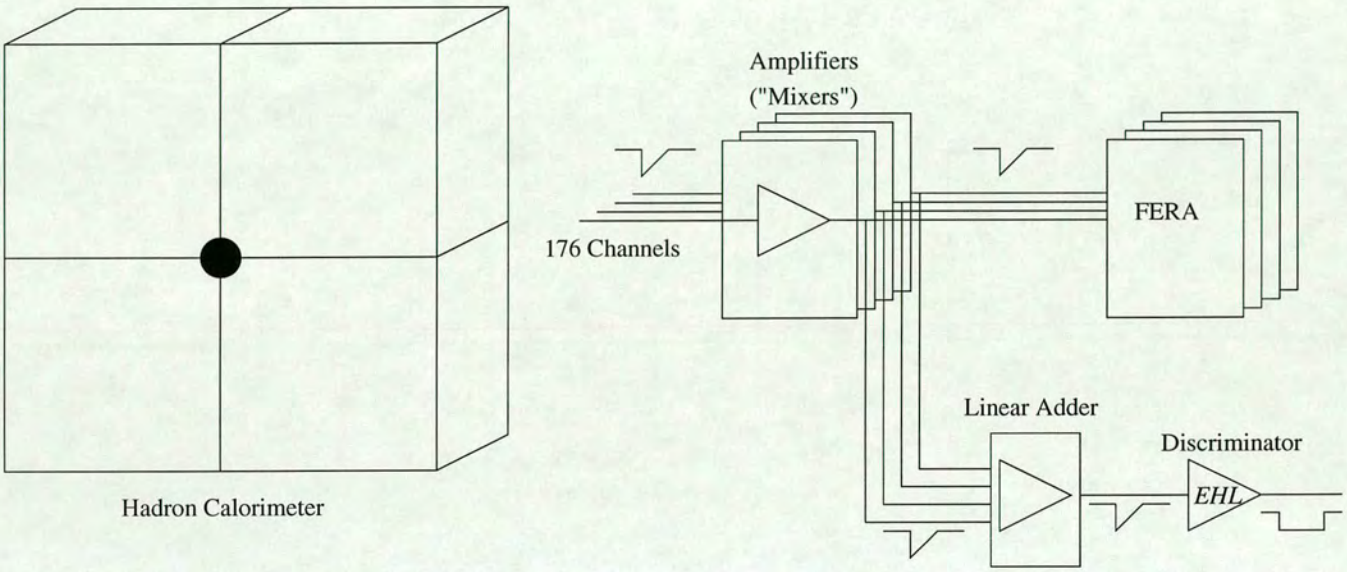

Figure 3.1: Scheme of the hadronic calorimeter readout in 1995.

3.2 Data Acquisition System

In four separate subsystems, detector signals were recorded, from

the charged hodoscope and AKS;

the tagger;

the drift chambers;

the hadron calorimeter and muon veto counters.

For each triggered event, the blocks of corresponding digitised signals from each subsystem were sent to different input buffers of the Data Merger via

optical fibres. From the Data Merger buffers, the different parts of an event were collected by the FIFO Output Formatter (FOF) and sent to one of the Front End Workstations. Triggers were dispatched by a prototype Trigger Supervisor. The entire flow was managed by the **Control Program** (CP). The CP supervises the state of the whole system and controls the start and end of a run. Its instructions are sent to the relevant subsystems via a dedicated Ethernet link, and received by a local control program called *harness*, running on a **Single Board Computer** (SBC).

3.3 TRIGGER

The information used to build a trigger signal came from the charged hodoscope, the hadronic calorimeter and the muon veto counters. Table 3.1 illustrates the logic for the so-called $\mu\mu\gamma$, $\pi\pi$ and *minimum bias* (*mb*) trigger signals. The hodoscope essentially provided information on the multiplicity

Charged Hodoscope Signals	
Q_x	$(QV_1 + QH_1) \cdot (QV_3 + QH_3) + (QV_2 + QH_2) \cdot (QV_4 + QH_4)$
Q_2	at least two sub-quadrants in coincidence
Muon Veto Signals	
μ	coincidence of OR of the first two planes
2μ	two counters in each of the first two planes
Hadronic Calorimeter Signals	
EHL	total energy $\geq$ 8GeV
EHH	total energy $\geq$ 35GeV

Table 3.1: How the various triggers are built

and position of charged tracks. A two-body decay has to satisfy the condition of coplanarity of the two tracks and the beam line. A signal called Q_x, that should guarantee this condition, is requested for a $\pi\pi$ trigger (see table 3.2). For other trigger types, the condition of just having two charged tracks onto any two subquadrants of the hodoscope is sufficient: this is the so-called Q_2

signal. In both cases (Q_x and Q_2) an inefficiency lower than 0.5% is expected from the inactive regions between two scintillators or two quadrants [42].
The semi-leptonic decays $K_{\mu 3}$ are rejected by means of the "$\mu 2$ signal", based on a coincidence of hits from the first two planes of the muon veto detector.
The hadronic calorimeter provides information based on the energy loss of the decay products. The signal given by a two charged pion event is higher than the one provided by a semi-leptonic decay. To get $\pi\pi$ events the *High Energy Threshold* (EHH) condition is imposed, whereas for minimum bias events the *Low Energy Threshold* (EHL) is requested. The *random* trigger

Trigger Signals	
$\pi\pi$	$Q_x \cdot$ EHH $\cdot\overline{\mu}$
minimum bias	$Q_2 \cdot$ EHL
$\mu\mu\gamma$	$2\mu \cdot$ EHL $\cdot Q_2$

Table 3.2: The trigger signals recorded during 1995 data-taking period

signal is generated by a beam intensity monitor, with a frequency that depends on the SPS accelerator period.

Each trigger signal was recorded after downscaling, by the PMB Pattern Unit system. Downscaling was necessary to reduce the trigger rate. The downscaling factor was chosen independently for each trigger type.

3.4 The Collected Data

Several tests on the detector components were carried out during the 1995 run.
The trigger and data acquisition systems were tested using signals given by a pulser, at a constant rate.
A 10 Hz laser signal sent to both the hodoscope and the tagger allowed the determination of the time resolution of the tagging system, with the advantage of being totally independent of the beam.
The correct alignment of the tagger scintillators was verified using a K_S beam at different intensities.

Different values of intensity of a combined K_L and K_S beam were chosen to study the behaviour of the drift chambers, the efficiency of the magnetic spectrometer and its ability to cope with the proposed nominal beam intensity.

After testing and commissioning the apparatus, physics data were recorded with a K_S beam and the $\pi\pi$ trigger, as well as with a K_L beam and a trigger given by the condition $\mu\mu\gamma + \pi\pi/D_1 + mb/D_2 + random/D_3$, where D_1, D_2 and D_3 indicate the downscaling factors.
The typical frequencies of the components of this trigger signal were:

$\mu\mu\gamma$: 2500 events/burst;

$\pi\pi$: 30000 events/burst;

minimum bias (*mb*) : 110000 events/burst;

random : 2500 events/burst.

In about 30 days of data-taking, $2.5 \cdot 10^6$ triggers were recorded onto 60 DLT 2000 cartridges (see paragraph 2.10.2), for a total of 520 GBytes and 93000 files.

3.5 Data Reduction

The data which have been used in the analysis described here belong to a set of *runs* recorded in September 1995. Most of the events were recorded using the $\mu\mu\gamma$ trigger.
A first selection of the recorded data was performed according to the trigger type. The procedure consisted in decoding the trigger bits in the raw data, and in rewriting only the events of interest onto different files. A sample of minimum bias, $\pi\pi$ and *random* events was thus selected. It contained:

975 119 $\pi\pi$ triggers;

1 505 042 *mb* triggers

which were subsequently used in the analysis.

3.6 Event Reconstruction

The information which need to be reconstructed is essentially the signals provided by the magnetic spectrometer and by the hadronic calorimeter.

3.6.1 Magnetic Spectrometer

The aim of this algorithm is to compute direction and momentum corresponding to each track.
As described in section 2.5, each drift chamber has four views (X, Y, U and V). Each view consists of two planes of wires. The first step performed by the program is the reconstruction of *clusters* of adjacent wires (in the two planes) which have been hit in each view.

The information coming from the same view of chambers 1 and 2 (upstream from the magnet) are used to define *segments* of tracks. The four segments corresponding to the four views are then combined to build a track.

The hits in chamber 4, downstream from the magnet, are combined together to form *space points*, which are then associated to the *segments* upstream. Complete tracks are thus found through the full spectrometer. The combination between a segment and a space point in chamber 4 is performed taking the magnetic field intensity and direction into account.

The momentum corresponding to each track in then computed and stored in a ZEBRA bank, together with the slope of the track, its coordinates x and y at a given z, and the electric charge of the particle.

The coordinates of a vertex and the distance of closest approach are then computed for each pair of tracks in the spectrometer, and stored as well.

3.6.2 Hadronic Calorimeter

After being reconstructed in the magnetic spectrometer, tracks are extrapolated onto the hadronic calorimeter to determine their impact points. A squared region (the so-called *shower box*) of n horizontal and n vertical strips

is considered around each impact point; the strip to which the track is extrapolated is the central strip of the shower box. Depending on the shower box size, additional strips on both sides of the central strip are included in the box. The default value for 1995 data was $n = 3$.

The total energy released by each track is given by the sum of the energies deposited in the strips belonging to the corresponding shower box. The energies in the front and back modules of the calorimeter are added independently.

The position of the shower is determined from the measurement in the front module. It is defined as the energy-weighted average of the position of all the strips of the shower box in one projection:

$$x_j = \frac{\sum_{i=1}^{n} E_{i,j} \cdot x_{i,j}}{\sum_{i=1}^{n} E_{i,j}} \tag{3.1}$$

where $j = 1, 2$ indicates the horizontal or vertical strips, and $i = 1, \cdots, n$ counts the strips in an $n \times n$ shower box.

The shower width in the horizontal and vertical projections (x and y) is defined as the RMS width of the shower in strip units:

$$W_{x,y} = \sqrt{\frac{\sum_{i=1}^{n} E_i x_i^2}{\sum_{i=1}^{n} E_i} - \left(\frac{\sum_{i=1}^{n} E_i x_i}{\sum_{i=1}^{n} E_i} \right)^2} \tag{3.2}$$

Chapter 4

The Simulation Programs

In order to extract information reliably about physical processes from experimental data and to perform precise measurements with small systematic errors, the simulations of the physics phenomena and of the detector behaviour are valuable, and often essential. A deep knowledge of the experimental apparatus and especially of the possible sources and relevance of systematic errors is necessary.
The simulation of an experiment can be divided into two phases: the event generation and the simulation of the various components of the apparatus. A generated event is identified by the physical process, and the kinematical quantities of all the involved particles. The response of the detector to the passage of particles is simulated as well. It is advisable that the format of the real detector signals and of the simulated ones be the same.
The Monte Carlo simulation of an experiment is used to design the apparatus and optimise its characteristics, as well as to develop and to test reconstruction strategies and to establish selection criteria. A careful simulation is also necessary to compute corrections for the detector acceptance, reconstruction efficiency and background contamination of the signal.

In this chapter the NA48 simulation programs are described. The experiment uses two different and complementary Monte Carlo algorithms. The first consists of a full and detailed simulation, called **NASIM**, which is very time-consuming. For this reason, a second, dedicated and fast detector simulation code, called **NMC** [45], has been developed by the collaboration. It does not perform a full event-by-event simulation of the shower depositions

in the liquid krypton calorimeter, making use instead of a so-called *shower library* generated by GEANT [44]. Thanks to the use of this particular technique, NMC is faster than NASIM by about two orders of magnitude. The fast NMC simulation package allows the generation of high statistics which is necessary to compute the corrections to the double ratio $\mathrm{Re}(\varepsilon'/\varepsilon)$, whereas the detailed simulation performed by NASIM is used for specific studies only.

4.1 The ESPRIT project GP-MIMD2

CERN participated as leading partner in a European ESPRIT project, called General Purpose Multiple Instructions Multiple Data - 2 (GP-MIMD2) [46]. The aim of this project was to demonstrate the use of an European MIMD computer (the Meiko CS-2, see section 2.10.1), and to investigate the benefits and the future prospects of parallel processing in High Energy Physics. I have been involved in GP-MIMD2 as a part of my work on the NA48 Monte Carlo simulation. In particular, I have been working on various aspects of the NMC program.

The present description will focus mainly on NMC, which I used to compute the acceptance corrections for my analysis. A brief description of NASIM is given for completeness.

4.2 NASIM

The simulation program NASIM is based on GEANT, a standard, general system of detector description and simulation tools developed at CERN. The generated particles are grouped according to their interactions with matter:

photons;

positrons and electrons;

muons;

neutral hadrons;

charged hadrons;

geantinos.

The *geantino* is a stable, non-interacting particle, with no electric charge and massless. It can be used, for example, in neutrino studies.
Particle decays and electro-magnetic processes are simulated, as well as multiple scattering, Bremsstrahlung, the photo-electric effect, Compton scattering, pair production, Rayleigh effect, photo-fission and hadronic interactions. Each particle inside the detector volume is tracked through the different media until its kinetic energy goes below a pre-defined limit. It is easy to see that the required computational time can reach remarkably high values - in NA48 case, the simulation of an average electro-magnetic shower in the calorimeter takes about 10 s on a HP735.

4.3 NMC

The program NMC (see fig. 4.1) follows a different philosophy, since the experimental apparatus is not fully simulated, but only described geometrically. An event is generated by producing, according to user specific parameters, a neutral kaon which decays into other particles that may in turn be unstable. For each of the particles thus created a number of quantities, such as their type, momentum and energy, generation vertex, decay vertex, charge and lifetime, are computed and recorded.
Each particle is then tracked from production to decay vertex (if any) by computing its space and time coordinates at a number of fixed planes in space perpendicular to the beam direction, one for each subdetector and for each relevant location (e.g. the magnet). Of particular importance, especially for fast decisions, is the information whether a given detector has been hit or not.
The response of each subdetector is then simulated according to parameterisations derived from detailed studies of calibration data or from NASIM calculations. This is a crucial point of such an approach, which is reliable only if the detector response can be adequately parameterised without following in detail the interactions of each particle within the detector.
All signals arising from events in a given time window around the one considered (so-called *accidentals*), corresponding to the detector sensitive time, are then collected and stored for later usage (for example in the simulation

of the trigger).

All the information relative to each single event are stored in memory blocks (*banks*) handled by the data structures management facility ZEBRA [47]. The structure of the program is illustrated in fig. 4.1.

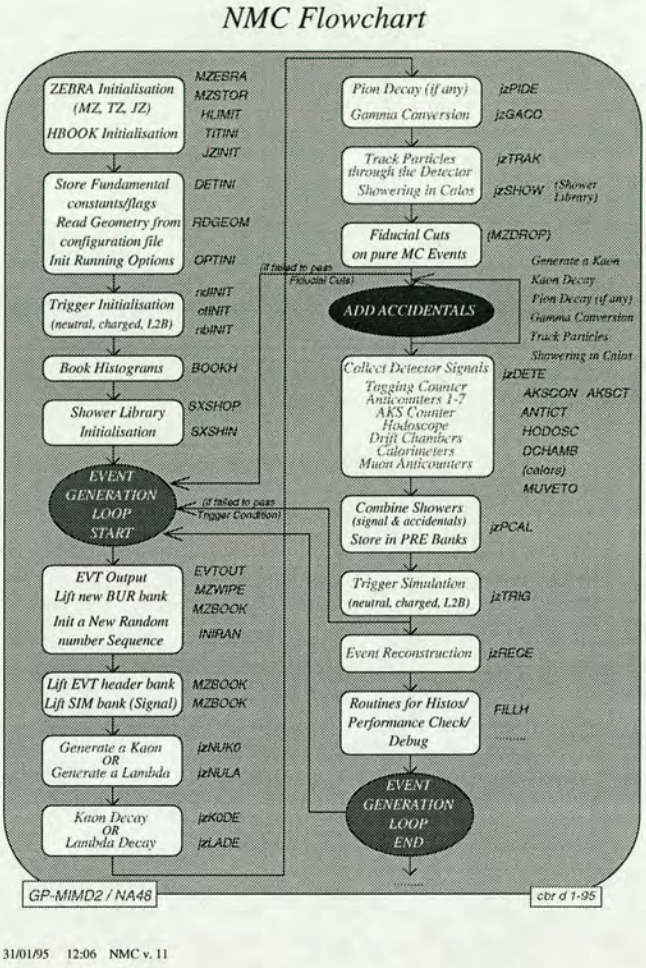

Figure 4.1: Flow-chart of the NMC Monte Carlo program.

4.3.1 The Shower Library

Instead of performing a full event-by-event simulation of shower depositions in the electro-magnetic calorimeter, NMC relies on a database called *shower library*, which is generated separately over a span of several days using NASIM. The database is read-only from the point of view of NMC. The showers are generated in the energy range of 2-100 GeV for photons and

electrons and between 2-200 GeV for pions, divided into 20 energy bins. Each entry in it is identified by the particle type (photon, electron or pion), the energy bin to which it belongs and the coordinates of its impact point on the calorimeter surface, and contains the energy deposited by the particle in the cell of a predefined area centred on its impact point. It can be re-used several times in the course of a large simulation, as long as this introduces a negligible bias in the result. It is worth noticing that for each set of requirements (particle type, energy and impact point) several showers have been generated, from which one is chosen by means of a random number. The size of the entire shower library is about 1 GByte, with 500K entries.
Eventually the shower library will be derived from real data.

4.3.2 Handling of Random Numbers

A number of requirements have to be met when handling random numbers in a Monte Carlo application like NMC. In particular, it must be possible to reproduce a given sequence of events regardless of some conditions which can be modified by the user; that is, the kinematics of each event and the detector signals must not change. For example, accidental events can be added without modifying the signal events that follow. Also, it must be kept in mind that a large number of independent random numbers may be used in the generation of a single event, and that large samples of events have to be generated without correlation.
The random generator RANLUX [48] was chosen after having investigated several possibilities. This routine generates pseudo-random numbers uniformly distributed in the interval (0,1). Each call produces an array of single-precision real numbers, and the user can choose a so-called "luxury level" which guarantees the required quality of the generated random numbers. The period of the generated pseudo-random number is greater than 10^{165} and they can be extracted from any of $9 \cdot 10^8$ independent sequences. The latter feature in particular was exploited to initialise a different sequence for each signal event, corresponding to the event number. Such a sequence provides all the necessary random numbers for that event and for its accidentals, if any.
It is worth noticing that the number of independent sequences gives a statis-

tical precision of about $3 \cdot 10^{-5}$, which is smaller by one order of magnitude than the statistical error on the data.

4.4 When Plenty of Simulation is Needed

For experimental reasons, a fast feedback from the Monte Carlo is desirable. A typical target is to generate the statistics for a first evaluation of acceptances and tail effects (about 10^7 events) overnight. In order to achieve this result and to improve the performance of the simulation program, the use of high performance computing techniques, such as parallel computing, has been considered.

Parallelism can be realized simply by running the code concurrently on several machines. The throughput is then trivially multiplied by the number of machines executing in parallel. This approach (call "event farming") is quite popular, being extremely cost effective when each event takes a large amount of CPU time compared to the input/output to disk and only aggregate throughput is important. The elapsed time to process a single event remains obviously unchanged; only the aggregate throughput is increased proportionately.

There are several limitations to this approach. Firstly, the organisation of a workstation farm becomes increasingly unwieldy as the number of workstations in the cluster increases. Beyond some limit, it is then necessary to consider partitioning or some other management technique to increase the robustness and the manageability of the system.
The networking between the workstations becomes also a limitation. For large clusters, there are questions of concurrency in database access which need to be carefully addressed.
There are also problems associated with storage subsystems which are not easily shared, and issues concerning the access to large disk farms for data.
Finally, if the application requires very large memory, then either the workstations are expensive because of the memory size, or there is too much disk activity as the memory is paged, which also impacts upon performance.

4.5 Parallelising the NA48 Simulation Program NMC

When the idea of parallelising the NMC simulation program was taken into account, a number of requirements had to be considered.
Every month or two, there is a new release of the software that includes bug-fixes and physics enhancements contributed by several physicists, typically experts in a particular sub-detector who devote only a small fraction of their time to software development and are not necessarily familiar with parallel processing.

4.5.1 Task Farming

The nature of the problem and the NA48 software community strongly suggested a simple, flexible and user-transparent approach to the parallelisation, in which the parallel and the (sequential) physics code are clearly separated. This simplifies the maintenance of the parallel versions and hides "obscure" message-passing calls from the occasional developer and from the end-user. In the *task farming* implementation the same program runs on different processing elements, called *event workers*, generating different events at the same time. A *source* processor initialises the working environment of the message passing interface as well as of the main code itself. It then splits the total amount of events to generate into "work packets" of pre-defined size, which are sent to the event workers upon reception of a work request message. Each of the worker processors generates events running NMC code itself. The results are then passed on to and collected by a so-called *sink* processor. The task farming structure is illustrated in fig. 4.2.

Thanks to the random numbers handling described above, the serial and the parallel versions of NMC generate exactly the same events. This is of fundamental importance when cross-checking the two codes, and certainly increases the user's confidence in the parallel program.

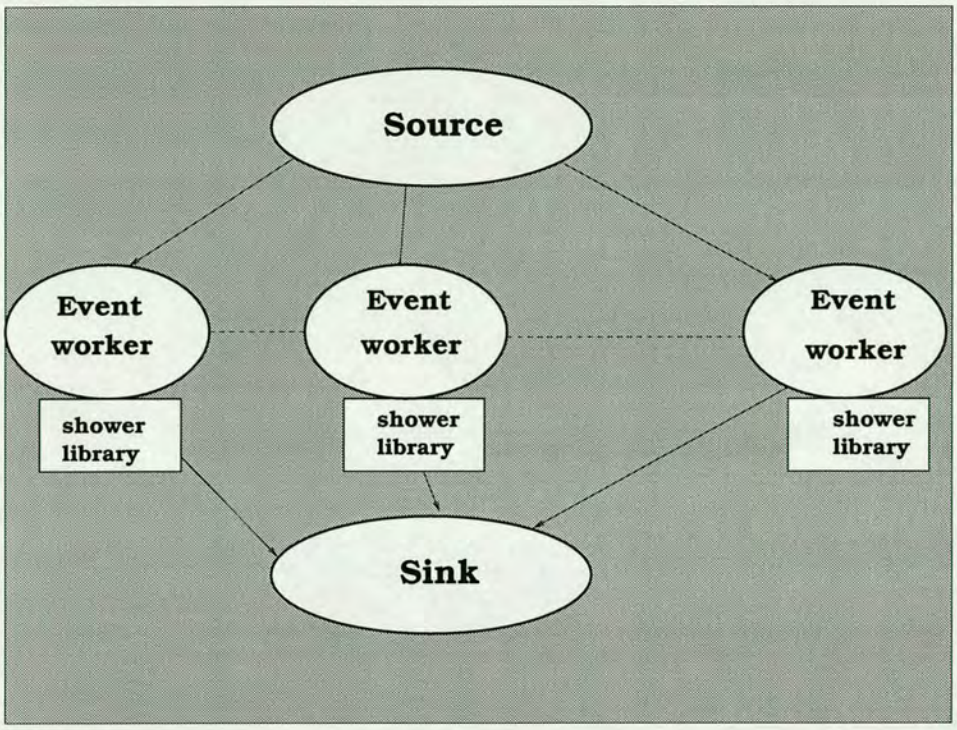

Figure 4.2: Parallel NMC, task farm structure.

4.5.2 Message-Passing Languages

Different message-passing interfaces, which make the communication between processors possible, have been tested to connect the different tasks of the parallel NMC version.
The first choice was CHIMP (Common High-level Interface to Message Passing) [49, 50, 51] developed at the Edinburgh Parallel Computing Centre. Groups of processes are set up during initialisation and stay unmodified during the simulation runs (static layout); communication between tasks belonging to different groups (e.g. between source and event workers) is carried out via standard blocking send and receive calls.

Other possibilities were also taken into account, for example implementing and testing a PARMACS [52, 53] version on NMC at the end of 1993, but this message passing language did not prove to be satisfactory.

After the standardisation of MPI (Message Passing Interface) [54] it was decided to migrate to it as soon as a native version was made available on the

Meiko CS-2. MPI is a portable library specification based on message passing (like CHIMP), proposed as a standard by a committee of vendors, implementors and users, and designed for high performance on both massively parallel machines and on workstation clusters.

4.5.3 Performance

With an aggregated network traffic of less than 5 MBytes/s, for a 50 processors run, the network requirements of NMC are rather modest. The I/O latency is more critical because in order to build a complete event up to eight showers have to be retrieved from the *shower library*. A low-latency "collision-less" network such as the Meiko CS-2's internal one is essential. Also it is important to parallelise the disk-read operations distributing the database over several disks. This is done in an elegant and transparent manner, exploiting the Meiko Parallel File System (PFS) capabilities. For a typical NMC run the I/O latency accounts for half of the processing time of an event. This latency can be reduced to negligible levels, running two NMC processes concurrently on each CS-2 processor, so that there is always one process running on CPU, while the other is waiting for its *shower library* record. The event throughput of NMC when running with one and two processes per processor has been measured (Fig. 4.3). The event throughput with two processes per processor is effectively doubled, confirming that, in the reference NMC configuration, I/O latency was accounting for half of the event simulation time and showing that this latency can be hidden almost completely. The linear scaling of the throughput with the number of processors confirms that the simple task farm approach does not introduce any significant overhead and that PFS bandwidth scales with the number of dedicated nodes.

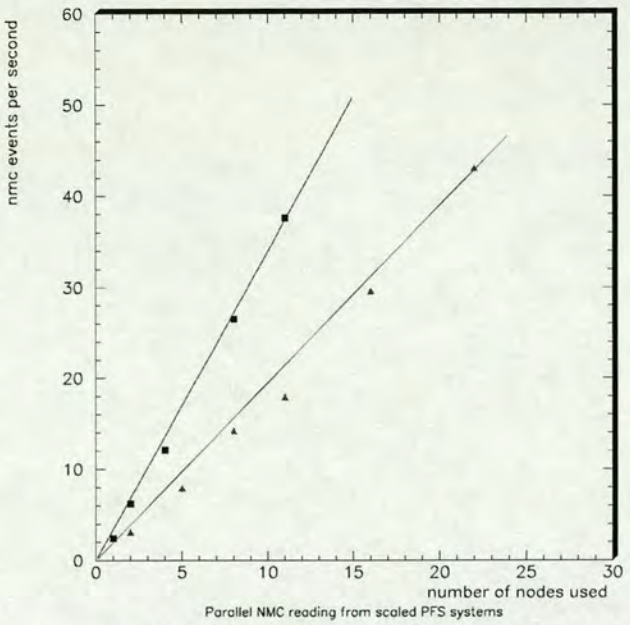

Figure 4.3: Parallel NMC event throughput reading from scaled PFS. Triangles refer to the case of running one NMC process per CS-2 processor, boxes to the case of two NMC processes per CS-2 processor

4.6 Real-time reconstruction and the Calibration of the Liquid Krypton Calorimeter

Reading back from tape the 40 TeraBytes of raw-data produced every year by NA48 should take several weeks and, due to limited tape resources, can only be performed after the end of a data-taking period. In order to give access to data during data-taking it is necessary to perform a systematic first-pass reconstruction while data files sit on the CDR disk buffer. To achieve the required performance, the reconstruction requires in quasi real-time the calibration constants of the Liquid Krypton Calorimeter response, with a few permil accuracy. In order to test the system, the parallel version of NMC has been run on 32 CS-2 processors, simulating 300 good calibration events per second, as produced by the experiment. The event simulation workers generated the events and passed the calorimeter data to 16 *calibration workers*, each one collecting the energies deposited in a 32×32 channels sector of the calorimeter. Each calibration worker performed independently the calibration of its calorimeter sector (1024 channels) using a standard technique called *Energy Resolution Minimisation* or *E/p method.* [55, and references

therein]. In a 5 hour run, 50 million kaon decays and 2.8 millions useful calibration events were generated achieving the required inter-calibration accuracy.
In particular, the response of each the 13000 channels of the Liquid Krypton calorimeter has to be calibrated with a few permilles accuracy. To monitor and correct for instabilities in the response, the calibration process should be repeated daily.

The calorimeter is calibrated using electrons produced in the $K \to \pi e \nu$ decay process. The electro-magnetic showers deposit their energy in a few hundred calorimeter channels. The energy of the primary electron is measured adding up the energy released in a *shower box* of typically 100 channels surrounding the impact point.
The electron energy measurements provided by the calorimeter is compared with the electron momentum measured by the spectrometer. As the electron momentum is measured with an error of the order of 1% and the electron energy is distributed over several calorimeter channels, about 100 events with an electron hit in any given cell are need to calibrate it at 0.3% level. As the distribution of electron hits over the calorimeter face is not uniform, $3 \cdot 10^6 K_{e3}$ events to perform a calibration are needed.

4.6.1 Feasibility Test of a Parallel Calibration Scheme

A pending problem is the well-known *ringing* effect of the solutions, which appears at the edges of each 32×32 array (fig. 4.4). Oscillations extend as far as one full shower box width (7 channels in this case). The basic algorithms for on-line calibration will be tested with real data coming from the calorimeter in the 1997 summer.

Several other basic studies can be developed using the simulation-calibration described above:

- a more refined data structure to store the coefficients of the calorimeter in a realistic way has to be implemented;
- the sub-division in sectors has to be improved in order to minimise the ringing effects at sector edges. One solution is to define partially *over-*

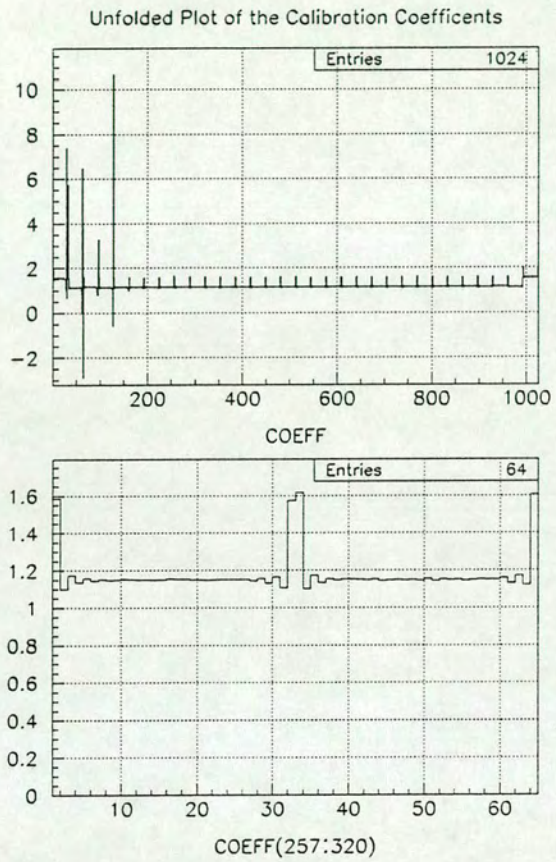

Figure 4.4: Top: the unfolded plot of all calibration coefficients (1024) of a given sector. Bottom: a close-up showing two rows and the ringing at the outer edge of each row. The large spikes in the top plot correspond to cells close to the central hole, the smaller ones to the outer edges of a sector.

lapping sectors and to compute the calibration coefficients only for the non-overlapping channels. The information of the channels in common with another sector, is used to create a smooth "shadow" at the edge. In this way, the ringing at the edges is effectively suppressed. The parallelisation in presence of overlapping sectors can be implemented using a virtual shared-memory scheme: just before the final matrix inversions the relevant calibration workers exchange the data relative to all overlapping cells;

- direct inversion methods for a sparse rectangular matrix (13000×10^6 elements) should be investigated, although they seem too memory demanding;

- Iterative methods should be evaluated, as well as mixed methods such as QR updating decomposition [56].

CHAPTER 5

DATA ANALYSIS

This chapter describes the analysis procedure to select the events of interest and to compute the studied branching ratio. The event selection method and the background subtraction are explained.

5.1 THE RATIO $\frac{\Gamma(K_L \to \pi^+\pi^-)}{\Gamma(K_L \to \pi^\pm e^\mp \overset{(-)}{\nu})}$

The branching ratio of the channel $K_L \to \pi^+\pi^-$ is small compared to the more frequent three-body decays, as illustrated in table 1.1 [6].
The branching ratio of $K_L \to \pi^+\pi^-$ has been measured using the decay $K_L \to \pi^\pm e^\mp \overset{(-)}{\nu}$ as normalisation. The branching ratio of $K_L \to \pi^+\pi^-$ can then obtained as:

$$\begin{aligned} BR(K_L \to \pi^+\pi^-) &= \frac{\Gamma(K_L \to \pi^+\pi^-)}{\Gamma(K_L \to \pi^\pm e^\mp \overset{(-)}{\nu})} \cdot BR(K_L \to \pi^\pm e^\mp \overset{(-)}{\nu}) \\ &= R \cdot BR(K_L \to \pi^\pm e^\mp \overset{(-)}{\nu}) \end{aligned} \tag{5.1}$$

The ratio R of the two decay modes is evaluated by measuring the number of decays for each channel and the corresponding efficiencies. The following expression is used:

$$R = \frac{\Gamma(K_L \to \pi^+\pi^-)}{\Gamma(K_L \to \pi^\pm e^\mp \overset{(-)}{\nu})} = \frac{N_{K2\pi}}{N_{Ke3}} \cdot \frac{\epsilon_{Ke3}}{\epsilon_{K2\pi}} \tag{5.2}$$

where $N_{K2\pi}$ and N_{Ke3} indicate the number of events in the two channels, and $\epsilon_{K2\pi}$, ϵ_{Ke3} are the corresponding total efficiencies.
The event selection procedure is described in the following, whereas the computation of the efficiencies will be explained in the subsequent chapter.

5.2 Event Selection

5.2.1 General Cuts

The first step to select the events of interest is to discard events which are clearly anomalous and to avoid the regions where the trigger is most likely to be inefficient. This is the reason why some conditions are imposed on all the events, independently of the particular channel ($\pi^+\pi^-$ or $\pi^\pm e^\mp \overset{(-)}{\nu}$) one wants to select.

- Two tracks of opposite electric charge must be reconstructed for each event.
- In order to ensure a good vertex quality, the distance of closest approach is required to not exceed 1.5 cm (see fig. 5.1).

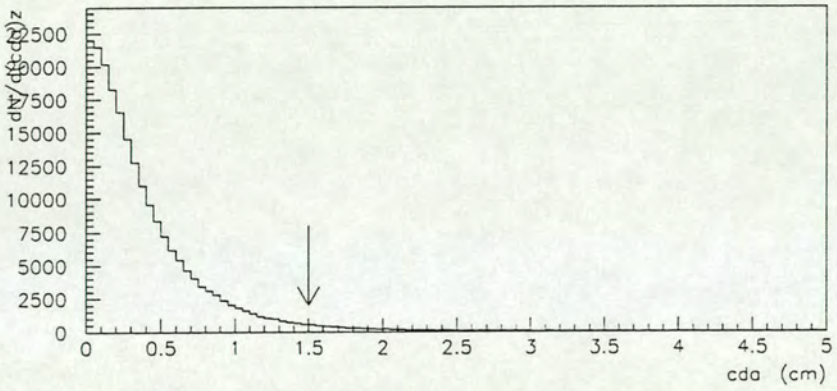

Figure 5.1: Closest distance of approach. The arrow indicates the applied cut (K_L data, 1995).

- The distribution of the reconstructed z coordinate of the vertex is shown in fig. 5.2, and used to define the *fiducial region*. The latter starts at a distance of 2 m from the last K_L collimator (6.8 m downstream of the K_S target) and is 58 m long.
- The distribution of track momentum is shown in fig. 5.3. The momentum of each single track must not be smaller than 10 GeV, and the magnitude of the vector sum of the two momenta must be in the range 20-200 GeV (see fig. 5.4).

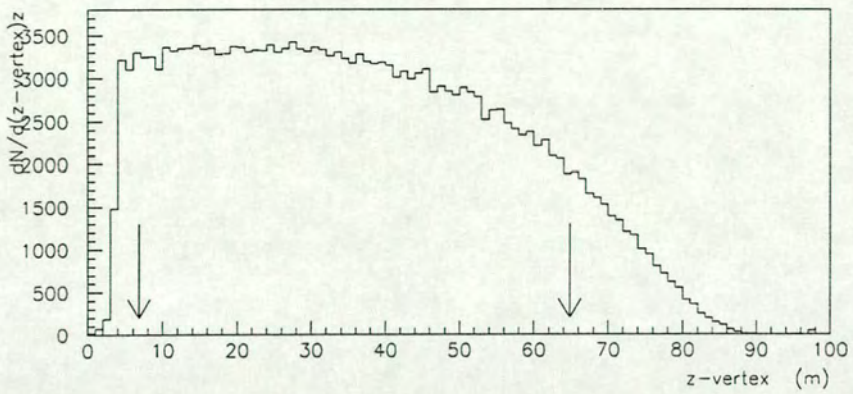

Figure 5.2: The longitudinal coordinate of the vertex. The cuts are shown by the two arrows (K_L data, 1995).

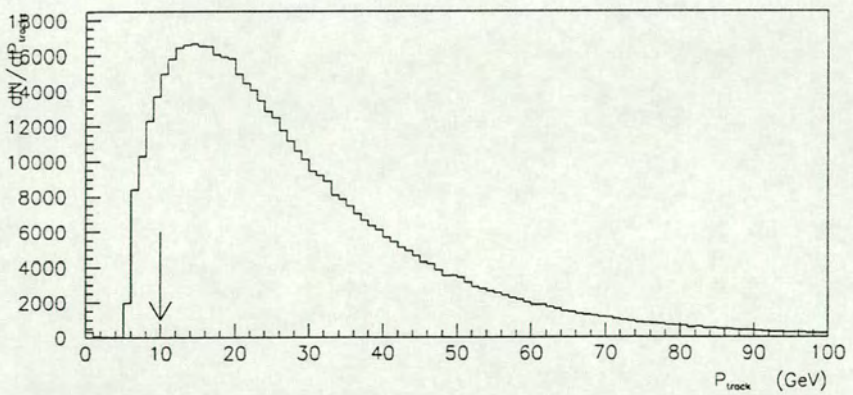

Figure 5.3: Single track momentum. The arrow shows the condition applied on the minimum value (K_L data, 1995).

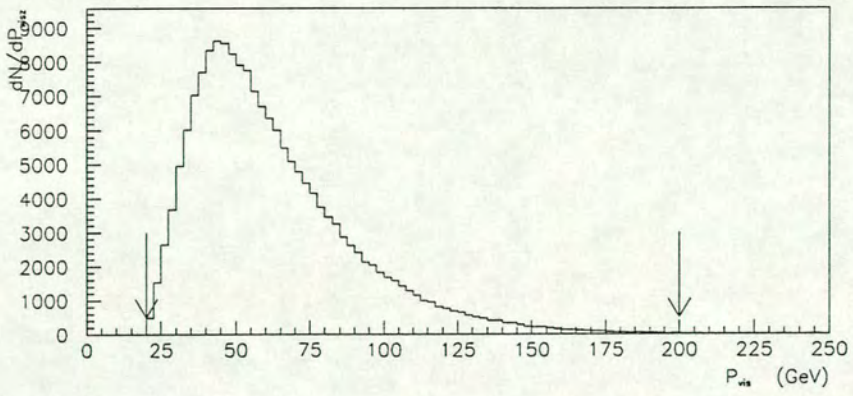

Figure 5.4: The total visible momentum. The arrows indicate the applied cuts (K_L data, 1995).

- The radial distance d_{rad} of the track impact point on the first chamber from the central hole is plotted in fig. 5.5. The region around the hole is discarded by requesting d_{rad} to be larger than 12.5 cm for each track.

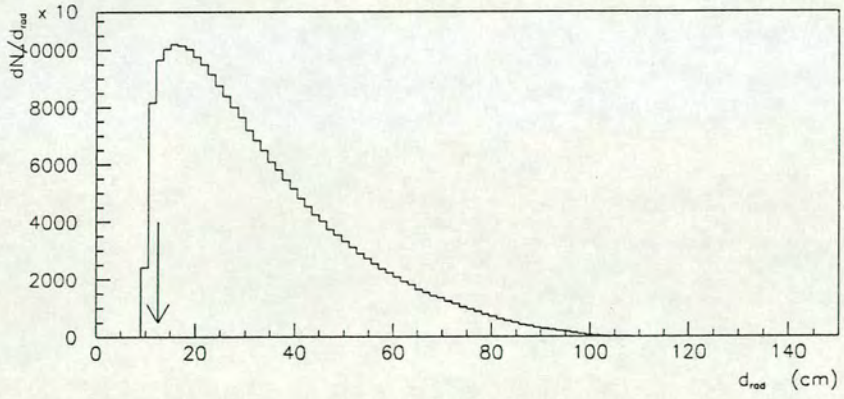

Figure 5.5: The radial distance of the track impact point from the centre of the first drift chamber. The applied cut is indicated by the arrow (K_L data, 1995).

The composition of the whole data sample after having applied the conditions described above is illustrated in table 5.1.

The analysis has been executed separately for the $\pi\pi$ and the minimum bias

number of $\pi\pi$ triggers	590382
number of minimum bias triggers	590693
other triggers	25522
total	1181075

Table 5.1: Composition of the data set after the "general cuts".

trigger data sets. One of the aims of the 1995 data analysis is indeed the study of the different trigger types, which can have different inefficiencies. Performing the same analysis on the two data sets allows to check the different triggers and to avoid any assumptions on the downscaling factors.

5.2.2 Selection of $K_L \to \pi^+\pi^-$ candidates

Due to its small branching ratio, the decay into two charged pions needs a careful selection. It is necessary to reject the dominating background without losing events of interest.

Trigger conditions. The $K_L \to \pi^+\pi^-$ have been selected in both the $\pi\pi$ and the minimum bias trigger data sets.

Cuts related to trigger conditions. In order to discard semi-leptonic decays containing muons, it has been requested that at least the majority of two planes out of three in the muon veto counter had not been hit. The efficiency of this cut in detecting muons has been estimated as $(99.8 \pm 0.1)\%$ [57].

The information given by the spectrometer has been used to compute the position of the tracks impact points on the charged hodoscope. A geometrical Q_x condition (i.e. two hits in opposite quadrants) is then imposed.

Kinematical cuts. Figure 5.6 shows the distribution of the kinematical variable $(p'_0)^2$, defined as

$$(p'_0)^2 = \frac{(m^2_{K^0} - m^2_{\pi^0} - m^2_{\pi\pi})^2 - 4(m^2_{\pi^0} m^2_{\pi\pi} + p_t^2 m^2_{K^0})}{4(p_t^2 + m^2_{\pi\pi})} \qquad (5.3)$$

where m_{K^0} indicates the kaon mass, m_{π^0} is the neutral pion mass, $m_{\pi\pi}$ is the effective mass of the two charged tracks (supposed to correspond to a $\pi^+\pi^-$

pair), and p_t is their transverse momentum.

The quantity $(p'_0)^2$ is the momentum of K_L in the reference frame in which the longitudinal momentum of the two charged tracks is zero. In a $K_L \to \pi^+\pi^-\pi^0$ decay, the magnitude of $(p'_0)^2$ is hence equal to the longitudinal momentum of the neutral pion, so it must be ≥ 0. For other decays, namely the semi-leptonic ones K_{e3} and $K_{\mu 3}$, the quantity $(p'_0)^2$ assumes mainly negative values. In order to discard $K_L \to \pi^+\pi^-\pi^0$ events, the condition $(p'_0)^2 \leq -0.015$ GeV^2 has been applied.

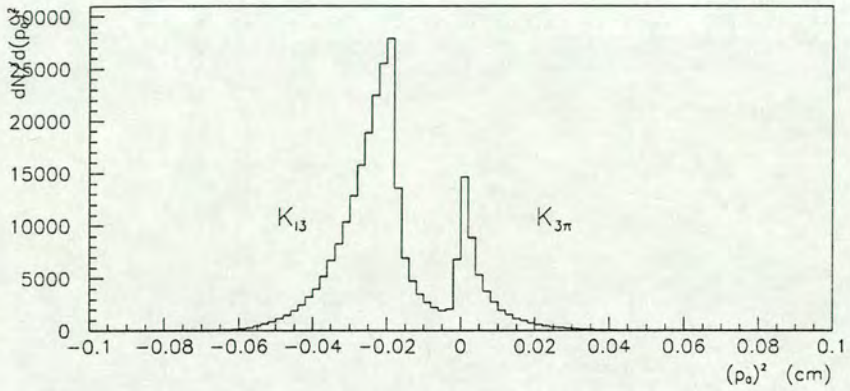

Figure 5.6: The variable $(p'_0)^2$ (K_L data, 1995).

The invariant mass distribution of the events selected by the $\pi\pi$ and minimum bias triggers is shown in fig. 5.7 (left). It has been obtained by assigning the pion mass to each charged track:

$$m = \sqrt{((E_1 + E_2)^2 - (|\vec{p_1} + \vec{p_2})^2|)} \tag{5.4}$$

where p_i is the momentum of each track and $E_i = \sqrt{(|\vec{p_i}|^2 + m_\pi^2)}$. The peak on the left, approximately centred around 350 MeV, corresponds to the $K_L \to \pi^+\pi^-\pi^0$ decay in which the neutral pion is not detected. Such a peak disappears after imposing the condition on the variable $(p'_0)^2$ described above, as shown in fig. 5.7 (right).

The small peak around the kaon mass (497.7 MeV) is given by the $K_L \to \pi^+\pi^-$ events, which must be separated from the dominant semi-leptonic decays. A loose cut on the mass is applied, imposing 0.483 GeV $< m_{\pi\pi} <$ 0.509 GeV. A Monte Carlo simulation shows a loss of only 0.03% of the $\pi^+\pi^-$ events.

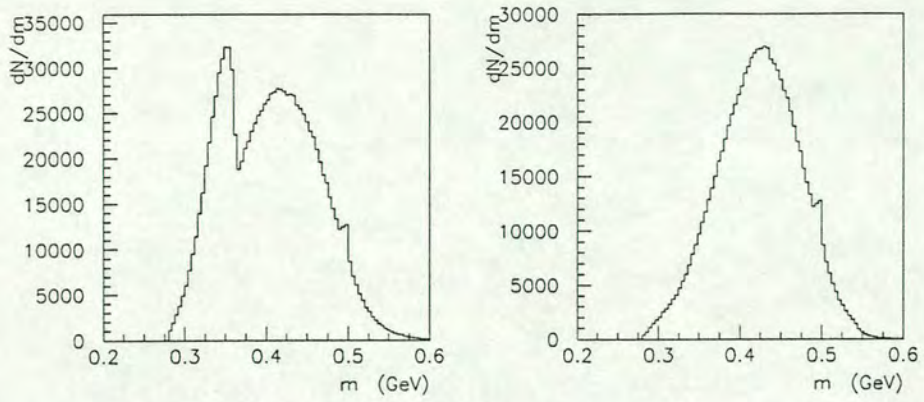

Figure 5.7: Reconstructed invariant mass before and after the condition on $(p'_0)^2$.

The distribution of the reconstructed invariant mass as a function of the transverse momentum squared (in logarithmic scale) is given in fig. 5.8. In the first picture, the $K_{3\pi}$ events are clearly visible, while after applying the above described conditions the events of interest and the prevailing background from K_{e3} are left. The mass cut is shown by the arrows. The maximum accepted value of the transverse momentum squared has been set at 125 MeV^2/c^2. This condition allows 99.6% of the events of interest to be kept.

The minimum value of kaon momentum has been set to 65 GeV, in order to avoid inefficiencies due to the hadronic calorimeter energy threshold required at trigger level (see section 6.3).

VERIFICATION OF THE $\pi^+\pi^-$ EVENTS SELECTION WITH PARTICLE IDENTIFICATION.

The information provided by the hadronic calorimeter, although not very accurate, can be used to distinguish pions from electrons. The relevant quantity is the ratio between the energy deposited by a track in the front module of the hadronic calorimeter (in a square *box* of 3×3 strips around the impact point) and the momentum of that track measured by the spectrometer. In fig. 5.9 the distribution of E^{front}_{HAC}/p_{vis} for electron and pion candidates is shown. The peak at low values is due to pions whose shower in the front module of the calorimeter could not be properly reconstructed.

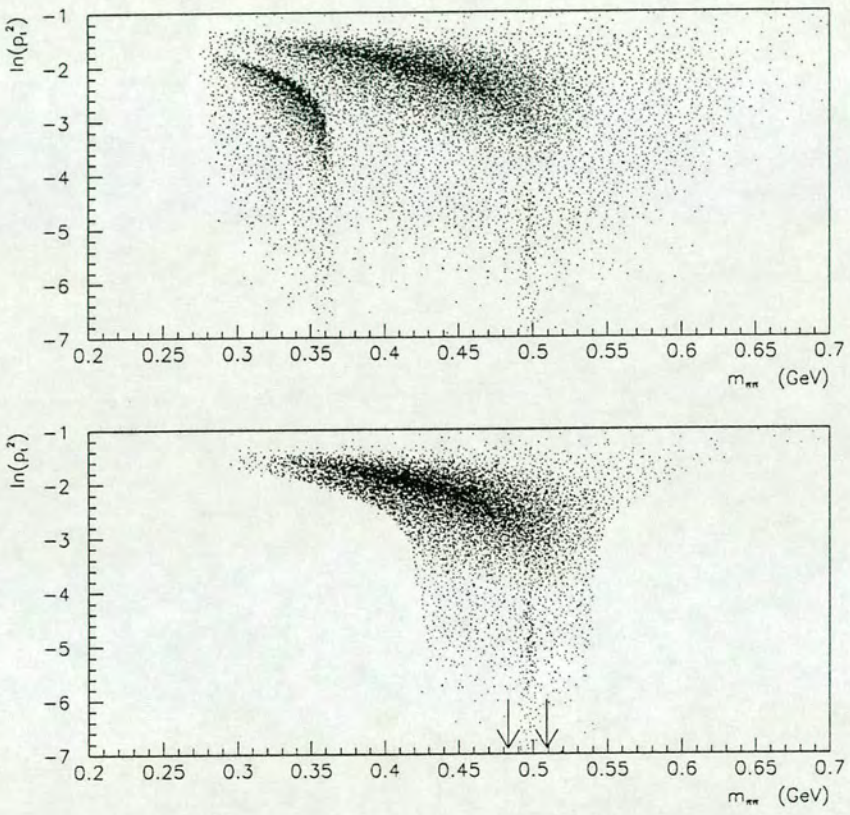

Figure 5.8: Distribution of transverse momentum (in logarithmic scale) versus reconstructed invariant mass, before (above) and after applying the $\pi^+\pi^-$ selection conditions.

The distribution of the variable E_{HAC}^{front}/p_{vis} has been used in order to verify

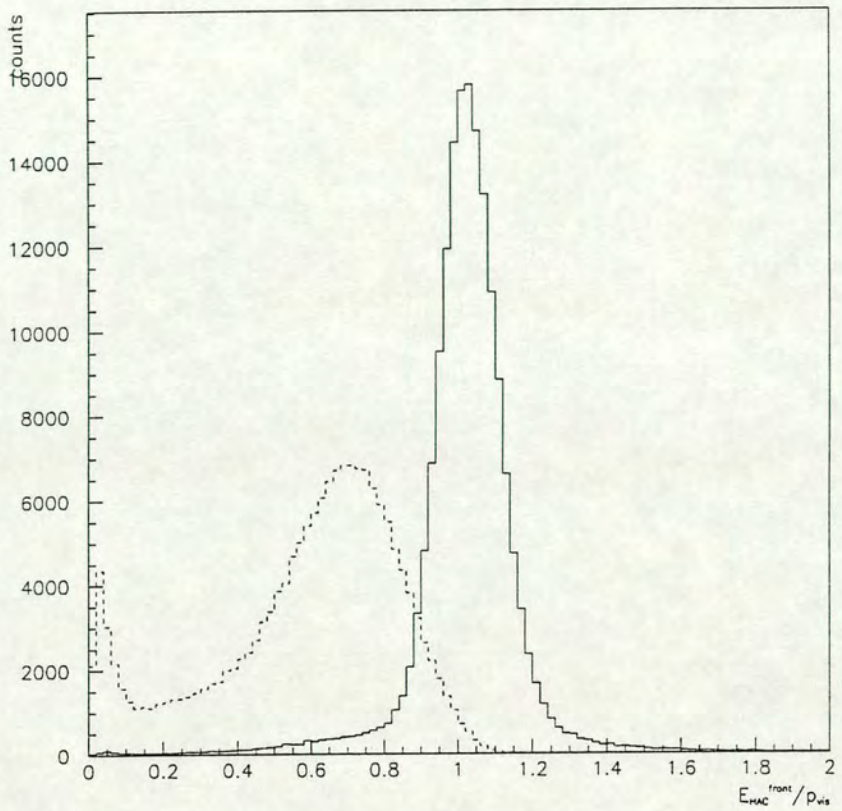

Figure 5.9: E_{HAC}^{front}/p_{vis} distribution for electron (solid line) and pion candidates.

the effectiveness of the selection criteria for $\pi^+\pi^-$ events. Fig. 5.10.a shows the E_{HAC}^{front}/p_{vis} distribution for all the data in the minimum bias sample: the peak due to muons is visible at low values, and disappears after imposing the cuts related to trigger conditions (b). The peak due to charged pions is reduced by the cut on $(p'_0)^2$, which aims to $K_{3\pi}$ rejection (c). The electron signal is reduced by a cut on the maximum value of the transverse momentum (d); it can be noticed, however, that a background given by K_{e3} events is still present.

The distribution of E_{HAC}^{front}/p_{vis} for K_S data is given in fig. 5.11 for comparison. The branching ratio of $K_S \to \pi^+\pi^-$ is $(68.61 \pm 0.28)\%$, while that of the neutral decay mode ($\pi^0\pi^0$), not detected by NA48 in 1995, is $(31.39 \pm 0.28)\%$.

The branching ratios of all the other channels are smaller by one order of magnitude or more.

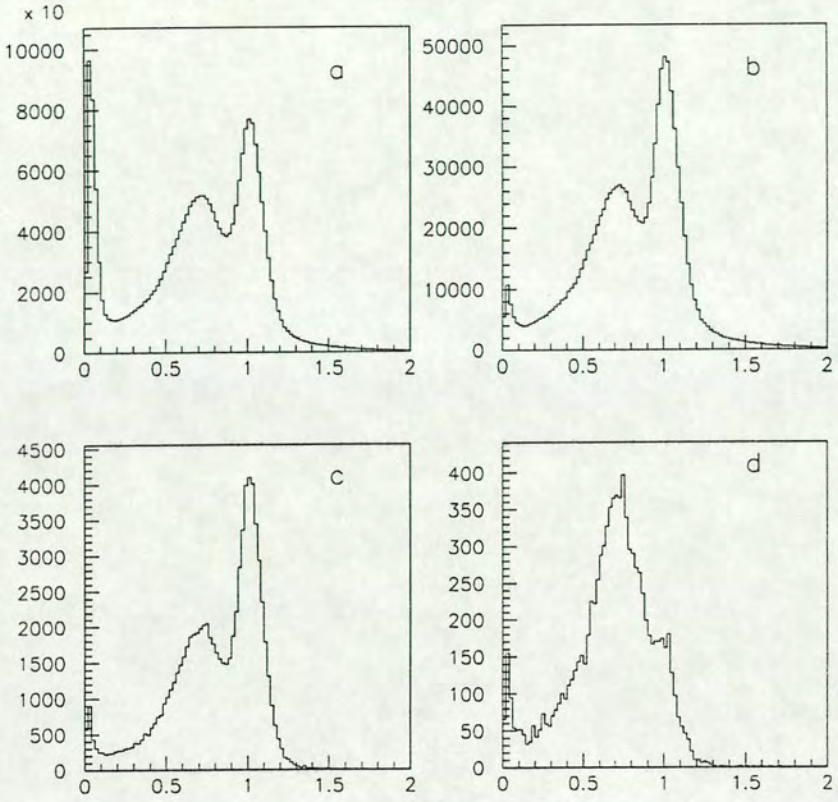

Figure 5.10: E_{HAC}^{front}/p_{vis} distribution before event selection (fig. a); after discarding events which contain muons (b); after $K_{3\pi}$ rejection (c); final distribution, before background subtraction (d).

Background subtraction

In order to determine the number of $K_L \to \pi^+\pi^-$ decays correctly, it is necessary to evaluate the amount of background events which survive the selection criteria.

The transverse momentum has been computed with respect to the line connecting the vertex to the K_L target. The distribution of such a variable is illustrated in fig. 5.12. The first picture shows the transverse momentum squared of all the data in the minimum bias sample. In the second one, the same quantity was plotted after imposing the trigger-related conditions; the

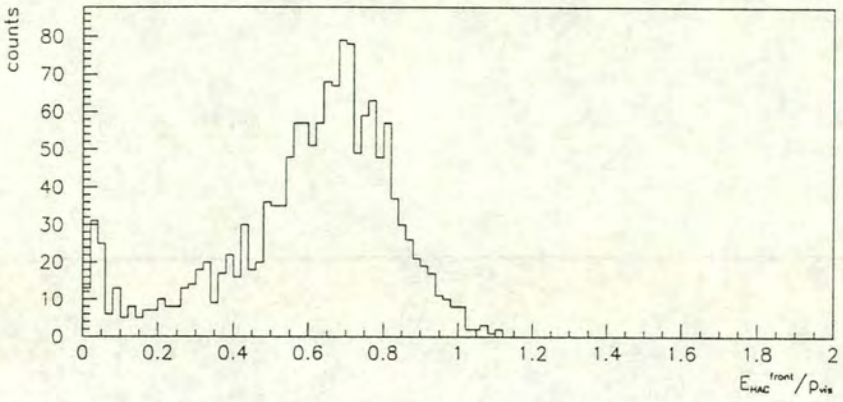

Figure 5.11: E_{HAC}^{front}/p_{vis} distribution for K_S data.

last shows the final distribution. The peak at low values corresponds to the two-body decays which have to be extracted from the main K_{e3} background. The transverse momentum squared is thus a good quantity to perform the subtraction of background.

The technique. The background distribution has been extrapolated under the $\pi^+\pi^-$ peak and subtracted from the whole distribution. The maximum allowed value for transverse momentum squared has been set to 125 MeV$^2/c^2$, as shown in fig. 5.12.c.

The distribution of the transverse momentum squared for those events whose invariant mass is outside the allowed mass window is given in fig. 5.13. A fourth-grade polynomial has proven a good and simple curve to fit such a distribution. The associated function has then been used to fit the transverse momentum squared distribution of the events selected so far. The number of the decays of interest has been obtained subtracting the area under the 4th degree curve from the whole distribution (see subsection 6.3.1).

5.2.3 Selection of $K_L \to \pi^\pm e^\mp \overset{(-)}{\nu}$ events

Trigger conditions and related cuts. The events of interest have been selected both in the $\pi\pi$ and minimum bias data sets. The requirement on the muon veto detector signals described above has been applied.

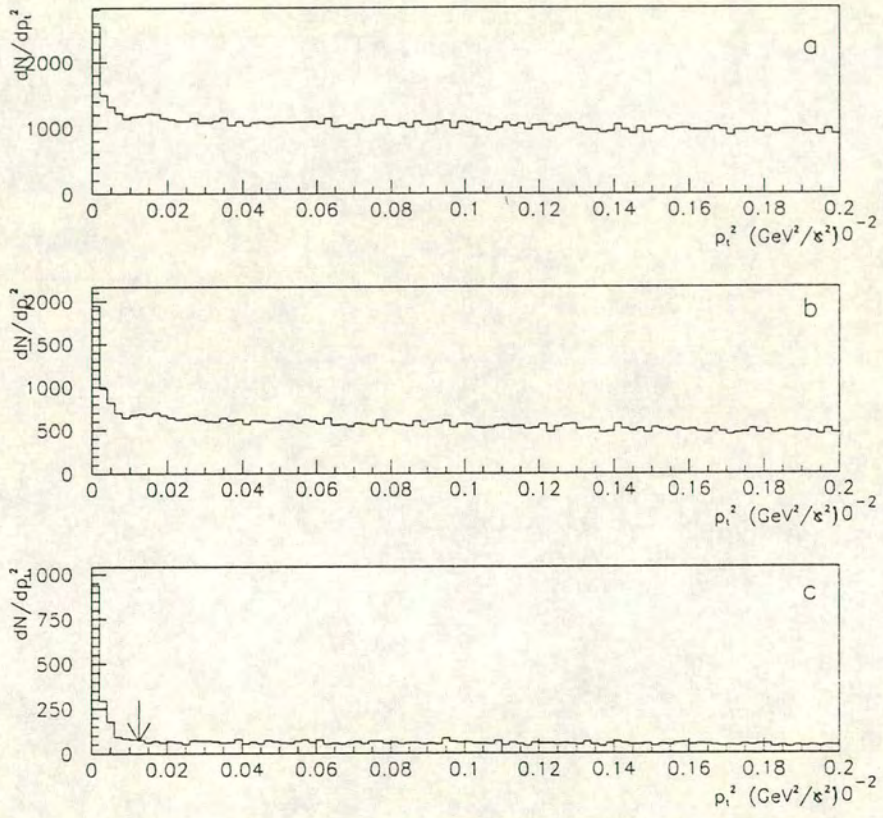

Figure 5.12: Distribution of transverse momentum squared for (a) all the events in the minimum bias sample; (b) for those events which survive the trigger-related conditions; (c) for the $\pi^+\pi^-$ candidates. The arrow shows the applied cut.

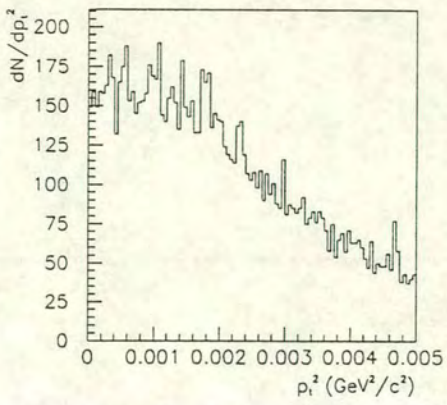

Figure 5.13: Transverse momentum squared of events with mass below 489 MeV or above 506 MeV.

Kinematical cuts. The $K_{3\pi}$ events, which give the largest background, have been eliminated by imposing $(p'_0)^2 \leq -0.004$ GeV^2. Such a cut removes 99.96% of the $K_{3\pi}$ events while keeping 97.9% of K_{e3}.

The condition on the value of transverse momentum squared

$p_t^2 \geq 1.25 \times 10^{-4}$ GeV$^2/c^2$ allowed to discard 99.6% of the CP-violating decays $K_L \to \pi^+\pi^-$. It keeps 98.8% of the events of interest.

In analogy with the $K_L \to \pi^+\pi^-$ selection, a minimum value of 65 GeV is requested on the visible momentum of the kaon.

5.2.4 The final samples

The final sample of candidates for $\pi^+\pi^-$ and K_{e3} events is shown in table 5.2. In the next chapter the computation of the efficiencies is discussed.

Decay mode	$\pi\pi$ trigger	minimum bias trigger
$K_L \to \pi^+\pi^-$	2118	901
(background events:	716	269)
$K_L \to \pi^\pm e^\mp \overset{(-)}{\nu}$	175535	86034

Table 5.2: Number of selected events in the two data sets, for each of the two decay modes of interest.

Chapter 6

Corrections

After counting the number of events of interest in the data samples, it is necessary to apply some corrections, in order to take into account all the factors which may affect the measurement, such as limited geometrical acceptance of the detector, efficiency of the trigger, of the reconstruction and of the conditions imposed at selection level.
The Monte Carlo program NMC (see chapter 4) was used. It was particularly suited for the purposes of this work, since a very accurate simulation of the calorimeter's response was not needed, and because it allows a fast feedback.

6.1 Geometrical Acceptance

Two-pion events. In order to estimate the number of $K_L \to \pi^+\pi^-$ events in which one or both decay products fall outside the detector, and thus cannot be observed, a Monte Carlo simulation of the events of interest was performed.
It was requested that the two charged pions passed through the three drift chambers, the charged hodoscope and the hadronic calorimeter. Moreover, events containing muons were discarded, as well as those in which a charged track hit a collimator or the muon veto detector. The acceptance has been computed in bins of visible momentum and longitudinal vertex position (see below, section 6.3.1). Its overall value is $(47.9 \pm 0.1)\%$. The quoted error is purely statistical and it has been evaluated as

$$\Delta(A) = \sqrt{\frac{A(1-A)}{N}} \tag{6.1}$$

where A is the computed acceptance and N is the total number of generated events.

Semi-leptonic decays. In case of $K_L \to \pi^{\pm} e^{\mp} \overset{(-)}{\nu}$ events, the same conditions as the ones described for the $\pi^+\pi^-$ events were imposed on the charged pion and the electron. The computed acceptance was found to be $(41.8 \pm 0.1)\%$. It is smaller than the acceptance for $\pi^+\pi^-$, since the semi-leptonic decays are 'unbalanced' due to the undetectable neutrino, and thus more likely to fall outside the detector geometry.

6.1.1 Check of geometrical acceptance

For the two-pion decay mode, the geometrical acceptance can be computed analytically, thus allowing an useful check of the Monte Carlo simulation. From the relation between angles in the laboratory and in the centre of mass frame:

$$\tan\theta_{LAB} = \frac{\sin\theta_{CM}}{\gamma(\cos\theta_{CM} \pm \beta/\beta_{CM})} \tag{6.2}$$

a weight can be computed for each event, as $1/(\cos\theta_{CM}$ accepted interval). More details of the calculation are given in appendix A. The comparison between the kaon momentum spectrum corrected with Monte Carlo-computed and analytical geometrical acceptance (illustrated by fig. 6.1) shows a satisfying agreement.

6.2 Efficiency of the Reconstruction Program

Those Monte Carlo events which had satisfied the acceptance criteria were given as input to the reconstruction program. It is necessary to determine which percentage of the decays of interest can be correctly reconstructed with two tracks and a vertex.

The efficiency of the reconstruction program has been estimated using Monte Carlo events, according to the definition

$$\epsilon_{rec} = \frac{N_{rec}}{N_{acc}} \tag{6.3}$$

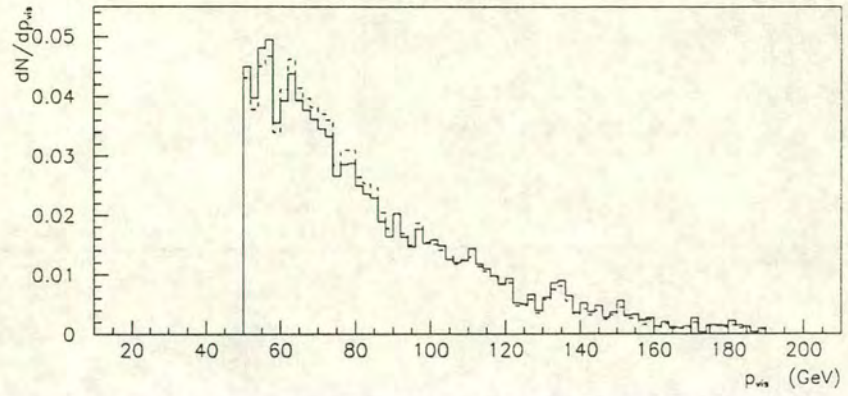

Figure 6.1: Comparison between the kaon momentum spectrum corrected with Monte Carlo-computed acceptance (solid line) and analytically computed acceptance.

where N_{acc} is the number of events which had passed the geometrical acceptance conditions (see previous section, 6.1), and N_{rec} indicates the number of events which have been reconstructed. The efficiency of the reconstruction is

- $(97.83 \pm 0.05)\%$ for $\pi^+\pi^-$ decays
- $(91.7 \pm 0.1)\%$ for K_{e3} events.

The reasons why some events could not be reconstructed have been studied in detail. A cut imposed on minimum track momentum and on its slope, together with a too small separation between two tracks, are the main causes of inefficiency. The algorithm has been designed to maximise the reconstruction efficiency for $\pi^+\pi^-$ events.

6.3 The Kaon Momentum Spectrum

The momentum p of a kaon is generated in the Monte Carlo program according to the spectrum

$$\frac{d^2N}{dpd\Omega} = \frac{\eta p^2}{4p_0} \cdot [1.3e^{-(8.5p/p_0+3.0p^2\theta^2)} + 4.35e^{-(13p/p_0+3.5p^2\theta^2)}] \qquad (6.4)$$

where η is the target efficiency, p_0 indicates the momentum of the incident proton beam (450 GeV/c), and θ is the production angle (whose average is

2.4 mrad for K_L and 4.2 mrad for K_S). This spectrum has been computed from precision measurements of particle production by 400 GeV protons on beryllium targets [58].

Experimentally, the kaon spectrum has been reconstructed using the $K_L \to \pi^+\pi^-$ events selected in the $\pi\pi$ trigger data set. The momentum of the decaying kaon is given by the vector sum of the momenta of the two charged pions.

It is necessary to apply some corrections in order to reconstruct the kaon momentum spectrum.

6.3.1 Corrections applied to momentum spectrum

Acceptance correction. The geometrical acceptance has been measured in bins of visible momentum and longitudinal coordinate of the kaon decay vertex. For each bin, the acceptance has been defined as

$$A(p_{vis}, z) = \frac{N_{acc}(p_{vis}, z)}{N_{gen}(p_{vis}, z)} \tag{6.5}$$

where $N_{gen}(p_{vis}, z)$ indicates the number of generated events in the bin (p_{vis}, z), and $N_{acc}(p_{vis}, z)$ is the number of accepted events in the same bin.

For each bin, a weight W_{acc} has been computed as

$$W_{acc}(p_{vis}, z) = \frac{1}{A(p_{vis}, z)} \tag{6.6}$$

and applied to all events in order to correct for geometrical acceptance (see fig. 6.2).

Correction due to kaon decay. It is necessary to compute the *production* spectrum of the K mesons, i.e. the spectrum at the K_L target. In order to do so, one has to take into account the probability that a kaon decay takes place in the fiducial region, which is defined by the minimum and maximum allowed values of the longitudinal vertex coordinate (z_{min} and z_{max} respectively):

$$P(z_{min} - z_{max}) = P(after\ z_{min}) \cdot P(before\ z_{max}). \tag{6.7}$$

The probability of a kaon surviving until the beginning of the fiducial region (see fig. 6.3) is given by

$$P(after\ z_{min}) = e^{-L/(\beta\gamma c\tau_{K_L})} \tag{6.8}$$

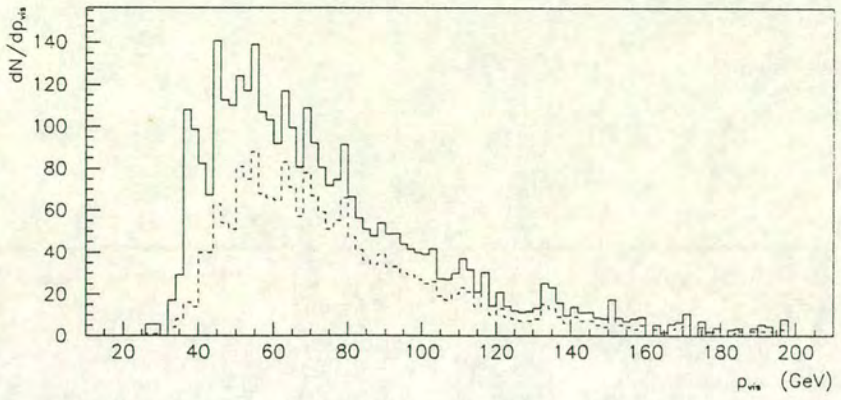

Figure 6.2: The reconstructed kaon momentum spectrum before (dashed line) and after acceptance correction.

where L indicates the distance between the K_L target and the beginning of the fiducial region.

The probability of a decay occurring before the end of the fiducial region is

$$P(before\ z_{max}) = 1 - e^{-F/(\beta\gamma c\tau_{K_L})} \tag{6.9}$$

where the length of the fiducial region is indicated by F.

The weight which has to be applied to each event is thus

$$\begin{aligned} W_{decay}(p) &= \frac{1}{P(z_{min} - z_{max})} \\ &= \frac{e^{L/(\beta\gamma c\tau_{K_L})}}{1 - e^{-F/(\beta\gamma c\tau_{K_L})}} \end{aligned} \tag{6.10}$$

and is a function of the kaon momentum p, through $\beta = p/\sqrt{p^2 + m_K^2}$ and $\gamma = 1/\sqrt{1-\beta^2}$. The effect of the correction due to kaon decay is shown in fig. 6.4.

Trigger efficiency. The efficiency of the $\pi\pi$ trigger may depend on the visible energy, so giving a bias to the recorded events. The most important conditions imposed by this trigger are the Q_x (which requires that the two charged tracks hit two opposite quadrants of the hodoscope) and EHH (threshold on the energy detected in the hadronic calorimeter; see section 3.3).

The geometrical Q_x condition has been applied to the events, so that it is

Not to scale

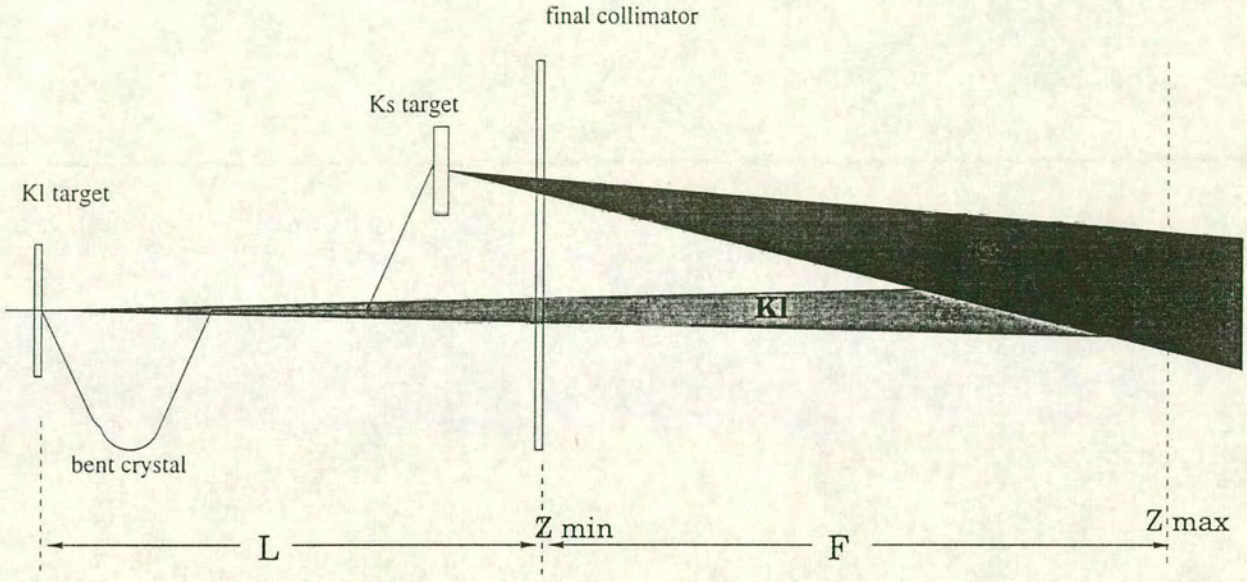

Figure 6.3: Scheme of the fiducial region.

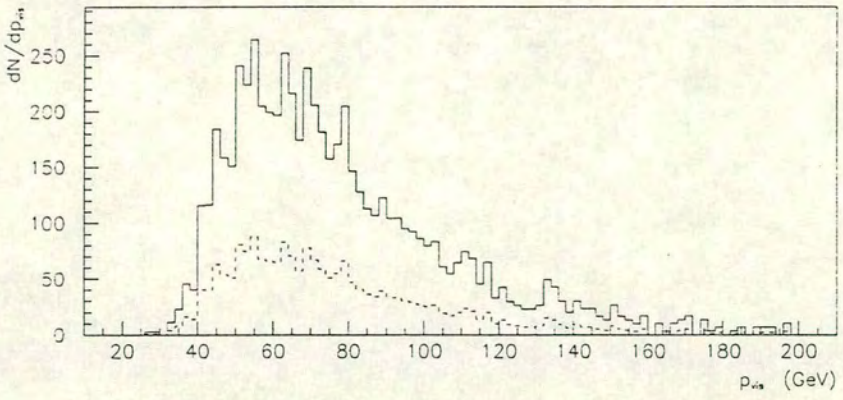

Figure 6.4: The kaon momentum spectrum, before (dashed line) and after the correction due to kaon decay.

not necessary to compute its efficiency.

The efficiency of the EHH condition has been measured using the $K_{\mu 3}$ decays in the minimum bias data sample. The events of interest have been selected essentially by applying a cut on the maximum value of the kinematical variable $(p'_0)^2$ to discard $K_{3\pi}$ events (see section. 5.2.2), and by requiring at least two of the three planes of the muon veto detector to be hit.

When a $K_{\mu 3}$ event occurs, the energy detected by the hadronic calorimeter is that of the charged pion (with a very small contribution from the muon, which in general does not exceed 2 GeV). The efficiency of the EHH condition can thus be evaluated as the ratio between the number of selected $K_{\mu 3}$ events and the number of events in which the EHH condition is satisfied. Such a measurement is performed as a function of the pion energy. The resulting curve has been fitted with the function

$$f(p_\pi) = 1 - 1/(e^{(p_\pi - a)/b} + 1) \tag{6.11}$$

where p_π is the charged pion momentum. The expression (6.11) has been derived from the Fermi function, which gives the probability for an energy level to be filled by an electron. The values of the parameters a, b are 31.29 and 5.28 respectively (errors on parameters: 5.78 and 3.70 respectively. The χ^2 is not significant in this case, since the value of the curve has been artificially set to 1 in a few empty bins at high momentum). The result is shown in fig. 6.5.

Background subtraction. The procedure already described in section 5.2.2 has been performed in bins of kaon momentum and applied to the reconstructed kaon spectrum (the average value of χ^2/ndf is 2.5. The values of the parameters of the fitted fourth-grade polynomials depend on the number of entries in each kaon momentum bin). The effect of such a correction is shown in fig. 6.6.

6.3.2 Determination of the kaon momentum spectrum

The corrected spectrum has been fitted (starting from 50 GeV, in order to avoid possible undetected low-energy trigger inefficiencies without losing too

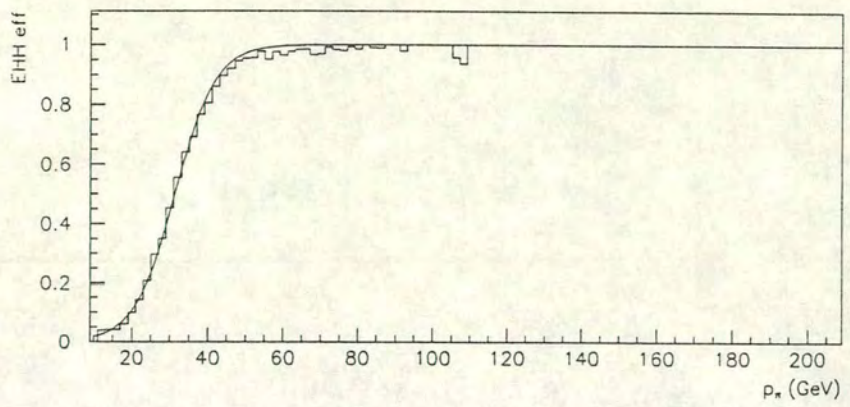

Figure 6.5: Efficiency of EHH condition, as a function of charged pion momentum.

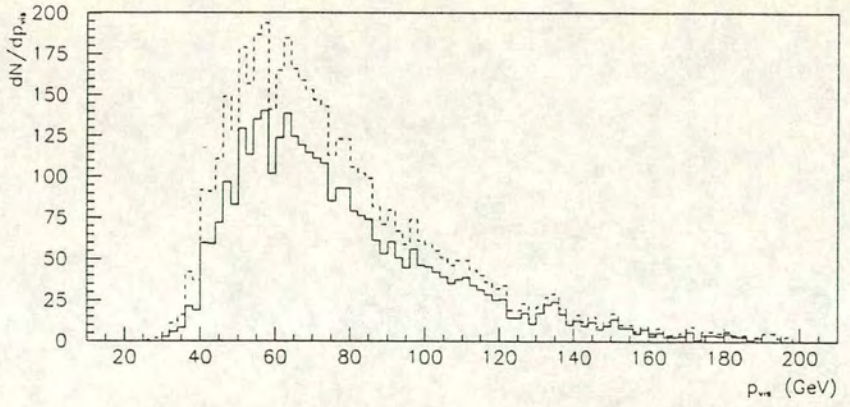

Figure 6.6: The experimental kaon momentum spectrum before (dashed line) and after background subtraction.

much statistics) with a curve derived from the expression given in (6.4). The original spectrum equation has been integrated over θ to eliminate the angular dependency. The integration limits depend on the experimental apparatus, and are $\theta_{min} = 1.4 \cdot 10^{-3}$ mrad and $\theta_{max} = 3.4 \cdot 10^{-3}$ mrad. The error function

$$\frac{2}{\sqrt{\pi}} \int_0^x e^{-t^2 \mathrm{d}t} \tag{6.12}$$

has been computed using the CERN library routine C300 (ERF). A simplified form $\mathcal{S}(p)$ of

$$\int_{\theta_{min}}^{\theta_{max}} \frac{d^2N}{dpd\Omega} \mathrm{d}\theta \tag{6.13}$$

has been used to fit the experimental spectrum:

$$\mathcal{S}(p) = a_0 p/p_0 \cdot e^{a_1 p/p_0} \cdot p a_2^2 \frac{2}{\pi} \int_{a_2\theta_{min}p}^{a_2\theta_{max}p} e^{-(a_2 p\theta)^2} \mathrm{d}\theta \qquad (6.14)$$

where a_0, a_1, a_2 are the free parameters of the fit.
Their resulting values are:

$$\begin{aligned} a_0 &= 352100 \pm 7956 \\ a_1 &= -8.413 \pm 0.156 \\ a_2 &= 4.806 \pm 0.055 \end{aligned}$$

($\chi^2/\mathrm{ndf} = 76.67/67$). The fit is shown in fig. 6.7. The comparison between the experimental momentum spectrum and the one originally implemented in the Monte Carlo program is shown in fig. 6.8. The fitted function (6.14)

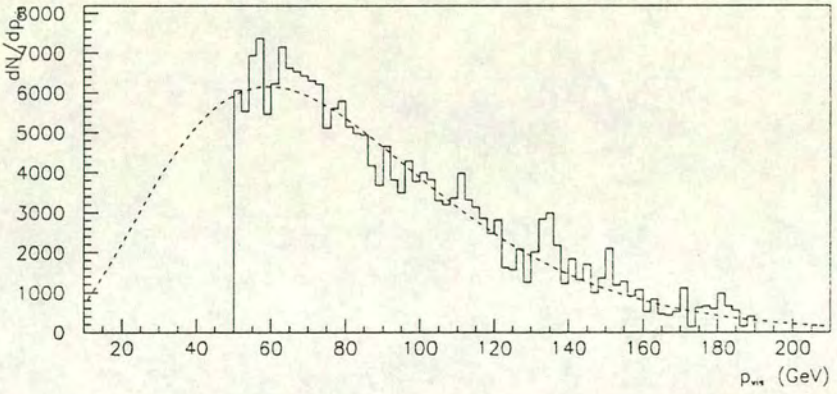

Figure 6.7: The experimental kaon momentum spectrum and the fitted curve.

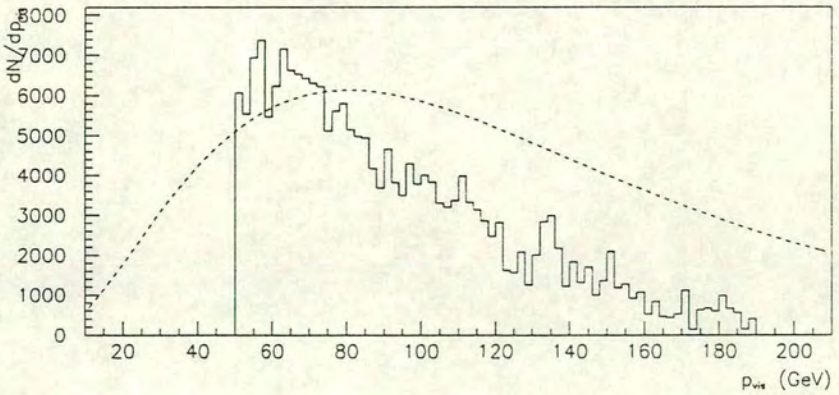

Figure 6.8: The kaon momentum spectrum originally in the Monte Carlo (dashed line) and the experimental one.

has been implemented in the Monte Carlo program, in order to simulate the decays of interest correctly.

6.4 Comparison Between Data and Monte Carlo

Both $K_L \to \pi^+\pi^-$ and $K_L \to \pi^\pm e^\mp \overset{(-)}{\nu}$ events have been generated with NMC Monte Carlo program. Then they have been reconstructed and selected by means of the same algorithms already used for real data. When efficiencies are computed using Monte Carlo, as in this case, a careful comparison between simulated and real events is necessary.

The kaon momentum spectrum has been verified with both $\pi^+\pi^-$ and K_{e3} events. The comparison is especially significant in case of the semi-leptonic decays, since it is a check of the spectrum obtained using the two-pion events. A satisfactory agreement has been found, as shown in fig. 6.9. Fig. 6.10 shows the distribution of the longitudinal decay vertex coordinate for K_{e3} events. The same distributions for $K_L \to \pi^+\pi^-$ are shown in figs. 6.11 and 6.12 respectively.

6.5 Efficiency of the Selection Criteria

After having verified the consistency between data and Monte Carlo, the same cuts already applied to real data (described in chapter 5) have been imposed on simulated (and reconstructed) $\pi^+\pi^-$ and K_{e3} events. The efficiency of the general cuts and of the selection procedure is thus defined as:

$$\epsilon_{sel} = \frac{N_{sel}}{N_{rec}} \tag{6.15}$$

where N_{sel} is the number of events which have survived the cuts, and N_{rec} indicate all those events which had been reconstructed. The computed values are:

- $\epsilon_{sel,K2\pi} = (42.4 \pm 0.2)\%$
- $\epsilon_{sel,Ke3} = (27.9 \pm 0.3)\%$

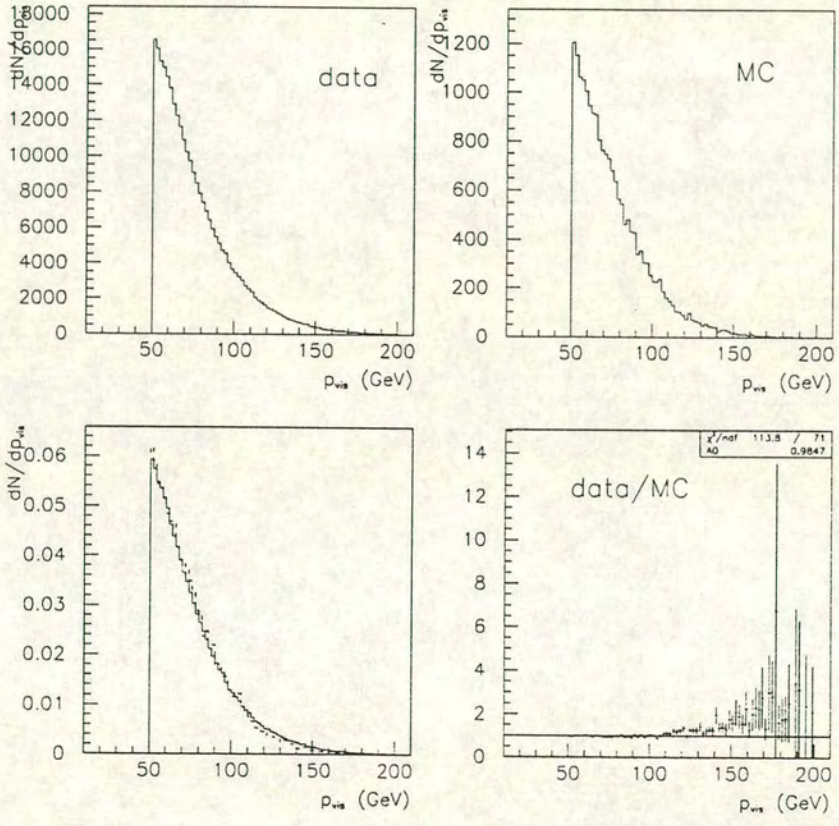

Figure 6.9: Comparison between the visible momentum spectrum for K_{e3} data and Monte Carlo events. The lower left plot shows both real data (solid line) and simulated ones. The ratio data/MC has been fitted with a constant to verify the agreement between the two.

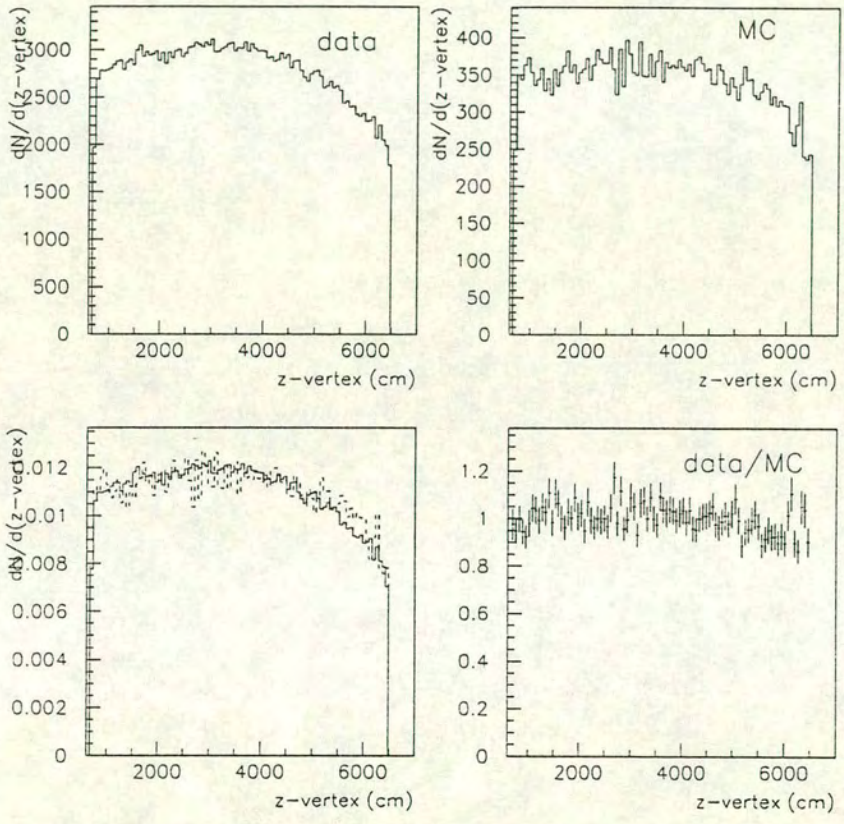

Figure 6.10: The longitudinal vertex coordinate for K_{e3} events, data (upper left), Monte Carlo (upper right), both (lower left; the solid line curve corresponds to real data), and the ratio of the two.

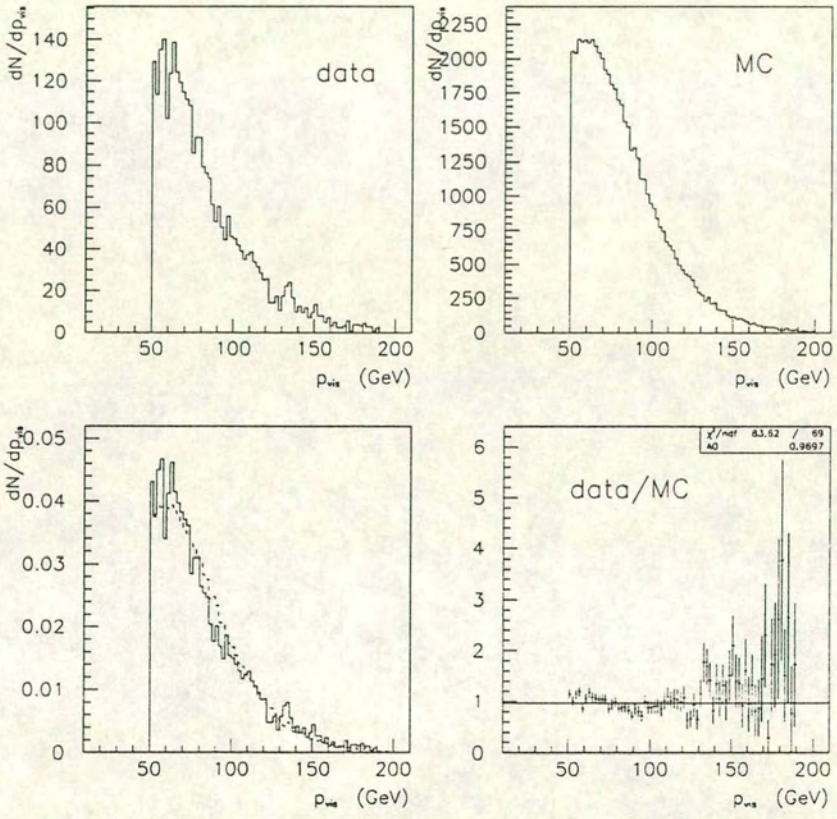

Figure 6.11: Comparison between the kaon momentum spectrum for $\pi^+\pi^-$ data and Monte Carlo events. The lower left plot shows both real data (solid line) and simulated ones. The ratio data/MC has been fitted with a constant to verify the agreement between the two.

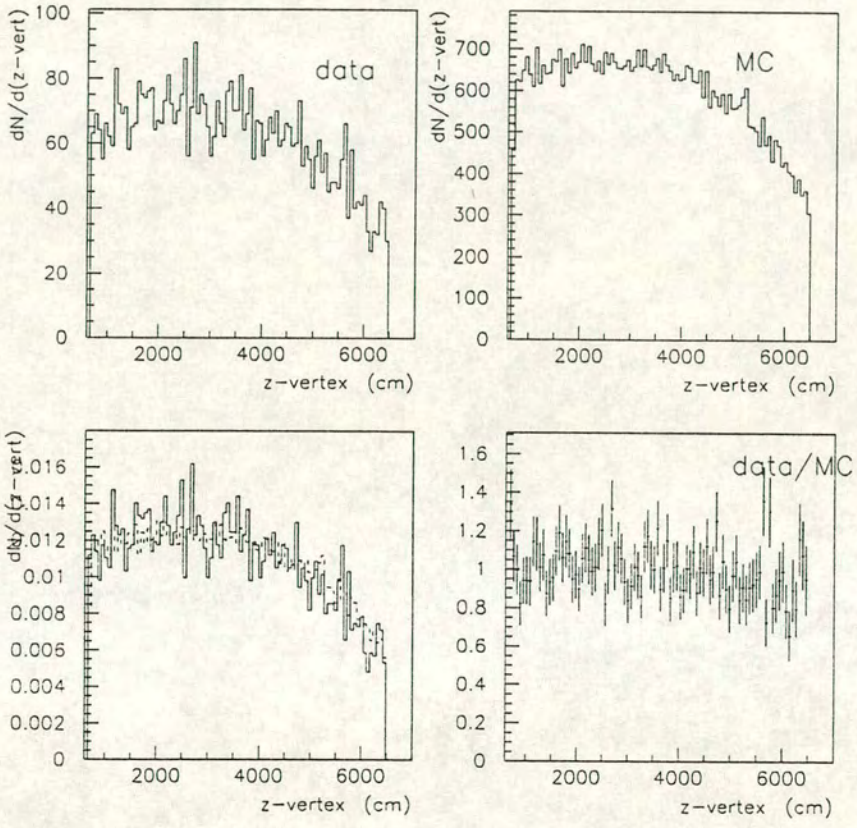

Figure 6.12: The longitudinal vertex coordinate for $\pi^+\pi^-$ events, data (upper left), Monte Carlo (upper right), both (lower left; the solid line curve corresponds to real data), and the ratio of the two.

The general cuts contribution is $(89.8 \pm 0.1)\%$ and $(80.1 \pm 0.2)\%$ for $\pi^+\pi^-$ and K_{e3} events respectively.

6.6 Total Efficiencies

The total efficiencies are computed as the product of the reconstruction and the selection efficiencies. The resulting values are

- $\epsilon_{tot,K2\pi} = \epsilon_{rec,K2\pi} \cdot \epsilon_{sel,K2\pi} = (41.5 \pm 0.2)\%$
- $\epsilon_{tot,Ke3} = \epsilon_{rec,Ke3} \cdot \epsilon_{sel,Ke3} = (25.6 \pm 0.3)\%$

The quoted errors are purely statistical.

The geometrical acceptance is applied event by event in bins of visible momentum and longitudinal vertex coordinate, as described in section 6.1. The efficiency of the EHH trigger condition (see section 6.3.1) is applied in bins of visible momentum to the events selected in the $\pi\pi$ trigger data set. The background subtraction procedure (section 5.2.2) is applied to the $\pi^+\pi^-$ sample.
The results are reported in the following table (6.1):

Decay mode	$\pi\pi$ trigger	minimum bias trigger
$K_L \to \pi^+\pi^-$	2737	1511
$K_L \to \pi^\pm e^\mp \overset{(-)}{\nu}$	318983	154561

Table 6.1: Number of selected events in the two data sets, for each of the two decay modes of interest, after the geometrical acceptance and trigger efficiency corrections.

CHAPTER 7

RESULTS

In this chapter the computation of $BR(K_L \to \pi^+\pi^-)$ is reported, as well as an evaluation of the systematic error which affects the measurement and a discussion of the obtained results.

7.1 THE SYSTEMATIC ERROR

The two-pion events have been selected by imposing several conditions. The application of each of these selection criteria has an associated systematic error. For example, the systematic uncertainty in the number of $\pi\pi$ events arising from the lower cut on the visible momentum is estimated to be 1.9% of the total number of selected $\pi\pi$ decays. In fact, assuming a momentum resolution of 1%, the value of the cut has been varied accordingly, and the total number of events ri-calculated. Since the same variation is observed in the K_{e3} decay channel, and the two effects cancel in the ratio. The same argument holds for the length of the fiducial volume (which gives a systematic effect of less than 1% in both decay modes, assuming a resolution of 2%) and for the other selection cuts. It is difficult to separate each single contribution from the common overall effect on the shape of the final momentum spectrum, from which the Monte Carlo momentum spectrum has been derived.
The most significant source of systematic error is thus the shape of the kaon momentum spectrum in the Monte Carlo program. After reconstructing the kaon momentum as the vector sum of the charged pions momenta, several corrections have been applied (see section 6.3.1).
The geometrical acceptance of the detector has been computed using the Monte Carlo program and applied to the spectrum in bins of momentum and

longitudinal coordinate of the vertex. A mismatch between the geometry description in the Monte Carlo program and the real one brings a systematic error which is reflected in the shape of the kaon spectrum. An erroneous description of the geometry of the fiducial region causes a systematic effect in the correction due to kaon decay as well.

An undetected trigger inefficiency (for example, in the time measurement used in the Q_x condition of the $\pi\pi$ trigger) can heavily affect the shape of the spectrum, especially at low energies.

Finally, the background subtraction has been performed by fitting the transverse momentum squared distribution with a polynomial, and then applied to the kaon spectrum in bins of momentum. Such a fit gives a systematic error too.

The agreement between the Monte Carlo and the real kaon spectrum is crucial for our measurement, since the branching ratio has been computed integrating over the whole accepted range of visible momentum.

In order to estimate the systematic error arising from the fit to experimental data, the variation of the integral

$$\int_{p_{min}}^{p_{max}} \left(a_0 p/p_0 \cdot e^{a_1 p/p_0} \cdot p a_2^2 \frac{2}{\pi} \int_{a_2\theta_{min}p}^{a_2\theta_{max}p} e^{-(a_2 p\theta)^2} \mathrm{d}\theta \right) dp \qquad (7.1)$$

(where $p_{min} = 65$ GeV, $p_{max} = 200$ GeV) has been evaluated as a function of the value of the parameters a_0, a_1, a_2, within 1 σ.

The variation has been found to be 4.2%.

7.2 Computation of $\frac{\Gamma(K_L \to \pi^+\pi^-)}{\Gamma(K_L \to \pi^\pm e^\mp \overset{(-)}{\nu})}$

The ratio R of the two studied decay modes is evaluated according to the expression

$$R = \frac{\Gamma(K_L \to \pi^+\pi^-)}{\Gamma(K_L \to \pi^\pm e^\mp \overset{(-)}{\nu})} = \frac{N^\star_{K2\pi}}{N^\star_{Ke3}} \cdot \frac{\epsilon_{tot,Ke3}}{\epsilon_{tot,K2\pi}} \qquad (7.2)$$

where $N^\star_{K2\pi}$ and $N^\star_{Ke3}$ indicate the number of events in the two channels corrected for geometrical acceptance and trigger efficiency, and $\epsilon_{tot,K2\pi}$, $\epsilon_{tot,Ke3}$ are the corresponding total efficiencies.

Substituting the computed values in (7.2), one finds

- $\pi\pi$ trigger data sample: $R = (0.53 \pm 0.01 \pm 0.02) \times 10^{-2}$

- minimum bias trigger data sample: $R = (0.53 \pm 0.02 \pm 0.02) \times 10^{-2}$

where the first quoted error is statistical and the second is systematic. Combining the above results, the obtained measurement is

$$R = (0.53 \pm 0.02) \times 10^{-2}.$$

7.3 Discussion of Results

A direct measurement of $\Gamma(K_L \to \pi^+\pi^-)/\Gamma(K_L \to \pi^\pm e^\mp \overset{(-)}{\nu})$ like the one performed here has never been published.

From the known quantities

$$\frac{\Gamma(K_L \to \pi^+\pi^-)}{\Gamma(K_L \to \pi^\pm e^\mp \overset{(-)}{\nu}) + \Gamma(K_L \to \pi^\pm \mu^\mp \overset{(-)}{\nu})} \tag{7.3}$$

and

$$\frac{\Gamma(K_L \to \pi^\pm \mu^\mp \overset{(-)}{\nu})}{\Gamma(K_L \to \pi^\pm e^\mp \overset{(-)}{\nu})} \tag{7.4}$$

it is possible to compute the value of $\Gamma(K_L \to \pi^+\pi^-)/\Gamma(K_L \to \pi^\pm e^\mp \overset{(-)}{\nu})$. The ratio (7.3) has been measured by two different collaborations [59, 60] in 1985 and 1977. The Particle Data Group fit [6] gives the value

$$\frac{\Gamma(K_L \to \pi^+\pi^-)}{\Gamma(K_L \to \pi^\pm e^\mp \overset{(-)}{\nu}) + \Gamma(K_L \to \pi^\pm \mu^\mp \overset{(-)}{\nu})} = (3.13 \pm 0.06) \times 10^{-3}. \tag{7.5}$$

Two older measurements of (7.3) [61, 62] do not agree with the more recent [59, 60], and have been excluded from the fit.

The particle Data Group fit for (7.4) gives the value

$$\frac{\Gamma(K_L \to \pi^\pm \mu^\mp \overset{(-)}{\nu})}{\Gamma(K_L \to \pi^\pm e^\mp \overset{(-)}{\nu})} = 0.701 \pm 0.009 \tag{7.6}$$

Making use of the two above results, the computed value of the quantity under investigation is

$$\frac{\Gamma(K_L \to \pi^+\pi^-)}{\Gamma(K_L \to \pi^\pm e^\mp \overset{(-)}{\nu})} = (0.53 \pm 0.01) \times 10^{-2}$$

in agreement with the one measured here.

It is also possible to compare the obtained result for $\Gamma(K_L \to \pi^+\pi^-)/\Gamma(K_L \to \pi^\pm e^\mp \overset{(-)}{\nu})$ with the ratio of the absolute branching ratios of the two decay modes. The values are $(2.067 \pm 0.035) \times 10^{-3}$ and $(38.78 \pm 0.27)\%$ for $\Gamma(K_{2\pi})$ and $\Gamma(K_{e3})$ respectively (as in [6]; see table 1.1).
Their ratio gives the value

$$\frac{\Gamma(K_L \to \pi^+\pi^-)}{\Gamma(K_L \to \pi^\pm e^\mp \overset{(-)}{\nu})} = (0.53 \pm 0.01) \times 10^{-2}$$

in agreement with the measurement performed here.

From relation (7.2), the branching ratio of $K_L \to \pi^+\pi^-$ can be obtained as

$$BR(K_L \to \pi^+\pi^-) = R \cdot BR(K_L \to \pi^\pm e^\mp \overset{(-)}{\nu}) \tag{7.7}$$

Using the quoted value for $BR(K_{e3})$, the result is

$$BR(K_{2\pi}) = (2.06 \pm 0.08) \times 10^{-3}$$

The above result for the branching ratio of $K_L \to \pi^+\pi^-$ has to be compared with the existing value $(2.067 \pm 0.035) \cdot 10^{-3}$.
The measurement performed here agrees with the existing one, but with a much less accurate precision due to the lack of statistics. The scarcity of the available data sample not only increases the statistical error, but also heavily contributes to the systematic one, since it does not allow an accurate reconstruction of the kaon momentum spectrum.

The value of the quantity $|\eta_{+-}|$ (see section 1.3.3) can be evaluated as well, knowing the branching ratio for the K_S decay into two charged pions:

$$BR(K_S \to \pi^+\pi^-) = (68.61 \pm 0.28)\%$$

and $\tau(K_S) = (0.8927 \pm 0.0009) \times 10^{-10}$ s, $\tau(K_L) = (5.17 \pm 0.04) \times 10^{-8}$ s [6].
From the expression

$$|\eta_{+-}| = \left[\frac{BR(K_L \to \pi^+\pi^-)}{\tau(K_L)} \cdot \frac{\tau(K_S)}{BR(K_S \to \pi^+\pi^-)}\right]^{1/2} \tag{7.8}$$

one obtains the value

$$|\eta_{+-}| = (2.28 \pm 0.09) \times 10^{-3}$$

in agreement with the known value $(2.285 \pm 0.019) \times 10^{-3}$. This measurement will be performed with a better accuracy with the data NA48 will collect in the future.

CONCLUSIONS

The analysis described here has been performed on the first data taken by the experiment NA48 at CERN, in 1995. The aim of the experiment is the determination of the CP violation parameter $\mathrm{Re}(\varepsilon'/\varepsilon)$ with an accuracy of 2×10^{-4}. The method used consists of a comparison between the probabilities for long- and short-lived neutral kaons to decay in two-pion states.
The purpose of 1995 data-taking period was to commission the various components of the detector and the innovative data recording technique. This aim was successfully achieved.

The collected data allowed the determination of the branching ratio of the decay $K_L \to \pi^+\pi^-$ relative to that of $K_L \to \pi^\pm e^\mp \overset{(-)}{\nu}$, as described here. The measurement gives:

$$\frac{K_L \to \pi^+\pi^-}{K_L \to \pi^\pm e^\mp \overset{(-)}{\nu}} = (0.53 \pm 0.02 \pm 0.02) \times 10^{-2}$$

where the quoted errors are statistical and systematic respectively. Although a direct measurement of this quantity has never been published, the result is in agreement with the value which can be computed using other published results.
This analysis has provided a first direct measurement of the neutral kaon momentum spectrum in the NA48 setup, an essential element in simulation studies.

The presented analysis has been useful in understanding the performance of the detector and which aspects need further studies. The mass resolution of the magnetic spectrometer has proven very satisfying at 2.5 MeV. The particle identification will be properly performed when the electromagnetic

calorimeter information is available. The neutral kaon momentum spectrum will be improved once more data have been collected and analysed.

APPENDIX A

CHECK OF GEOMETRICAL ACCEPTANCE

For the two-pion decay mode, it is possible to compute the geometrical acceptance analytically.

The minimum and the maximum accepted angles θ_{min}, θ_{max} for a single track are determined by the minimum and maximum accepted radii R_{min}, R_{max}. The former is imposed at the 'general cuts' stage (see section 5.2.1), the latter corresponds to the outer radius of the detector.

The value of θ_{min} and θ_{max} is not fixed, but depends on the longitudinal position of the kaon decay vertex.

In the centre of mass reference frame the following equations hold:

$$\begin{aligned} p_l &= \gamma(\beta E_{CM} + p' \cos\theta_{CM}) \\ p_t &= p' \sin\theta_{CM} \end{aligned} \tag{A.1}$$

where $\beta = p/\sqrt{p^2 + m_K^2}$ (p and m_K being the kaon laboratory momentum and mass), p_l and p_t are the longitudinal and transverse components of the momentum p' of the centre of mass, and θ_{CM} is the polar angle of the momentum with respect to a longitudinal axis.

From the above expressions, one obtains

$$\tan\theta_{LAB} = \frac{p_t}{p_l} = \frac{\sin\theta_{CM}}{\gamma(\beta/\beta_{CM} + \cos\theta_{CM})} \tag{A.2}$$

where

$$\beta_{CM} = \frac{p_{CM}}{E_{CM}} \tag{A.3}$$

for each pion. The momentum p_{CM} has opposite sign for the two particles, one going forward with respect to the centre of mass, and the other going

backward. The relation between the angles in the laboratory and in the centre of mass frame is thus

$$\tan\theta_{LAB} = \frac{\sin\theta_{CM}}{\gamma(\cos\theta_{CM} \pm \beta/\beta_{CM})} \tag{A.4}$$

and it can be drawn in the $(\cos\theta_{CM}, \tan\theta_{LAB})$ plane (as in fig. A.2).
The pure geometrical acceptance of the detector is the portion of the $\cos\theta_{CM}$ axis corresponding to the region in which both pions fall inside the detector, i.e. $\tan\theta_{min} < \tan\theta_{LAB} < \tan\theta_{max}$ for both particles, as shown in fig. A.2. A weight can thus be computed for each event, as $(1/(\cos\theta_{CM}$ accepted interval).
The comparison between the reconstructed kaon spectrum before and after this correction is given in fig. A.1.

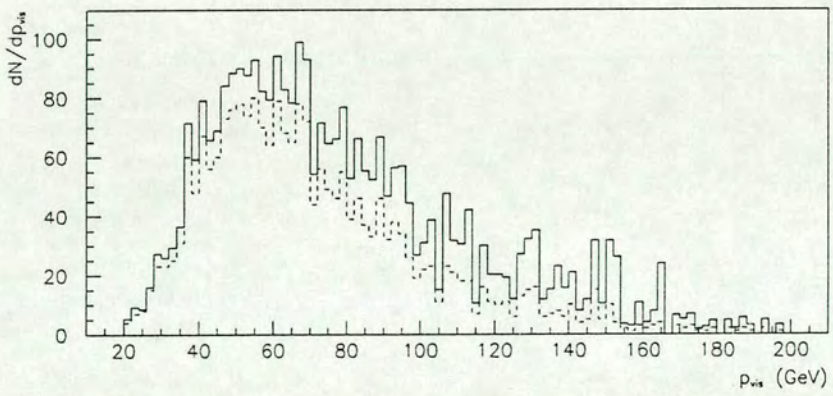

Figure A.1: The reconstructed kaon momentum spectrum before (dashed line) and after analytical acceptance correction.

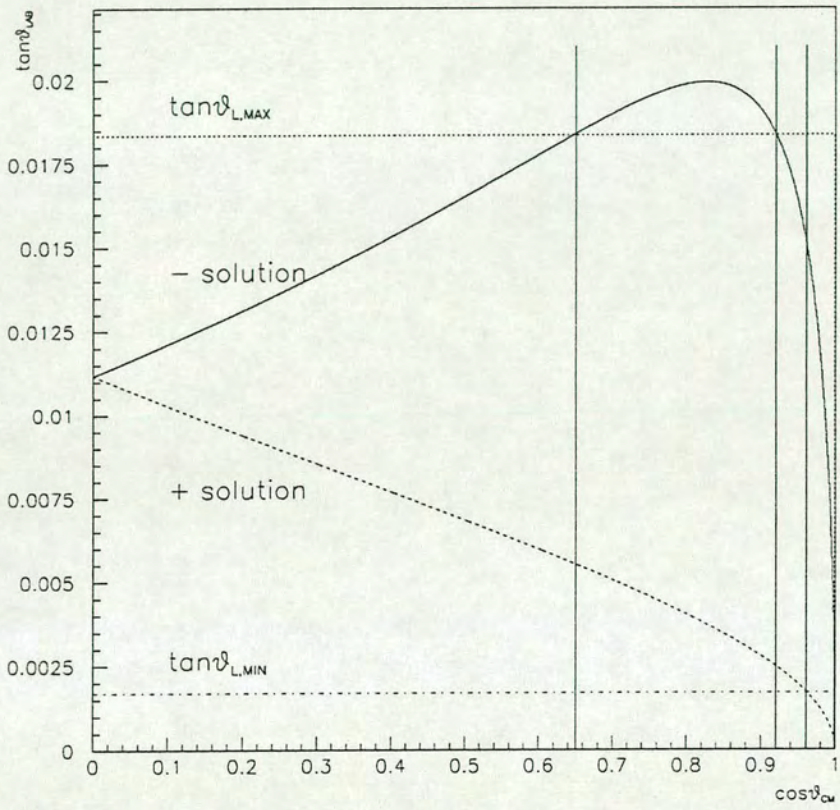

Figure A.2: The tangent of the polar angle in the laboratory as a function of the cosine of the angle in the centre-of-mass system. The shown solutions correspond to the particle going forward ("+ solution"), and to the one going backward ("- solution").

Bibliography

[1] T. P. Cheng and L. F. Li, *Gauge theory of elementary particle physics*, Clarendon press, Oxford, 1986.

[2] G. Lüders, Dan.Mat.Fys. Medd. **28**, n.5 (1954).

[3] W. Pauli, in *Niels Bohr and the Development of Physics.* Mc Graw-Hill, New York, 1955.

[4] T.D. Lee, C.N. Yang, Phys. Rev. *104*, 254 (1956).

[5] J.H. Christenson, J.W. Cronin, V.L. Fitch and R. Turlay, Phys. Rev. Lett **13** (1964), 138.

[6] Particle Data Group, *Review of Particle Physics*, Phys. Rev. **D54** (1996) Part. 1.

[7] L.M. Chounet *et al*, Phys. Reports **4C** (1972), 199.

[8] L.F. Li, Phys. Rev. **D21** N.1 (1980), 178.

[9] J.F. Donoghue, Phys. Rev. **D36** N.3 (1987), 798.

[10] H.Y. Cheng, Phys. Lett. **129B** N.5 (1983), 357.

[11] K.J. Peach *et al*, Nucl. Phys. **B127** (1977), 399.

[12] Y. Cho *et al*, Phys. Rev. **D15** (1977), 587.

[13] K. Kleinknecht, in *CP violation*, ed. C. Jarlskog, Advanced Series on Directions in High Energy Physics, Vol. 3, World Scientific, Singapore (1989).

[14] L. Wolfenstein, Phys. Rev. Lett. **13** (1964), 562.

[15] N. Cabibbo, Phys. Rev. Lett. **10** (1963), 513.

[16] M. Kobayashi and T. Maskawa, Prog. Theor. Phys **49**, N.2 (1973).

[17] L. Wolfenstein, Phys. Rev. Lett. **51** (1983), 1945.

[18] C. Jarlskog, in *CP violation*, ed. C. Jarlskog, Advanced Series on Directions in High Energy Physics, Vol. 3, World Scientific, Singapore (1989).

[19] A. Masiero, *CP violation for pedestrians*, Proceedings of 1993 European School of High-Energy Physics, Zakopane, Poland, Sept. 1993. Ed. by N. Ellis and M.B. Gavela, CERN, 189-215.

[20] L.K. Gibbons *et al*, Phys. Rev. Lett. **70** (1993), 1203.

[21] G.D. Barr *et al*, Phys. Lett. **317B** (1993), 233.

[22] *KTeV Design Report*, FN-580, Fermi National Laboratory, Batavia, Illinois (1992).

[23] INFN-LNF, *Proposal for a Φ-Factory*, LNF-90/031(R) (1990).

[24] `http://www.cern.ch/CERN/Divisions/SL/spspage.html`

[25] G. D. Barr *et al*, *Proposal for a Precision Measurement of ε'/ε in CP violating $K^0 \to 2\pi$ decays*, CERN/SPSC/90-22, SPSSC/P253, July 1990.

[26] N. Doble, L. Gatignon, and P. Grafström, *A novel application of bent crystal channelling to the production of simultaneous particle beams*, CERN preprint, CERN/SL/95-16 (EA), March 1995.

[27] R. Moore *et al.*, NA48 internal note 1994-40 (1994).

[28] NA48 collaboration (presented by P. Buchholz) Nucl. Instr. and Meth. **A316** (1992), 1.

[29] G. Barr *et al*, Nucl. Instr. and Meth. **A323** (1992), 393.

[30] V. Fanti *et al*, Nucl. Instr. and Meth. **A344** (1994), 507.

[31] G. D. Barr et al, *Performance of an electro-magnetic liquid krypton calorimeter based on a a ribbon electrode tower structure,* Nucl. Instr. and Meth. **A370** (1996), 413. http://www.cern.ch/NA48/Welcome/papers/Overview.html#95

[32] W.E. Cleland and E.G. Stern, Nucl. Instr. and Meth. **A338** (1994), 467.

[33] M. Calvetti *et al.*, NA48 internal note 1995-1 (1995).

[34] G. Barr *et al.*, NA48 internal note 1994-4 (1994).

[35] S. Anvar *et al*, NA48 internal note 1994-13 (1994).

[36] F. Bertolino *et al*, IEEE Transactions on Nuclear Science, **41** (1994), 274.

[37] http://www.meiko.com/info/welcome.html

[38] G. Barr *et al.*, NA48 internal note 1994-11 (1994).

[39] J.-P. Matheys *et al*, NA48 internal note 1995-19 (1995).

[40] P. Brodier-Yourstone, IEEE Transactions on Nuclear Science, **42** (4) (1995), 870.

[41] A. Van Praag, *Testing a long distance serial HIPPI link for NA48*, unpublished, http://www.cern.ch/HSI/hippi/longdist/shtest1.htm

[42] P. Cenci, private communication.

[43] http://wwwcn.cern.ch/asdoc/zebra_html3/zebramain.html

[44] CERN Application Software Group, *GEANT detector description and Simulation Tool*, CERN Program Library Long Writeup W5013 (1994). http://wwwcn.cern.ch/asdoc/geant/GEANTMAIN.html

[45] V. Schönharting, NA48 Internal note 1996-17 (1996).

[46] http://www.cern.ch/GPMIMD2

[47] J. Shiers *et al*, *ZEBRA: Overview of the Zebra System*, CERN Program Library Long Writeup Q100/Q101 (1995).

[48] F. James, *RANLUX: A Fortran implementation of the high-quality pseudorandom number generator of Lüscher*, Computer Phys. Commun. **79** (1994), 111.

[49] J.G. Mills *et al. CHIMP Concepts*, EPCC Technical Report EPCC-KTP-CHIMP-CONC (1991).

[50] R. Alasdair *et al. CHIMP Version 2.0 User Guide*, EPCC Techical Report EPCC-KTP-CHIMP-V2-USER (1993).

[51] `http://www.epcc.ad.ec.uk/epcc-projects/CHIMP`

[52] R. Hempel, *The ANL/GMD macros (PARMACS) in fortran for portable parallel programming using the message passing programming model - users' guide and reference manual.* Technical report, Forschungszentrum Informationstechnik GmbH (GMD) (1991).

[53] R. Hempel, H.-C. Hoppe, A. Supalov, *A proposal for a PARMACS library interface.* Technical report, GMD (1992).

[54] `http://www.mcs.anl.gov/mpi`

[55] C. Bruschini *et al*, *Simulation of a Parallel Scheme for the Online Calibration of NA48 Electromagnetic Calorimeter*, NA48 Internal Note, Oct. 1995.

[56] A. Ceccucci and G. Lasio, *The NA48 Electromagnetic Calorimeter: Some Simulation Results*, NA48 Internal Note, Sep. 1995.

[57] B. Hay, *Ph. D. Thesis*, University of Edinburgh, 1996.

[58] H.W. Atherton *et al*, CERN Yellow Report 80-07 (1980).

[59] D.P. Coupal *et al*, Phys. Rev. Lett. **55** (1985), 566.

[60] R. Devoe *et al*, Phys. Rev. **D16** (1977), 565.

[61] X. de Bouard *et al*, Nuovo Cimento **52A** (1967), 662.
And: Phys. Lett. **15** (1965), 58.

[62] V.L. Fitch *et al*, Phys. Rev. **164** (1967), 1711.